

## INFORMATION TO USERS

This manuscript has been reproduced from the microfilm master. UMI films the text directly from the original or copy submitted. Thus, some thesis and dissertation copies are in typewriter face, while others may be from any type of computer printer.

The quality of this reproduction is dependent upon the quality of the copy submitted. Broken or indistinct print, colored or poor quality illustrations and photographs, print bleedthrough, substandard margins, and improper alignment can adversely affect reproduction.

In the unlikely event that the author did not send UMI a complete manuscript and there are missing pages, these will be noted. Also, if unauthorized copyright material had to be removed, a note will indicate the deletion.

Oversize materials (e.g., maps, drawings, charts) are reproduced by sectioning the original, beginning at the upper left-hand corner and continuing from left to right in equal sections with small overlaps. Each original is also photographed in one exposure and is included in reduced form at the back of the book.

Photographs included in the original manuscript have been reproduced xerographically in this copy. Higher quality 6" x 9" black and white photographic prints are available for any photographs or illustrations appearing in this copy for an additional charge. Contact UMI directly to order.

# U·M·I

University Microfilms International  
A Bell & Howell Information Company  
300 North Zeeb Road, Ann Arbor, MI 48106-1346 USA  
313/761-4700 800/521-0600



Order Number 9209706

**Plasma dynamics of the Earth magnetopause-boundary layer  
and its coupling to the polar ionosphere**

Wei, Chang-Quan, Ph.D.

University of Alaska Fairbanks, 1991

**U·M·I**  
300 N. Zeeb Rd.  
Ann Arbor, MI 48106

/ /

**PLASMA DYNAMICS OF THE EARTH MAGNETOPAUSE-BOUNDARY  
LAYER AND ITS COUPLING TO THE POLAR IONOSPHERE**

**A  
THESIS**

**Presented to the Faculty  
of the University of Alaska Fairbanks  
in Partial Fulfillment of the Requirements  
for the Degree of**

**DOCTOR OF PHILOSOPHY**

**By  
Chang-Quan Wei, B. S., M. S.**

**Fairbanks, Alaska**

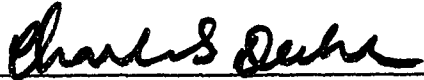
**December 1991**

PLASMA DYNAMICS OF THE EARTH MAGNETOPAUSE-BOUNDARY  
LAYER AND ITS COUPLING TO THE POLAR IONOSPHERE

By

Chang-Quan Wei

RECOMMENDED:



C. S. Deehr



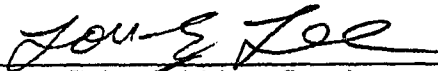
D. W. Swift



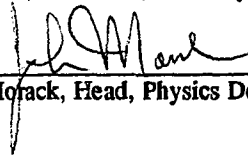
W. R. Tape



B. J. Watkins

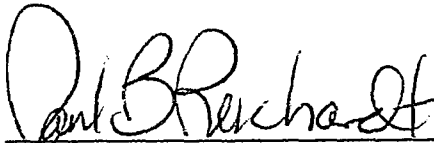


L. C. Lee, Chairman, Advisory Committee



J. L. Morack, Head, Physics Department

APPROVED:



P. B. Reichardt, Dean, College of Natural Sciences



L. Proenza, Dean of the Graduate School

10/7/91

Date

## ABSTRACT

In this thesis, the plasma dynamics of the Earth magnetopause-boundary layer and its coupling to the polar ionosphere are studied by using computer simulations.

First, the plasma dynamics and structure of the magnetopause-boundary layer are studied by a two-dimensional incompressible magnetohydrodynamic simulation code. It is found that the Kelvin-Helmholtz instability with driven boundary conditions at the magnetopause can lead to the formation of plasma vortices observed in the magnetopause-boundary layer. In the later stage of development, a density plateau is formed in the central part of the boundary layer.

Second, the coupling of plasma vortices formed in the boundary layer to the polar ionosphere is studied based on a magnetosphere-ionosphere coupling model. The finite ionospheric conductivity provides a dragging force to the plasma flow and leads to the decay of plasma vortices in the boundary layer. In the model, the ionospheric conductivity is allowed to be enhanced due to accelerated electrons precipitating in upward field-aligned current regions. The competing effect of the formation and decay of vortices leads to the formation of strong vortices only in limited regions. Several enhanced conductivity regions are formed along the post-noon auroral oval, which may account for the observed auroral bright spots.

In addition, the evolution of localized plasma vortices, as well as magnetic flux ropes, along magnetic field lines is studied. The evolution leads to the generation of large-amplitude Alfvén waves, which carry field-aligned currents and provide the link for the coupling of plasma vortices and magnetic flux ropes in the magnetosphere to the polar ionosphere.

## TABLE OF CONTENTS

	Page
<b>Abstract</b>	iii
<b>Table of Contents</b>	iv
<b>List of Figures</b>	vi
<b>Acknowledgments</b>	ix
<b>CHAPTER 1. Overview</b>	1
1.1 Observations of the Magnetopause-Boundary Layer	7
1.2 Observations of Auroral Bright Spots	9
1.3 Magnetic Impulse Events	13
1.4 Previous Theoretical and Simulation Work	15
1.5 Outline of the Thesis	17
<b>CHAPTER 2. Vortex Structures in the Low-Latitude Boundary Layer</b>	19
2.1 Introduction	19
2.2 Simulation Model and Numerical Scheme	22
2.2.1 Simulation Model and Governing Equations	22
2.2.2 Differencing Scheme and Numerical Procedure	26
2.2.3 Boundary Conditions	27
2.3 Simulation Results	28
2.3.1 Case A: Local Injection at the Magnetopause	29
2.3.2 Case B: Uniform Injection at the Magnetopause	36
2.3.3 Case C: A Sheared Plasma Flow with Periodic Boundary Conditions	42
2.3.4 Case D: A Sheared Plasma Flow with Outflow Boundary Conditions	47
2.4 Discussion and Summary	51



<b>CHAPTER 3. Auroral Bright Spots</b>	<b>55</b>
3.1 Introduction	55
3.2 Simulation Model and Governing Equations	58
3.3 Simulation Results	70
3.3.1 Periodic Cases	71
3.3.2 Uniformly Driven Cases Along the Duskside Magnetopause	74
3.3.3 Locally Driven Cases Along the Duskside Magnetopause	85
3.3.4 Dawnside Magnetopause Driven Cases	88
3.4 Summary and Discussion	91
<b>CHAPTER 4. Evolution of Magnetic Flux Ropes and Plasma Vortices</b>	<b>94</b>
4.1 Introduction	94
4.2 Simulation Model	100
4.2.1 Governing Equations	100
4.2.2 Initial Conditions and Normalization	102
4.2.3 Simulation Box and Boundary Conditions	103
4.3 Evolution of Magnetic Flux Tubes	105
4.3.1 Case A: A Small $B_\theta/B_0$ Ratio	105
4.3.2 Case B: A Large $B_\theta/B_0$ Ratio	115
4.3.3 Effect of Tube Length on the Evolution of the Magnetic Field	117
4.3.4 Effect of Ratio $B_\theta/B_0$ on the Wave Speed	121
4.4 Evolution of Localized Plasma Vortices	123
4.4.1 Initial and Boundary Conditions	123
4.4.2 Simulation Results	124
4.5 Discussion	128
4.6 Summary	131
<b>CHAPTER 5. Summary and Discussion</b>	<b>133</b>
<b>APPENDIX. Numerical Technique for Solving Magnetosphere-Ionosphere Coupling Equations</b>	<b>139</b>
<b>REFERENCES</b>	<b>143</b>

## LIST OF FIGURES

		Page
Fig. 1.1	A sketch of the Earth's magnetosphere showing the magnetopause and the boundary layer.	2
Fig. 1.2	Schematic sketches of interactions among the solar wind, the magnetosphere, and the ionosphere.	3
Fig. 1.3	Schematic representation of physical processes related to the observed magnetic impulse event.	6
Fig. 1.4	Plasma and magnetic field data from an ISEE outbound pass.	8
Fig. 1.5	An auroral image from the ultraviolet imager on the Viking satellite.	11
Fig. 1.6	Magnetic field traces from two ground stations.	14
Fig. 2.1	Schematic sketch of the simulation domain in the equatorial plane of the magnetosphere.	24
Fig. 2.2a	Contour plots of the plasma density at different simulation times in Case A.	30
Fig. 2.2b	Vector plots of the flow velocity at different simulation times in Case A.	31
Fig. 2.3	The plasma density and the flow velocity as a function of time measured at three fixed probes in Case A.	34
Fig. 2.4	Profiles of the plasma density and the flow velocity in the boundary layer parallel to the magnetopause in Case A.	35
Fig. 2.5	Profiles of the plasma density and the flow velocity across the boundary layer in Case A.	37
Fig. 2.6a	Contour plots of the plasma density at different simulation times in Case B.	39
Fig. 2.6b	Vector plots of the flow velocity at different simulation times in Case B.	40
Fig. 2.7	Profiles of the plasma density and the flow velocity in the boundary layer parallel to the magnetopause in Case B.	41

Fig. 2.8	(a) Contour plots of the plasma density and (b) vector plots of the flow velocity at different simulation times in Case C.	44
Fig. 2.9	Profiles of the plasma density across the center of the vortex in Case C.	46
Fig. 2.10	Profiles of the plasma density and the flow velocity in the boundary layer parallel to the magnetopause in Case C.	48
Fig. 2.11	(a) Contour plots of the plasma density and (b) vector plots of the flow velocity at different simulation times in Case D.	50
Fig. 3.1	Schematic sketches of simulation domains for the duskside magnetopause driven cases.	61
Fig. 3.2	Four two-dimensional plots for a case with periodic boundary conditions in the boundary layer and $R_{hp} = 1$ .	72
Fig. 3.3	Five two-dimensional plots for a case with the uniform driven condition at the duskside region of the magnetopause and $R_{hp} = 1$ .	75
Fig. 3.4	Contour plots of the ionospheric Pedersen (or Hall) conductivity at different simulation times for the above case.	78
Fig. 3.5	Same as Fig. 3.3, but for a case with the uniform driven condition at the duskside region of the magnetopause and $R_{hp} = 2$ .	80
Fig. 3.6	Maximum upward FAC density as a function of the coupling coefficient $\alpha$ .	84
Fig. 3.7	Same as Fig. 3.3, but for a case with the localized driven condition at the duskside region of the magnetopause and $R_{hp} = 2$ .	87
Fig. 3.8	Same as Fig. 3.3, but for a case with the uniform driven condition at the dawnside region of the magnetopause and $R_{hp} = 3$ .	90
Fig. 4.1	Schematic representation of how boundary layer vortices couple to the polar ionosphere.	95
Fig. 4.2	From top panel to bottom panel, contour plots of the plasma density, the azimuthal magnetic field, the azimuthal velocity, the plasma pressure, and the magnetic pressure in Case A.	106
Fig. 4.3	Profiles of the plasma pressure ( $P$ ) along the radial direction at $z = 0$ in Case A.	109

Fig. 4.4	(a) Wave front position along the $z$ -direction, (b) the corresponding wave front velocity, and (c) the maximum values of $B_\theta$ and $ V_\theta $ in Case A.	111
Fig. 4.5	Contour plots of the currents (top) along the $r$ -direction ( $J_r$ ) and (bottom) along the $z$ -direction ( $J_z$ ) in Case A.	113
Fig. 4.6	The magnetic field lines in Case A.	114
Fig. 4.7	(Top) Contour plots of the azimuthal magnetic field, $B_\theta$ , and (bottom) the azimuthal velocity, $V_\theta$ , in Case B.	116
Fig. 4.8	(a) The propagation speed of the wave front along the $z$ -direction and (b) the maximum values of $B_\theta$ and $ V_\theta $ in Case B.	118
Fig. 4.9	(a) $B_{\theta\max}$ and $ V_\theta _{\max}$ values and (b) $B_{z\max}$ values for different flux tube lengths with $B_{\theta\max}(t=0) = 3 B_0$ .	120
Fig. 4.10	The propagation velocity of the Alfvén wave along the $z$ -direction for different azimuthal magnetic field components ( $B_{\theta\max}$ ).	122
Fig. 4.11	Same as Fig. 4.2, but for an initially given plasma vortex.	125
Fig. 4.12	Contour plots of the currents (top) along the $r$ -direction ( $J_r$ ) and (bottom) along the $z$ -direction ( $J_z$ ) for the above case.	127

## ACKNOWLEDGMENTS

It is my great pleasure to acknowledge some of the people who have helped me, directly or indirectly, from the preparation to the completion of this thesis. Although it is impossible to list all of them here, I must express my thanks to some of the key people in particular.

First, I would like to thank Prof. Lou-Chuang Lee, my advisor and the chairman of my advisory committee, for his steady advice, guidance, encouragement, inspiration, and financial support through five years of graduate study at the Geophysical Institute, University of Alaska Fairbanks. I deeply appreciate his support.

In addition, I wish to thank the other members of my advisory committee – Profs. Chuck Deehr, Dan Swift, Walter Tape, and Brenton Watkins – for their valuable suggestions, comments, and words of encouragement. In particular, Prof. Dan Swift has made many helpful comments which have greatly improved the thesis. Special thanks also are given to Profs. Zhu-Feng Fu and Shui Wang for their help and encouragement on this thesis project.

Many of my friends and fellow graduate students at the Geophysical Institute, Bill Bristow, Fei Cao, Gwang-Son Choe, Jim Conner, Nettie La Belle-Hamer, Zhiwei Ma, Qilong Min, Ming Yan, Lie Zhu, and others also provided invaluable help. I would like to thank them for their help directly or indirectly related with the completion of the thesis. In particular, Nettie deserves special thanks for helping me to improve my English significantly during the thesis work.

This work has been supported in part by the National Science Foundation grant ATM88-20992, the Department of Energy grant DE-FG06-86ER 13530, and the National Aeronautics and Space Administration grant NRA-89-ES SPTP-006 to the University of Alaska. The numerical calculations were made possible by the computer facilities in the Geophysical Institute and the Academic Computing System in the University of Alaska. Special thanks go to C. Rohwer, and K. D. Ramier.

Finally, I wish to express my gratitude to my wife, Lin Wang, for her understanding, encouragement, and support during this thesis work.

## CHAPTER 1

### Overview

The solar wind-magnetosphere interaction, one of the most fundamental processes in space plasma physics, includes the transfer of energy, momentum, and mass from the solar wind to the Earth's magnetosphere, and subsequently to the ionosphere. The magnetopause is the interface region between the shocked solar wind in the magnetosheath and the hot, low-density plasma in the Earth's magnetosphere, where these transfers take place. Satellite observations of plasmas during the magnetopause crossings indicate the existence of a boundary layer which contains magnetosheath-like plasma and is located earthward of the magnetopause. The part of the plasma boundary layer which is located at low to moderate latitudes is called the low-latitude boundary layer (LLBL), as shown in Figure 1.1 [Eastman *et al.*, 1976; Haerendel *et al.*, 1978; Eastman, 1979; Eastman and Hones, 1979; Sckopke *et al.*, 1981; Lundin and Dubinin, 1984, 1985; Phan *et al.*, 1989; Bryant and Riggs, 1989]. The high-latitude part of the plasma boundary layer which is located earthward of the tail magnetopause is called the plasma mantle [Akasofu *et al.*, 1973; Rosenbauer *et al.*, 1975; Sckopke *et al.*, 1976; Gosling *et al.*, 1985]. The plasma boundary layer near the dayside cusps is called the entry layer [Haerendel *et al.*, 1978]. Also shown in Figure 1.1 are the bow shock, the magnetosheath, the cusp, the tail lobe, and the plasma sheet.

As the solar wind flows toward the subsolar point of the magnetopause, it is diverted toward both the dawnside and duskside of the magnetosheath, as shown in Figure 1.2a, which shows the flow pattern in the equatorial plane of the magnetopause-boundary layer region. The flow bulk velocity parallel to the magnetopause is on the order of 100 – 300 km/s in

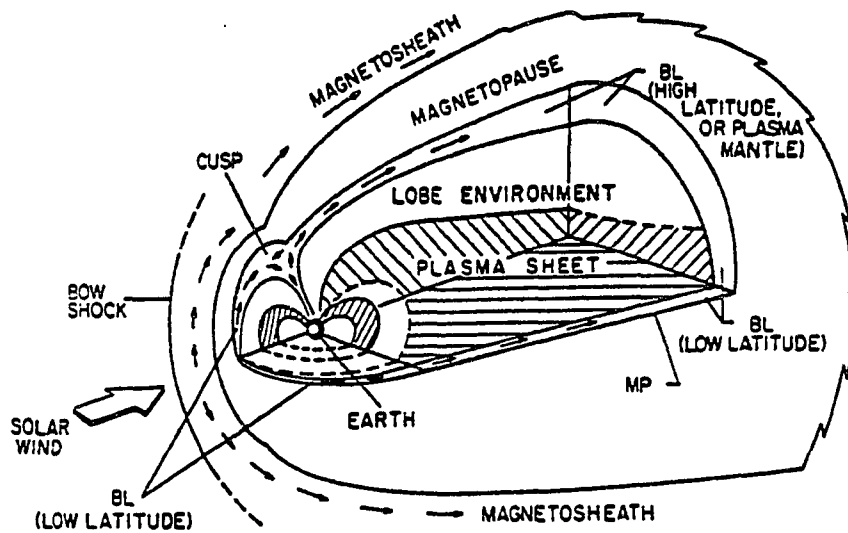


**Figure 1.1** A sketch of the Earth's magnetosphere showing the magnetopause and the boundary layer [Eastman, 1979]. In the figure, MP means the magnetopause and BL means the boundary layer.



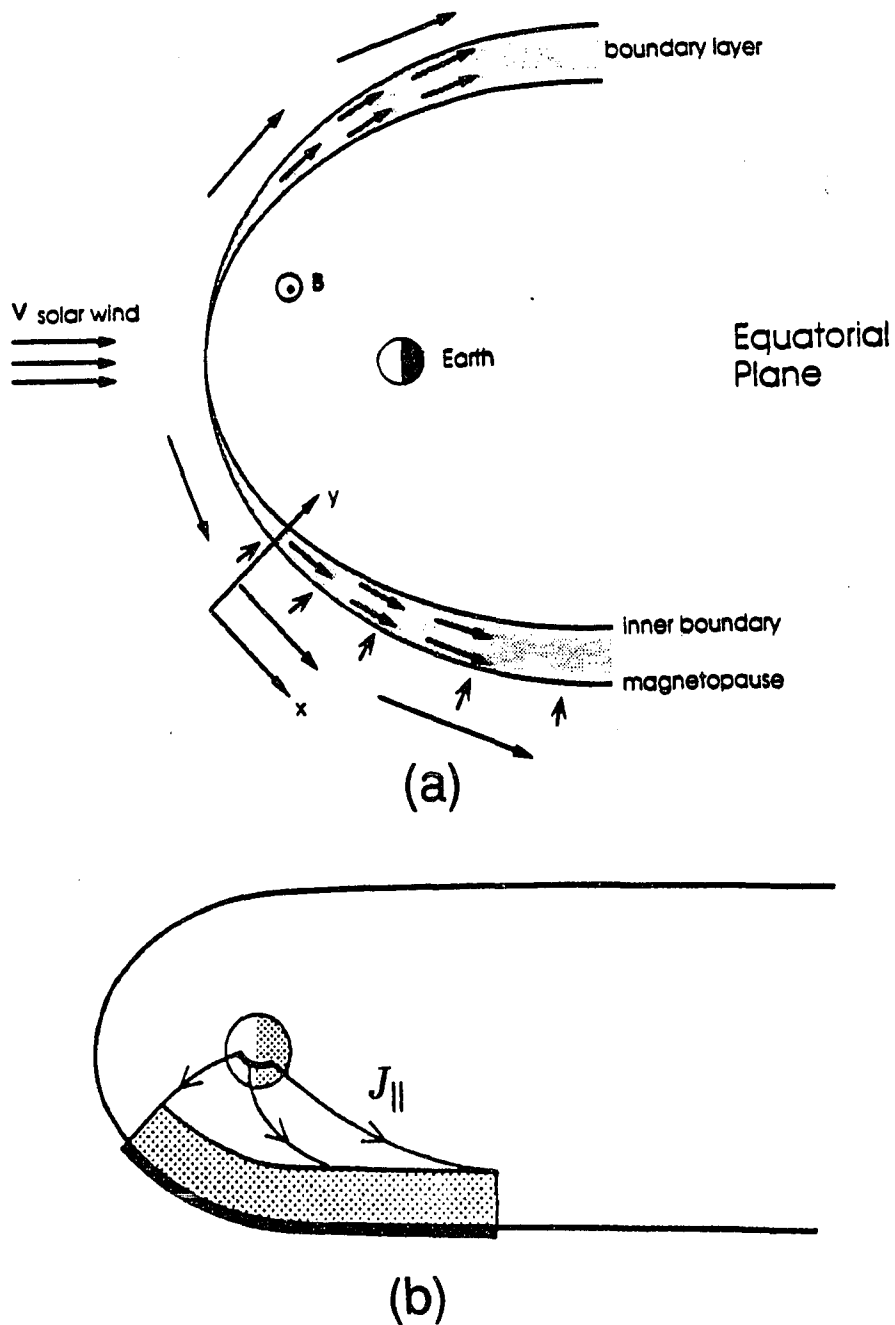


**Figure 1.2** Schematic sketches of interactions among the solar wind, the magnetosphere, and the ionosphere. (a) The low-latitude boundary layer (shaded area) in the Earth's equatorial plane and (b) the coupling of the duskside region of the boundary layer to the post-noon sector of the ionosphere via the field-aligned currents.

the magnetosheath, while it is nearly zero at the inner boundary of the boundary layer. This velocity difference across the boundary layer will cause a sheared plasma flow, which in turn causes vortex motion in the boundary layer region. The vortex associated with the sheared plasma flow is clockwise in the dawnside region of the boundary layer and counterclockwise in the duskside region of the boundary layer. In addition, there may exist a normal diffusion flux with a velocity on the order of 2 – 10 km/s in some regions of the magnetopause, as shown schematically in Figure 1.2a [Eastman, 1979]. The justification of the existence of this normal diffusion flux may be found later in this thesis.

The vortex motion caused by the sheared plasma flow in the boundary layer will produce a localized convection electric field, which in turn produces polarization charges in the magnetosphere. The counterclockwise vortex produces negative space charges in the duskside region, while the clockwise vortex produces positive space charges in the dawnside region. The polarization charges can be discharged to the conducting ionosphere through field-aligned currents (FACs), which are limited by the finite conductivities in the ionosphere. The dominant FAC flows upward (downward) in the duskside (dawnside) region of the boundary layer. Figure 1.2b is a sketch of this coupling process between the magnetopause-boundary layer region and the polar ionosphere through the field-aligned currents. Note that the FACs flow upward from the post-noon sector in the polar ionosphere to the duskside region of the boundary layer. The presence of the finite ionospheric conductivity will exert a dragging force on the plasma flow in the magnetosphere. The dragging effect of the ionosphere may slow down the convection speed of the plasma flow and cause the decay of the plasma vortices in the magnetosphere. Therefore, the dynamics of the magnetosphere and the ionosphere are intrinsically connected. Some ionospheric signatures may be explained by the development of the Kelvin-Helmholtz (KH) instability in the presence of the competing effect of the formation

of vortices in the magnetosphere and the decay of vortices in the ionosphere. The observed spatially periodic auroral bright spots in the ionosphere may be one of the examples [Lui *et al.*, 1987, 1989; Potemra *et al.*, 1990].

When coupled to the ionosphere, the plasma vortices generated in the magnetopause-boundary layer region also produce the ionospheric and ground signatures. The magnetic impulse events observed in the ionosphere and on the ground are signatures of this coupling through FACs [Lanzerotti *et al.*, 1986, 1987, 1990; Friis-Christensen *et al.*, 1988; Glassmeier *et al.*, 1989]. Based on magnetometer observations of multiple ground stations, the presence of the vortices in the ionospheric Hall current pattern can be identified. Figure 1.3 is a schematic representation of physical processes related to an observed magnetic impulse event [Glassmeier *et al.*, 1989]. Near the equatorial plane of the magnetopause-boundary layer region, the current system is driven by the plasma vortices. The corresponding convection electric field is similar to that of an electric dipole. FACs associated with the twin vortices flow downward in the west and upward in the east, which produce the ground-equivalent current structure, or the ground magnetic perturbations if the current pattern is rotated  $90^\circ$  counterclockwise. The twin-vortex structure is clockwise in the west and counterclockwise in the east.

In the following, observations of the magnetopause-boundary layer, auroral bright spots, and magnetic impulse events are further discussed. Previous theoretical and simulation work related to these observations is summarized. Finally, an outline of the thesis is given at the end of this chapter.

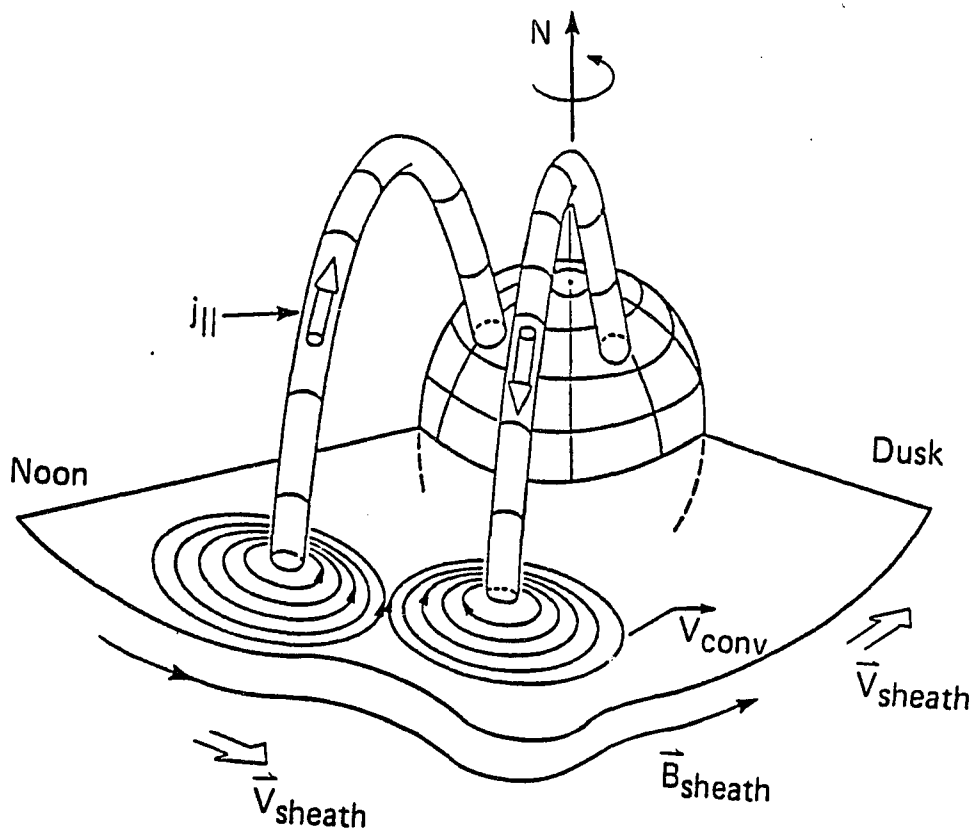


**Figure 1.3** Schematic representation of physical processes related to the observed magnetic impulse event on December 24, 1978. Shown are the two magnetic flux tubes carrying field-aligned current as suggested by the ground magnetic observations. The poleward and outward motion of these flux tubes is indicated as well as the convection flow pattern in the magnetospheric equatorial plane [Glassmeier *et al.*, 1989].

## 1.1 Observations of the Magnetopause-Boundary Layer

Satellite observations of the low-latitude boundary layer indicate that the boundary layer thickness is highly variable and appears to increase with increasing longitudinal distance from the subsolar point [Eastman, 1979; Eastman and Hones, 1979]. The thickness of the LLBL ranges from 0.1 to 2  $R_E$  (Earth radius). The plasma density and the flow velocity are also highly variable in the boundary layer region, showing vortex structures [Sckopke et al., 1981]. A density plateau is often observed in the boundary layer region (a constant density region with the density value between those in the magnetosheath and in the magnetosphere) [e.g., Haerendel et al., 1978; Paschmann et al., 1978; Sckopke et al., 1981]. The LLBL is bounded on one side by the magnetopause which has the high-density magnetosheath plasma with a high-speed flow and is bounded along its inner surface by the low-density, low flow speed, and high thermal energy magnetospheric plasma [Haerendel et al., 1978; Eastman, 1979; Sckopke et al., 1981; Bryant and Riggs, 1989]. The thickness of the low-latitude boundary layer is positively correlated with a northward interplanetary magnetic field (IMF) [Haerendel et al., 1978; Mitchell et al., 1987]. The magnetic field in the boundary layer region shows a very small variation and is similar to the magnetic field in the neighboring magnetosphere. The direction of the plasma flow is nearly perpendicular to the magnetic field [Eastman, 1979; Sckopke et al., 1981].

The plasma in the boundary layer consists of the cold intense magnetosheath-like plasma and the hot tenuous magnetosphere-like plasma. Figure 1.4 shows an example of plasma and magnetic field data from the ISEE 1 outbound traversal of the outer magnetosphere and the magnetosheath on November 6, 1977 [Sckopke et al., 1981]. The boundary layer region continued for  $\sim 50$  min (as can be seen from the density profile in the top panel), during

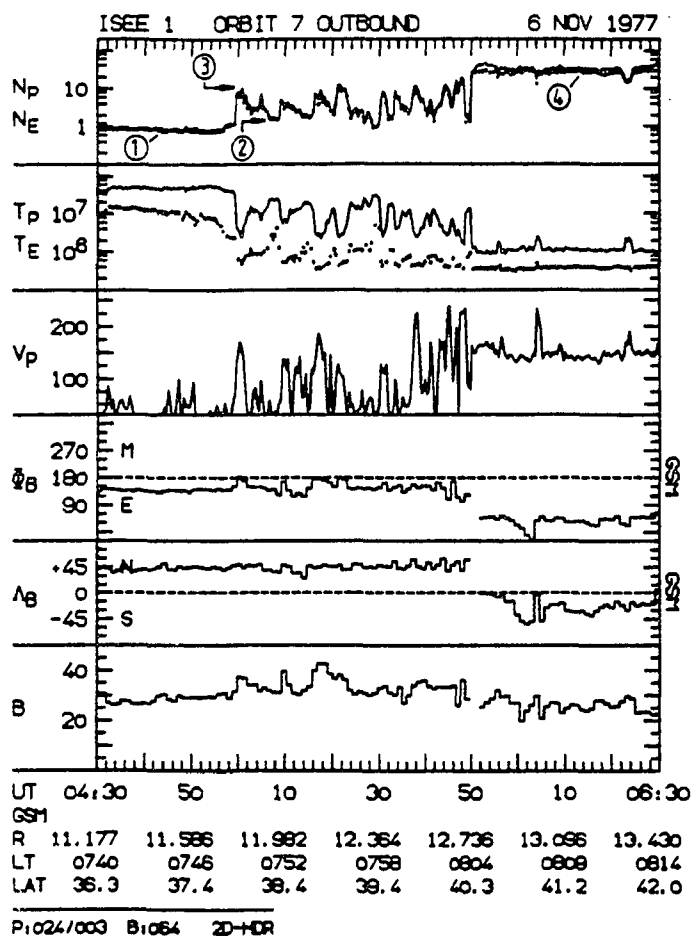


**Figure 1.4** Plasma and magnetic field data from an ISEE outbound pass through the outer magnetosphere, low-latitude boundary layer, and magnetosheath, near 0800 LT and 40° northern GSM latitude. The plasma parameters are from top to bottom, proton ( $N_p$ ) and electron ( $N_e$ ) densities in units of  $\text{cm}^{-3}$  as solid curves and solid circles, temperature  $T_p$  and  $T_e$  in degrees of Kelvin, and proton bulk velocity ( $v_p$ ) in kilometers per second.  $\phi_B$  and  $\Lambda_B$  are the GSM azimuth and elevation angles, respectively. The bottom panel shows magnetic field data in nanoteslas [Sckopke *et al.*, 1981].

which time the satellite traveled outward a distance of more than  $1 R_E$ . At about 0550 UT, the satellite crossed the magnetopause and entered the magnetosheath. The highly variable density structures can be seen from the density profile. The plasma bulk velocity (the third panel of Figure 1.4) in the boundary layer is generally correlated with the plasma density, namely, the bulk velocity approaches the magnetosheath level where the boundary layer plasma has a high density. The bulk velocity generally starts to increase with the density increase at the boundary layer transitions. However, some observations do not show such a clear correlation [Haerendel *et al.*, 1978; Eastman, 1979; Sckopke *et al.*, 1981]. The magnetic field in the bottom panel of Figure 1.4 shows a small variation in the boundary layer region. Sckopke *et al.* [1981] suggested that the vortex structure may be formed as a consequence of the development of the KH instability in the low-latitude boundary layer region.

Song *et al.* [1990] examined the magnetopause-boundary layer structure and properties for the ISEE 1 magnetopause-boundary layer crossings which occur near the subsolar point when the IMF was strongly northward. They found that the magnetopause-boundary layer is composed of three layers, a magnetosheath transition layer, an outer boundary layer, and an inner boundary layer. In each of the boundary layers, the plasma can be interpreted as simple mixtures of the magnetosheath and the magnetospheric plasmas. The boundaries among these layers are sharp (less than an ion gyroradius).

## 1.2 Observations of Auroral Bright Spots

Satellite observations of dayside auroral forms have shown the presence of spatially periodic bright spots aligned on the post-noon auroral oval, ranging from 1400 to 1600 magnetic local time (MLT) [e.g., Cogger *et al.*, 1977; Evans, 1985; Bythrow *et al.*, 1986;

*Lui et al.*, 1987, 1989; *Potemra et al.*, 1990]. The auroral luminosity of these localized bright spots can be comparable to that of nightside discrete auroras associated with substorm activities. Using data from the scanning auroral photometer on ISIS-2 satellite, *Cogger et al.* [1977] found that a persistent auroral intensity enhancement occurs between the 1400 to 1600 MLT, which is probably related to a statistically deduced maximum in particle fluxes observed in this sector. *Iijima and Potemra* [1978] found that the most intense upward region 1 FACs are located in the 1400 to 1600 MLT sector, while the most intense downward region 1 FACs are located in the 0800 to 1000 MLT sector. *Bythrow et al.* [1981] found that a portion of region 1 FAC on the dayside is coincident with the extension of the low-latitude boundary layer in the magnetosphere. *Evans* [1985] studied measurements of precipitating particle energy flux obtained with TIROS/NOAA satellite and also found a local intensity maximum in electron flux in the post-noon sector. Recent studies of magnetic field and energetic particle data obtained from satellites indicate that the dayside region 1 FAC flows primarily through the cusp and the low-latitude boundary layer [*Bythrow et al.*, 1981, 1988; *Erlandson et al.*, 1988; *Potemra et al.*, 1990]. *Murphree et al.* [1981] found that auroral morphology in the post-noon sector is controlled by the  $B_y$  component of the interplanetary magnetic field.

Figure 1.5 shows an example of the commonly observed periodic, localized regions of auroral intensity enhancements from the Viking satellite in the post-noon sector on May 3, 1986 [*Lui et al.*, 1989]. The image was taken at 0948:16 UT by a camera which monitors the 1304-Å emission from atomic oxygen. Figure 1.5 is reproduced from a color figure. The white regions indicate the high intensity and the black regions indicate the low intensity. Four bright spots (white regions in Figure 1.5) observed in the post-noon sector are located at about 1312, 1406, 1506, and 1548 MLT with approximate separation of about 0.7 – 1.1 hours in the



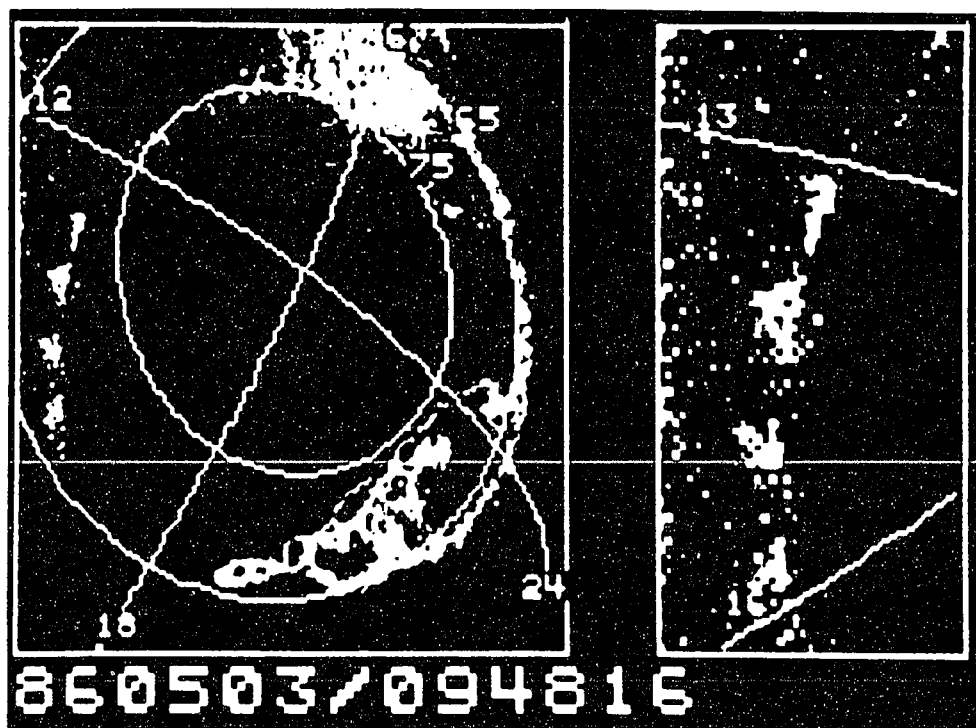


**Figure 1.5** An auroral image from the ultraviolet imager on the Viking satellite taken on May 3, 1986, at 0948:16 UT. Magnetic local time meridians are superimposed on the left image for reference. The white regions indicate the high intensity and the black regions indicate the low intensity. This image shows the occurrence of four bright spots in the post-noon sector along the auroral oval [Lui *et al.*, 1989].

MLT. The spatial dimension of these spots (i.e, the dimension of the area above diffuse aurora background luminosity) ranges approximately from 50 to 200 km, the separation between two successive spots is about 100 – 500 km, and the total range of all spots is more than 1000 km. The region of the bright spots is shown in more detail in the right portion of the figure, where the MLT range from 1300 to 1600 is emphasized. This event is seen during a substorm, as can be seen by the presence of a large auroral bulge on the nightside. *Lui et al.* [1989] suggested that these bright spots are related to the small-scale FAC resulting from the dynamic change of vorticity associated with the KH instability occurring in the LLBL of the magnetosphere.

*Potemra et al.* [1990] studied similar periodic auroral bright features obtained by ultraviolet images on the Viking satellite. They showed a case with a distinctive series of periodic bright spots in the post-noon region. These periodic bright spots are aligned in the east-west direction which persist for nearly 30 min. The spots are embedded in a continuous band of the ultraviolet emission that extends from about the 1300 to 1800 MLT at magnetic latitudes from about  $77^\circ$  to  $74^\circ$ . Magnetic field and hot plasma measurements confirmed that these bright spots are colocated with the field line projection of the upward field-aligned current and precipitating energetic ( $\sim 200$  ev) electrons. The results of their study support the view that large-scale oscillations of magnetospheric boundaries, possibly associated with the KH instability, can modulate currents, particles, and auroral forms [*Bythrow et al.*, 1986; *Lui et al.*, 1989; *Potemra et al.*, 1990].

In addition, optical and ion drift observations of auroral bright spot sequence near the 1400 MLT [*Sandholt et al.*, 1990] show that the auroral events cover about 300 km in east-west extent, move eastward (tailward) along the poleward boundary of the persistent background aurora with a velocity of  $\sim 1.5$  km/s.

### 1.3 Magnetic Impulse Events

Ionospheric and ground observations of magnetic impulse events at high latitudes indicate that many magnetic impulse events could be interpreted in terms of intense FACs above the observing stations and are related to the plasma vortices generated in the magnetopause-boundary layer region [Lanzerotti *et al.*, 1986, 1987, 1990; Friis-Christensen *et al.*, 1988; Glassmeier *et al.*, 1989; Olson, 1989]. Lanzerotti *et al.* [1986, 1990] found that most of the impulse events have a half-width of a few minutes in time and are reasonably conjugate. The amplitudes are of about 20 nT to 50 – 100 nT [Friis-Christensen *et al.*, 1988; Glassmeier *et al.*, 1989; Lanzerotti *et al.*, 1990]. The majority of the events have magnetic perturbations in the vertical component which can be interpreted in terms of FACs directed in the same direction (either into or out of the ionosphere) in both hemispheres. The perturbations in the horizontal plane exhibit a vortex-like structure, either single vortex, or twin vortices, or multiple vortices [Friis-Christensen *et al.*, 1988; Glassmeier *et al.*, 1989; McHenry *et al.*, 1988, 1990; Lanzerotti *et al.*, 1990].

Lanzerotti *et al.* [1990] studied magnetic field data acquired at high-latitude, near-conjugate stations. They observed spike-like magnetic field variations with time scales of a few minutes in the conjugate ionospheres. Figure 1.6 shows two magnetic impulse events, one at 1233 UT and the other at 1340 UT. The large, spike-like events have amplitude of magnetic component  $\sim 50 - 100$  nT. The vertical (V), the north-south (H), and the east-west (D) components show uni-polar, semi-bipolar or bi-polar spikes. The vertical components of the magnetic perturbations may be explained by a single ionospheric Hall current loop [Lee, 1986], a dual-loop [Southwood, 1987], or more complicated Hall current patterns in the ionosphere [Lanzerotti *et al.*, 1990].

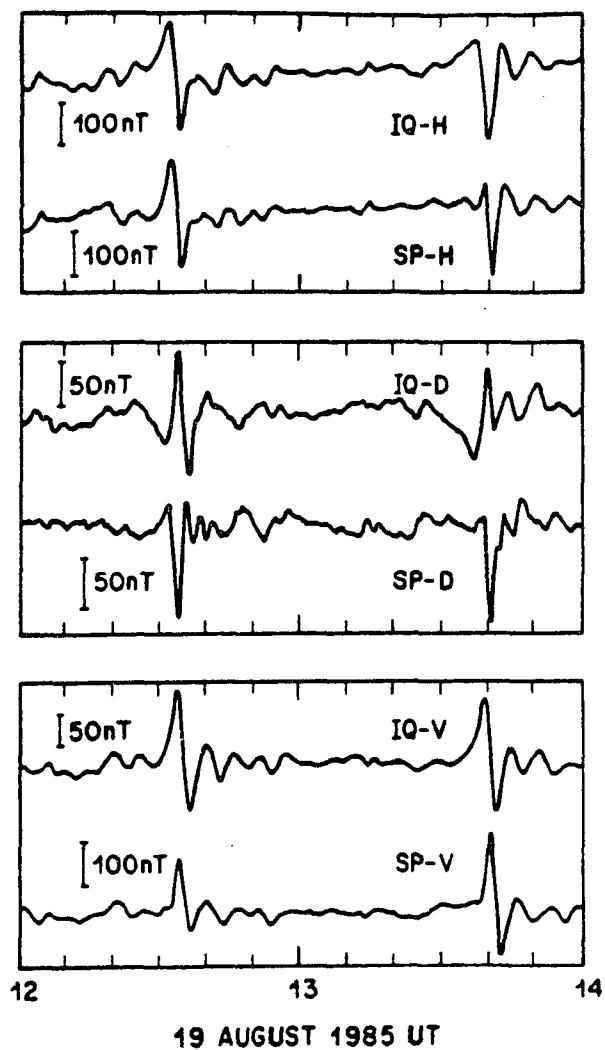


**Figure 1.6** Magnetic field traces from two ground stations for a 2-hour interval 1200 – 1400 UT on August 19, 1985. One station is at IQ (Iqaluit, invariant latitude  $74.0^\circ$ ) and the other is at SP (South Pole Station, invariant latitude  $74.8^\circ$ ). Magnetic field is shown for the north-south (H), east-west (D), and vertical (V) components [Lanzerotti *et al.*, 1990].

*McHenry et al.* [1990] detected several classes of traveling vortices in the dayside ionospheric convection using the Greenland magnetometer chain [*Friis-Christensen et al.*, 1988; *McHenry et al.*, 1988, 1990]. One class shows the signatures of localized ionospheric traveling convection vortices, which consist of a twin-vortex pattern of convection consistent with the presence of two FAC filaments [*Friis-Christensen et al.*, 1988]. This system of currents is observed to move westward at about 4 km/s. Another class observed consists of a continuous series of vortices moving generally westward for several hours at a time [*McHenry et al.*, 1988, 1990]. The vortex strength is seen to be approximately steady and neighboring vortices rotate in opposite directions. Satellite observations at the low altitude indicate that the vortices are on magnetic field lines which map to the inner edge of the low-latitude boundary layer. They suggested that these vortices are related to the plasma vortices, which are caused by the Kelvin-Helmholtz instability in the magnetopause-boundary layer region [*McHenry et al.*, 1988, 1990].

#### **1.4 Previous Theoretical and Simulation Work**

One of the basic mechanisms which transfer solar wind energy, momentum, and mass into the Earth's magnetosphere at the dayside magnetopause is the viscous interaction, which was originally proposed by *Axford and Hines* [1961]. In their model, as the solar wind plasma flows around the magnetopause, the viscous interaction between the solar wind and the Earth's magnetosphere can allow the solar wind mass and momentum to diffuse or penetrate into closed magnetospheric magnetic field lines. Although the classical kinematic viscosity is expected to be very low in the space plasma, a sufficiently large anomalous viscosity may be provided by the Kelvin-Helmholtz instability [e.g., *Southwood*, 1968; *Sckopke et al.*, 1981;

*Lee et al.*, 1981; *Miura*, 1984; *Pu and Kivelson*, 1983; *Wu*, 1986; *La Belle-Hamer et al.*, 1988] or particles being scattered by plasma waves, probably lower hybrid waves [*Huba et al.*, 1977; *Gary and Eastman*, 1979; *Lee*, 1982; *Tsurutani and Thorne*, 1982]. However, the KH instability can only account for the momentum transport; it alone cannot lead to the transport of mass into the magnetosphere [*Miura*, 1984]. The transport of particles through the magnetopause is most probably caused by plasma waves. The low-latitude boundary layer, through coupling to the ionosphere by field-aligned currents, may act as an MHD-dynamo, which converts the plasma flow energy into electric energy. *Eastman et al.* [1976] reported satellite observations in support of such a momentum exchange process.

*Miura* [1984] carried out a magnetohydrodynamic (MHD) simulation of the Kelvin-Helmholtz instability in a compressible plasma for both parallel ( $\mathbf{v}_0 \perp \mathbf{B}_0$ ) and transverse ( $\mathbf{v}_0 \parallel \mathbf{B}_0$ ) configurations, modeling the high-latitude and the dayside low-latitude boundary layers of the magnetosphere. The anomalous viscosity can be estimated from the simulation results. The diffusion coefficient associated with the Kelvin-Helmholtz instability is found to be on the order of  $10^9$  m<sup>2</sup>/s, which is comparable to the requirements of the viscous-like interaction hypothesis by *Axford and Hines* [1961]. The instability results in a vortex flow for the transverse configuration.

As have been stated previously, the Kelvin-Helmholtz instability in the low-latitude boundary layer [*Lee et al.*, 1981; *Miura*, 1984] may generate the vortex-like motions [*Lee et al.*, 1981; *Sckopke et al.*, 1981], be responsible for the occurrence of spatially periodic auroral bright spots [*Lui et al.*, 1989; *Potemra et al.*, 1990], and produce the magnetic impulse events [*McHenry et al.*, 1988, 1990]. Other physical processes at the dayside magnetopause may also produce similar ionospheric and ground signatures through the magnetosphere-ionosphere interactions via FACs, such as flux transfer events (FTEs) [*Goertz et al.*, 1985;

*Sandholt et al.*, 1986; *Lee*, 1986; *Lee et al.*, 1988; *Scholer*, 1988; *Lanzerotti et al.*, 1986, 1990], solar wind dynamic pressure pulses [*Friis-Christensen et al.*, 1988; *Glassmeier et al.*, 1989; *Sibeck*, 1990], and the impulsive plasma penetration across the magnetopause [*Lemaire*, 1977; *Schindler*, 1979; *Heikkila*, 1982; *Ma et al.*, 1991].

In the above-mentioned efforts, many aspects of the interactions between the magnetopause-boundary layer region and the polar ionosphere remain unclear. The objective of this thesis is to obtain a better understanding of the coupling of the plasma vortices formed in the magnetopause-boundary layer region to the polar ionosphere through numerical simulations.

### 1.5 Outline of the Thesis

In Chapter 2, the plasma dynamics and structure of the magnetopause-boundary layer region are studied on the basis of a two-dimensional incompressible magnetohydrodynamic simulation code. In the simulation, the magnetosheath plasma is driven into the boundary layer region by imposing a diffusion flux along the magnetopause. The simulation results are compared with the plasma observations at the magnetopause-boundary layer region.

In Chapter 3, the formation of the observed spatially periodic auroral bright spots is studied by using a self-consistent magnetosphere-ionosphere coupling model. The coupling model is an incompressible fluid model for the plasma flow dynamics in the low-latitude boundary layer and its interaction with the polar ionosphere via field-aligned currents and a parallel electric field, which consists of three parts: the low-latitude boundary layer in the magnetosphere, the polar ionosphere, and the field-aligned region. In the present model, the ionospheric conductivity is allowed to be enhanced due to precipitation of the accelerated

electrons in the upward field-aligned current regions. The Alfvén transit time between the magnetosphere and the ionosphere is assumed to be very short and neglected.

In Chapter 4, the generation and propagation of large-amplitude Alfvén waves associated with the evolution of localized plasma vortices, as well as localized magnetic flux ropes, along magnetic field lines are studied. A two-dimensional compressible magnetohydrodynamic simulation code in the cylindrical coordinates is used. The Alfvén waves carry field-aligned currents and provide the link for the coupling of plasma vortices and magnetic flux ropes in the magnetosphere to the polar ionosphere.

The summary and discussion are presented in Chapter 5.



## CHAPTER 2

### Vortex Structures in the Low-Latitude Boundary Layer

#### 2.1 Introduction

As mentioned in Chapter 1, the magnetopause-boundary layer region is the interface region between the solar wind and the Earth's magnetosphere. A sheared plasma flow exists in the magnetopause-boundary layer region, which may lead to the development of the Kelvin-Helmholtz (KH) instability. In addition, a normal diffusion flux exists in some regions of the magnetopause [Eastman, 1979]. It has been shown that some geomagnetic pulsations ( $P_c$  4 – 5, 45 – 600 s period) may be generated by the Kelvin-Helmholtz instability in the boundary layer [Southwood, 1968; Olson and Rostoker, 1978; Lee and Olson, 1980; Olson, 1986; Wolfe *et al.*, 1987]. Lee and Olson [1980] showed that the observed local time variation of dayside geomagnetic micropulsations is consistent with a generation mechanism due to the KH instability operating at the magnetopause. Olson [1986] showed that the pulsations are broad band, strongest near noon, and presumed related to the cusp. Statistical studies [Wolfe *et al.*, 1987] have also shown a correlation between pulsations in the  $P_c$  3 to  $P_c$  4 band and the solar wind speed. These findings support the generation mechanism due to the KH instability. It is also found that some geomagnetic pulsations in the  $P_c$  4 – 5 range are associated with traveling ionospheric flow vortices produced by moving FAC filaments which appear to originate near the inner edge of the LLBL. The generation of these vortices may be related to the KH instability due to the sheared plasma flow [McHenry *et al.*, 1988; 1990].

*Lee et al.* [1981] used a three-layer model to study the Kelvin-Helmholtz instability in the magnetopause-boundary layer region. The three uniform incompressible regions are separated by two idealized sharp boundaries, namely, the magnetopause and the inner boundary of the boundary layer. They found that the most unstable mode occurs at the inner boundary of the boundary layer (inner mode). An unstable mode also occurs at the magnetopause (magnetopause mode) which is unstable only for a magnetopause velocity shear larger than a critical value. This critical value depends on the magnitude and direction of both the magnetosheath magnetic field and the velocity fields on either side of the magnetopause. With the development of the inner mode, a large variation in the plasma density and the flow velocity is seen at the inner boundary, but not much variation is seen at the magnetopause. The observed variation in the low-latitude boundary layer may be due to the development of this inner mode. The corresponding compressible analysis confirmed the above conclusion [*Lin and Tschu*, 1988].

Based on a statistical study, *Eastman* [1979] found that in order to account for the observed thickness of the boundary layer there must exist, on the average, a diffusion flux with an inward normal velocity. The average inward normal velocity  $\langle v_n \rangle$  may be estimated as follows. As mentioned earlier, the boundary layer thickness ( $L_{BL}$ ) is observed to increase with increasing longitudinal distance from the subsolar point. At the dawn-dusk meridian, the boundary layer thickness is, typically,  $L_{BL} \simeq 0.5 R_E$  [*Eastman*, 1979]. The length of the magnetopause from the subsolar point to the dawn-dusk meridian can be estimated as  $S \simeq 16 R_E$ . The typical boundary layer flow velocity parallel to the magnetopause is  $v_t \simeq 200$  km/s. If the plasma density in the magnetosheath and in the boundary layer is assumed to remain constant, the conservation of particle flux gives  $L_{BL}v_t = S \langle v_n \rangle$ . For  $S \simeq 16 R_E$ ,  $v_t \simeq 200$  km/s, and  $L_{BL} \simeq 0.5 R_E$ , then the average diffusion velocity will be  $\langle v_n \rangle \simeq 6$

km/s. Note that although the diffusion can permit the magnetosheath plasma to penetrate into the magnetosphere, the diffusion alone can only produce a smoothly distributed density profile in the boundary layer. It cannot explain the observed vortex structures, as shown in Figure 1.4, or the formation of the density plateau in the boundary layer.

The nonzero diffusion velocity ( $\langle v_n \rangle \neq 0$ ) at the magnetopause can be due to the electrostatic and electromagnetic plasma waves observed at the magnetopause [Gurnett *et al.*, 1979; Anderson *et al.*, 1982; Tsurutani *et al.*, 1981; LaBelle and Treumann, 1988]. These plasma waves may be generated by the lower hybrid drift instability, the ion two-stream instability, or the modified two-stream instability at the magnetopause [Gary and Eastman, 1979; Lee, 1982; Tsurutani and Thorne, 1982]. The wave-particle interactions in the presence of the observed plasma waves may lead to an effective transport of particles from the magnetosheath to the magnetosphere. The ion diffusion coefficient  $D_{\perp}$  associated with these waves has been estimated to be  $D_{\perp} \simeq 10^9$  m<sup>2</sup>/s [Tsurutani and Thorne, 1982; Gary and Sgro, 1990]. For the observed thickness of the magnetopause,  $L_{MP} \simeq 100 - 500$  km, the average diffusion velocity can be estimated as  $V_D = D_{\perp}/L_{MP} \simeq 2 - 10$  km/s, which is of the order of the inflow speed estimated earlier.

The purpose of this chapter is to study the plasma dynamics in the magnetopause-boundary layer region in an attempt to explain the vortex structures observed in the boundary layer. This study is based on numerical simulations which use a two-dimensional incompressible MHD code. In the simulation, a normal diffusion flux with a velocity of  $\sim 2 - 10$  km/s is assumed to exist at the magnetopause to account for the sources at the magnetopause. Specifically, it is found that the Kelvin-Helmholtz instability can lead to the observed vortex structures in the boundary layer as suggested by Sckopke *et al.* [1981] and Lee *et al.* [1981]. It is also found that the boundary layer thickness increases with increasing longitudinal distance

from the subsolar point. A mixed region is formed where the magnetosheath plasma and the magnetospheric plasma mix due to the vortex motions. In the later stage of development, a density plateau is formed in the central part of the boundary layer.

This chapter is organized in the following way. Section 2.2 describes the simulation model and numerical scheme. The simulation results are presented in section 2.3. Section 2.4 summarizes the major results presented and their comparisons with observations in the low-latitude boundary layer.

## **2.2 Simulation Model and Numerical Scheme**

In this section, the simulation model, the governing equations, the differencing scheme, and the boundary conditions are presented.

### **2.2.1 Simulation Model and Governing Equations**

Consider the equatorial plane of the magnetopause-boundary layer region, as shown in Figure 1.2a. As the solar wind flows toward the subsolar point of the magnetopause, it is diverted toward both the dawnside and the duskside regions of the magnetosheath. The bulk velocity parallel to the magnetopause is of the order of 100 – 300 km/s in the magnetosheath. In addition, there may exist a normal diffusion flux with a velocity of the order of 2 – 10 km/s in some regions of the magnetopause, as shown schematically in Figure 1.2a. As has been mentioned in Chapter 1, the vortex associated with the sheared plasma flow is counterclockwise (clockwise) in the duskside (dawnside) region of the boundary layer, which will lead to the presence of localized upward (downward) FAC filaments in the post-noon (pre-noon) sector of both the northern and the southern polar ionospheres.

In this chapter the simulation domain is chosen to be a rectangular box in the  $x$ - $y$  plane extending from 0 to  $L_x$  in the  $x$ -direction (along the magnetopause) and from 0 to  $L_y$  in the  $y$ -direction (inward toward the Earth), as shown in Figure 2.1. The  $x$ -axis is along the magnetopause and points from the subsolar region to the magnetotail. The  $y$ -axis is perpendicular to the magnetopause and points from the magnetopause to the Earth. For simplicity the magnetopause is assumed to be a straight line ( $y = 0$ ) in the simulation model. The simulation domain is chosen to be the equatorial plane since the Kelvin-Helmholtz instability occurs only when the wave vector,  $\mathbf{k}$ , is nearly perpendicular to the magnetic field,  $\mathbf{B}$  [Lee *et al.*, 1981].

In the present simulation the magnetopause is treated as a fixed boundary with an effective diffusion flux. The macroscopic motion of the magnetopause is neglected in the simulation model. The use of an effective diffusion flux in the present simulation model is an attempt to partially include the effects of the microscopic wave-particle interactions at the magnetopause, as discussed in section 2.1. Theoretical analysis and simulation results show that the magnetopause is relatively stable to the Kelvin-Helmholtz instability and the most unstable mode occurs at the inner edge of the boundary layer [Lee *et al.*, 1981; Ogilvie and Fitzenreiter, 1989]. This is due to the fact that the magnetosheath magnetic field is generally not parallel to the magnetic field on the magnetospheric side and the tension force of the magnetic field tends to stabilize the KH instability. However, the assumption of a fixed magnetopause becomes invalid when the magnetic fields on the two sides of the magnetopause are nearly parallel or antiparallel, or when the pressure fluctuation in the magnetosheath is large.

Based on the observations discussed in Chapter 1, the magnetic field of the magnetosphere is nearly perpendicular to the equatorial plane in the low-latitude boundary layer and

## The Low-Latitude Boundary Layer in the Equatorial Plane

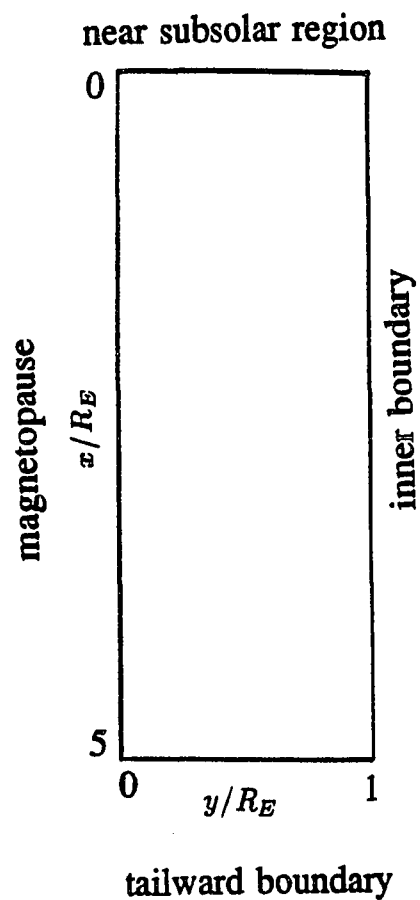


**Figure 2.1** Schematic sketch of the simulation domain in the equatorial plane of the magnetosphere. The left boundary ( $y = 0$ ) is the magnetopause, the right boundary ( $y = L_y = 1R_E$ ) is the inner boundary, the upper boundary ( $x = 0$ ) is a boundary near the subsolar region, and the lower boundary ( $x = L_x = 5R_E$ ) is a boundary near the tailward region of the boundary layer.

the variation of the magnetic field is small. For simplicity, the magnetic field is assumed initially to be a constant and perpendicular to the simulation plane (i.e.,  $\mathbf{B} = B_z \hat{\mathbf{z}} = \text{constant}$ ). For a two-dimensional incompressible flow, it can be shown that if  $B_x = B_y = 0$  and  $B_z = \text{constant}$  initially as assumed in this chapter, the magnetic field will remain at the initial constant value for time  $t > 0$ .

Under the assumptions of the incompressibility and a constant perpendicular magnetic field ( $B_x = B_y = 0$ ,  $B_z = \text{constant}$ ), the two-dimensional magnetohydrodynamic equations governing the plasma behavior can be reduced to the following incompressible Navier-Stokes equations:

$$\frac{\partial N}{\partial t} = -\mathbf{v} \cdot \nabla N \quad (2.1)$$

$$\frac{\partial \Omega}{\partial t} = -\mathbf{v} \cdot \nabla \Omega + \nu \nabla^2 \Omega \quad (2.2)$$

$$\mathbf{v} = \nabla \psi \times \hat{\mathbf{z}} \quad (2.3)$$

$$\nabla^2 \psi = -\Omega \quad (2.4)$$

where  $N$  is the plasma number density,  $\mathbf{v}$  is the flow velocity in the  $x$ - $y$  plane,  $\nu$  is the kinematic viscosity,  $\psi$  is the streamline function, and  $\Omega$  is the vorticity function in the  $z$ -direction. For simplicity, we have set  $v_z = 0$ . Note that the variation of the plasma density will not cause changes in the streamline function or the flow pattern.

In this chapter, the length is normalized by a characteristic length,  $a$ ; the velocity by the plasma velocity parallel to the magnetopause,  $V_0$ ; the density by the magnetospheric uniform plasma density,  $N_0$ ; the time by the characteristic time,  $t_0 \equiv a/V_0$ ; the vorticity by  $V_0/a$ ; and the kinematic viscosity by  $aV_0$ . The Reynolds number is defined as  $R = aV_0/\nu$ . We choose  $a = 1 R_E$  in this chapter, where  $R_E$  is the Earth radius. Based on observations,

values for some of the normalizations are given as follows:  $V_0 = 200$  km/s,  $N_0 = 1$  cm<sup>-3</sup>, and  $t_0 = 32$  s.

### 2.2.2 Differencing Scheme and Numerical Procedure

In order to simulate vortex structures in the boundary layer, the effects of numerical errors should be minimized. If the numerical diffusion is too large, the small-scale structures will diffuse away and a smooth transition region will quickly form in the boundary layer. To reduce the numerical errors, a high-order finite differencing scheme is developed as described below.

1. A two-step method is used to time-center the time derivatives. This gives a second-order accuracy in time step  $\Delta t$  (i.e., the truncation errors  $\sim O(\Delta t^2)$ ).

2. For the convective terms  $\mathbf{v} \cdot \nabla N$  and  $\mathbf{v} \cdot \nabla \Omega$ , a differencing scheme accurate to the third-order in spatial grid size  $\Delta x$  or  $\Delta y$  is used. For the purpose of illustration, the differencing scheme for the convective terms in the one-dimensional case is

$$\left(v \frac{\partial f}{\partial x}\right)_i = \begin{cases} v_i \left( \lambda \frac{f_{i+1} - f_{i-1}}{2\Delta x} + (1 - \lambda) \frac{f_{i-2} + 3f_i - 4f_{i-1}}{2\Delta x} \right), & \text{if } v_i \geq 0; \\ v_i \left( \lambda \frac{f_{i+1} - f_{i-1}}{2\Delta x} + (1 - \lambda) \frac{-f_{i+2} - 3f_i + 4f_{i+1}}{2\Delta x} \right), & \text{if } v_i < 0. \end{cases} \quad (2.5)$$

Note that a uniform mesh grid is used here. It can be easily shown that when  $\lambda = 2/3$  the truncation error of the differencing scheme in (2.5) for convective terms is of the order of  $\Delta x^3$ . This differencing scheme has been used by *Shi et al.* [1988] to simulate the global reconnection pattern at the dayside magnetopause. It can be shown that the scheme in (2.5) introduces a fourth-order dissipation, which corresponds to a fourth-order superviscosity. This fourth-order dissipation can smooth the fine structures in the simulation.



3. For the diffusion term on the right hand side of (2.2), the usual second-order center-differencing scheme is used.

4. A fast Poisson solver is used to solve the Poisson equation (2.4) at each time step.

Some test cases of the simulation code show that the numerical scheme is stable even for a very small viscosity. The effect of numerical errors is significant only when the Reynolds number,  $R$ , is larger than  $\sim 2000$ , where  $R = aV_0/\nu$ . We set  $R = 1000$  in all four cases presented in the next section.

### 2.2.3 Boundary Conditions

In the study of this chapter, we focus on the duskside region of the LLBL as shown in Figure 1.2a. The simulation domain is schematically shown in Figure 2.1, where the left boundary ( $y = 0$ ) is the magnetopause, the right boundary ( $y = L_y$ ) is the inner boundary, the top boundary ( $x = 0$ ) is the boundary near the subsolar region, and the bottom boundary ( $x = L_x$ ) is the tailward boundary. We set  $L_x = 5R_E$  and  $L_y = 1R_E$ . The plasma number density in the magnetospheric side is  $N_2 = N_0$  and the density in the magnetosheath side is maintained at  $N_1 = \alpha N_0$ , where  $\alpha$  is specified for each case.

*Left boundary ( $y = 0$ ).* The magnetopause ( $y = 0$ ) plays a very important role in the present simulation. It is at the magnetopause that the solar wind momentum and mass are transported into the boundary layer region and, subsequently, into the magnetosphere. Observations show that, at the magnetopause, the plasma density and the tangential velocity are close to their magnetosheath level. The velocity component normal to the magnetopause is usually small compared to the tangential component [Eastman, 1979]. Note that the injection region of the solar wind plasma may not be uniformly distributed over the magnetopause. For

example, there may exist some regions with an enhanced injection caused by the impulsive penetration of the magnetosheath plasma [Lemaire, 1977; Lemaire and Roth, 1978; Heikkila, 1982], by flux transfer events [Russell and Elphic, 1979], or by regions with an enhanced diffusion. To simulate these phenomena, we assume that, at the injection region of the magnetopause, the plasma density ( $N$ ) and the tangential velocity ( $v_t$ ) are maintained at their magnetosheath values; the normal velocity ( $v_n$ ) is kept constant during the simulation (time-independent) but may be different at different locations. For the remaining portion, boundary conditions for the plasma density and the flow velocity are  $\frac{\partial N}{\partial y} = \frac{\partial v_x}{\partial y} = \frac{\partial v_y}{\partial y} = 0$ .

*Top ( $x = 0$ ) and right ( $y = L_y$ ) boundaries.* Along the top boundary ( $x = 0$ ) and the right boundary ( $y = L_y$ ) we set  $N = N_2$ ,  $\Omega = 0$ , and  $\psi = 0$ .

*Lower boundary ( $x = L_x$ ).* Along the lower boundary ( $x = L_x$ ) we set  $\frac{\partial N}{\partial x} = 0$ ,  $\frac{\partial \psi}{\partial x} = 0$ , and  $\frac{\partial \Omega}{\partial x} = 0$  to allow an outflow of the boundary layer plasma.

### 2.3 Simulation Results

In this section the simulation results from four cases with different boundary conditions at the magnetopause and near the subsolar region are presented. Case A uses driven boundary conditions in just a small region of the magnetopause, while in Case B the diffusion plasma flux is maintained along the whole magnetopause. For comparison, Cases C and D show the pure Kelvin-Helmholtz instability associated with a sheared plasma flow under periodic boundary conditions and outflow boundary conditions, respectively.

### 2.3.1 Case A: Local Injection at the Magnetopause

In Case A the driven boundary conditions are imposed only in a localized region of the magnetopause. The plasma density and the tangential velocity are maintained at their magnetosheath values in the injection region. The plasma density is maintained at  $N_1 = 10N_0$  and the tangential velocity is maintained at  $v_x = V_0$ . A uniform grid mesh is used which contains  $321 \times 65$  grid points.

In the injection region (or the driven region) at the magnetopause  $\{x_0 - h < x < x_0 + h\}$ , the normal velocity is taken to be  $v_y = v_{n0} \cos[\frac{\pi}{2h}(x - x_0)]$  for simplicity, where  $v_{n0}$  is the characteristic normal velocity and  $2h$  is the length of the injection region. Outside the injection region, we set  $\frac{\partial N}{\partial y} = \frac{\partial v_x}{\partial y} = \frac{\partial v_y}{\partial y} = 0$  as mentioned in section 2.2. The normal velocity reaches maximum at the center of the injection region and smoothly decreases to zero at the edges. For this case, we choose  $v_{n0} = 0.15V_0$ ,  $x_0 = \frac{5}{6}R_E$ , and  $h = \frac{5}{12}R_E$ .

To avoid large gradients in the plasma density and the flow velocity in the injection region ( $x_0 - h < x < x_0 + h$ ,  $y = 0$ ), we let the plasma density increase linearly from  $N_0$  to its magnetosheath value  $N_1$ , the tangential velocity increase linearly from 0 to  $V_0$ , and the characteristic normal velocity increase linearly from 0 to  $v_{n0}$  during a small initial time interval  $\delta t = 0.4t_0$ . The choice of  $\delta t$  does not significantly affect the simulation results as long as  $\delta t$  is small relative to the growth time of the KH instability but large enough to avoid large gradients.

Figures 2.2a and 2.2b show contour plots of the plasma density and vector plots of the flow velocity at different simulation times, respectively. Initially ( $t = 0$ ), the plasma density is uniform and the flow velocity is zero inside the simulation domain. From the plots of the plasma density and the flow velocity, it can be seen that maintaining normal

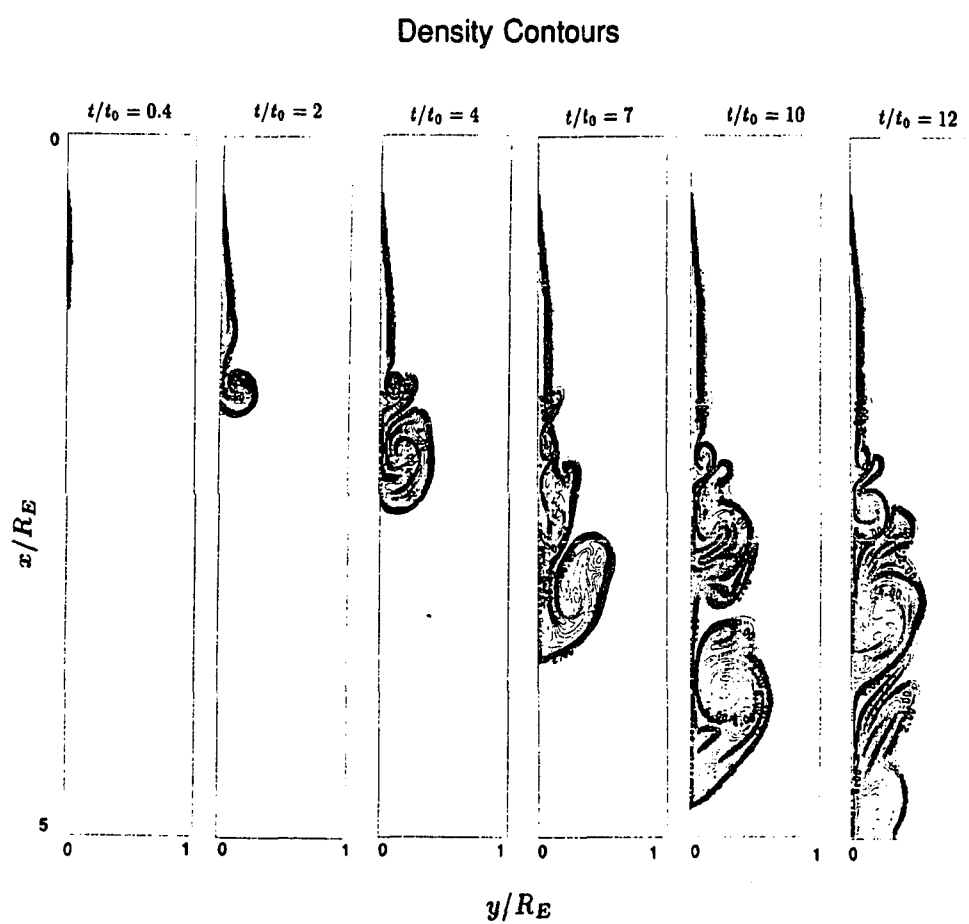


**Figure 2.2a** Contour plots of the plasma density at different simulation times in Case A.

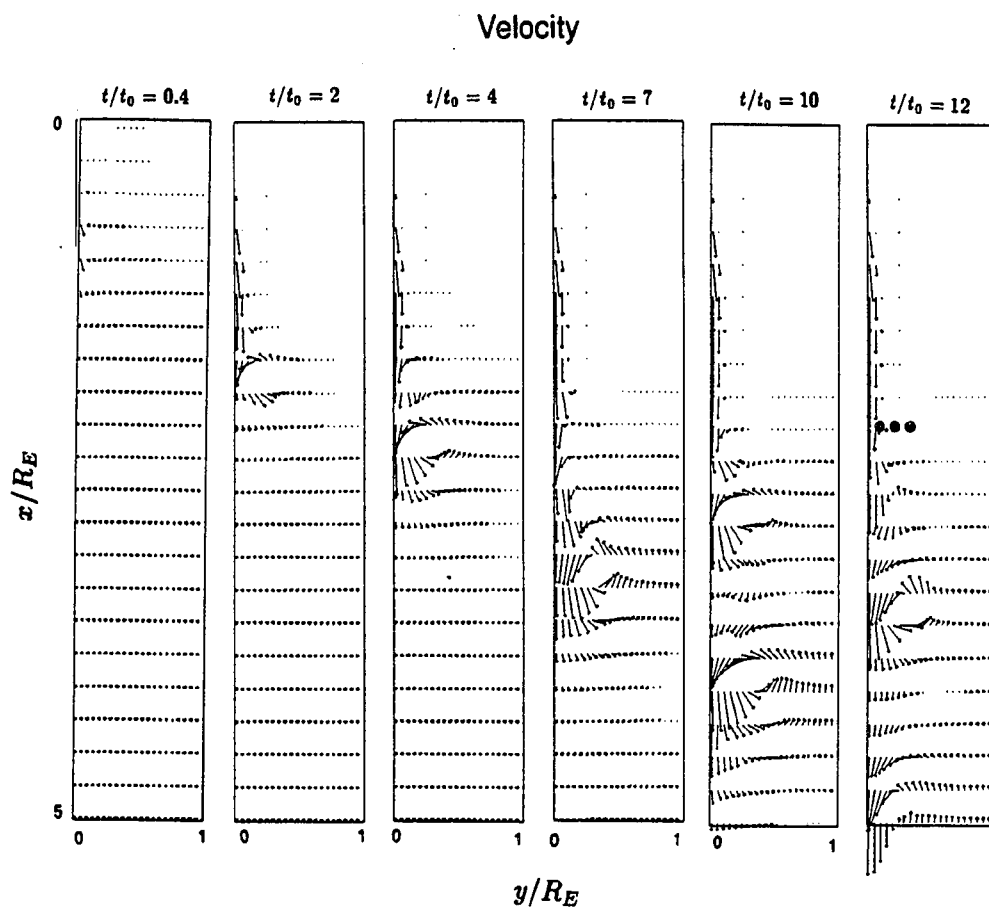


**Figure 2.2b** Vector plots of the flow velocity at different simulation times in Case A.

velocity in the injection region at the magnetopause leads to an inward convection of the magnetosheath plasma, while maintaining the tangential velocity at the magnetopause leads to a tailward plasma flow in the boundary layer. Figures 2.2a and 2.2b also show that the velocity shear in the boundary layer leads to the formation of localized plasma vortices through the development of the Kelvin-Helmholtz instability.

From contour plots of the plasma density in Figure 2.2a, it can be seen that the imposed diffusion flux in the injection region at the magnetopause does not simply lead to a smooth density profile. The density distribution has structures in the boundary layer region, with some local maximum and minimum values. As will be illustrated later, these density structures correspond to the observed vortex structures. The vortex structures are observed to grow in size as they are convected tailward. At the earlier stage, the boundary layer thickness increases with increasing longitudinal distance from the subsolar point. The thickness of the largest vortex at  $t = 7t_0$  reaches a value of  $\sim 0.5R_E$ . However, the maximum thickness of the vortices does not increase as they are convected further tailward (downstream) as shown in the last two panels ( $t/t_0 = 10, 12$ ) of Figures 2.2a and 2.2b. The maximum thickness  $D$  of vortices is related to the length of the injection region  $W$ , the average inward normal velocity  $\langle v_n \rangle$ , the plasma density in the injection region  $N_1$ , the average tailward flow speed  $\langle v_x \rangle$  in the boundary layer, and the average density  $\langle N \rangle$  in the boundary layer by the flux conservation relation,  $D \langle N \rangle \langle v_x \rangle = W N_1 \langle v_n \rangle$ . For Case A,  $W = 5R_E/6$ ,  $\langle v_n \rangle = 2v_{n0}/\pi \simeq 0.1V_0$ ,  $\langle v_x \rangle \simeq 0.3V_0$ , and  $\langle N \rangle \simeq 0.6N_1$ , we have  $D \simeq 0.5R_E$ .

From vector plots of the flow velocity in the boundary layer in Figure 2.2b, it can be observed that (1) vortex structures exist in the boundary layer, (2) the plasma flow in the boundary layer is mainly tailward although sunward flows are also present in some regions, and (3) the velocity vortex structures are coincident with the vortex density structures shown

in Figure 2.1a. In fact, the vortex density structures are formed by the vortex flow motion in the boundary layer.

The satellite velocity near magnetopause-boundary layer region is approximately 2 km/s [Eastman, 1979; Sckopke *et al.*, 1981], which is usually much smaller than the flow velocity ( $\sim 100 - 300$  km/s) in the boundary layer region. Therefore, the satellite can be considered stationary, observing the time variation of the plasma density and the flow velocity. Bearing this in mind, several probes are put in the simulation domain and the time variation of the plasma density and the flow velocity at these fixed positions can be observed. Figures 2.3a to 2.3c show the plasma density and the flow velocity measured by three probes which are located at (a)  $x = 2.25 R_E$ ,  $y = 0.0625 R_E$ ; (b)  $x = 2.25 R_E$ ,  $y = 0.125 R_E$ ; and (c)  $x = 2.25 R_E$ ,  $y = 0.1875 R_E$ , respectively. The positions of these three probes are indicated at  $t = 12t_0$  in Figure 2.2b. Highly variable structures in the plasma density and the flow velocity are clearly seen in these time series plots. The plasma density is more variable than the flow velocity. The flow velocity is generally correlated with the plasma density. It can be seen that the density profile in Figure 2.3a is more structured than that in Figure 2.3c. The probes at other positions in the boundary layer also show similar vortex structures, although the structures may be simple at some places and complex at other places.

To further study the spatial variations of the vortex structures, Figure 2.4 shows the one-dimensional profiles of the plasma density and the flow velocity at time  $t = 10t_0$  as a function of  $x$  along the lines  $y = 0.125 R_E$  (Figure 2.4a) and  $y = 0.40625 R_E$  (Figure 2.4b). The vortex structures can also be observed in most of the boundary layer region. There are also some correlations between the plasma density and the flow velocity in Figure 2.4a.

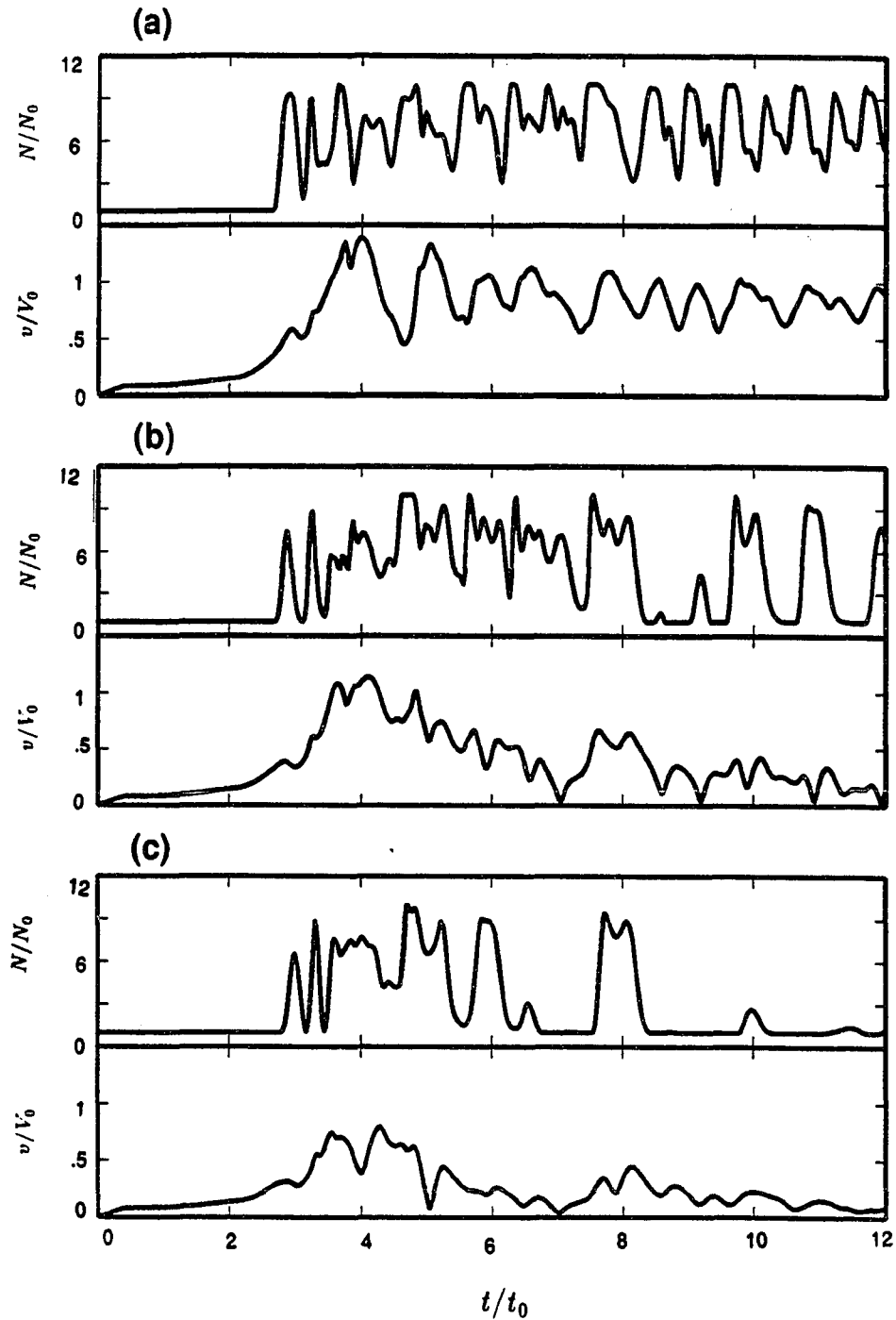


**Figure 2.3** The plasma density and the flow velocity as a function of time measured at three fixed probes in Case A which are located at (a)  $x = 2.25 R_E$ ,  $y = 0.0625 R_E$ ; (b)  $x = 2.25 R_E$ ,  $y = 0.125 R_E$ ; and (c)  $x = 2.25 R_E$ ,  $y = 0.1875 R_E$ .



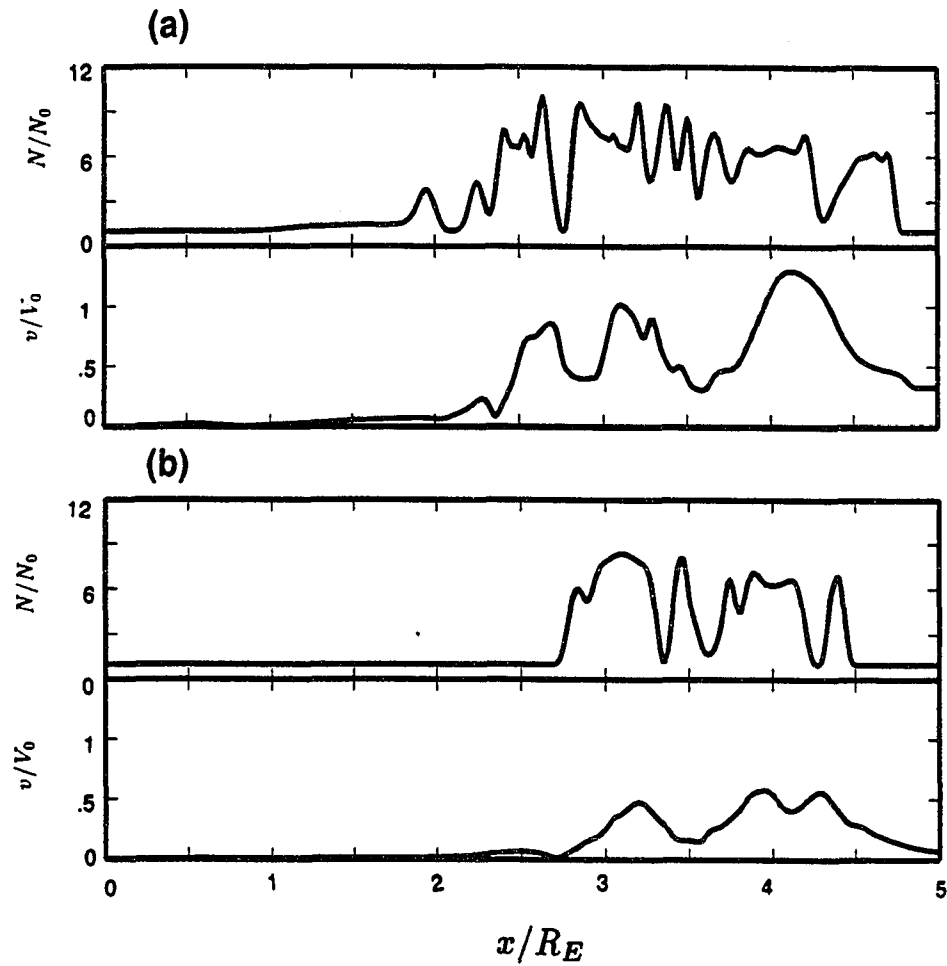


**Figure 2.4** Profiles of the plasma density and the flow velocity in the boundary layer parallel to the magnetopause in Case A at (a)  $y = 0.125 R_E$  and (b)  $y = 0.40625 R_E$ , at  $t = 10t_0$ .

Figure 2.5 shows the one-dimensional profiles of the plasma density and the flow velocity across the boundary layer at  $x = 3.91 R_E$  (Figure 2.5a) and  $x = 2.84 R_E$  (Figure 2.5b). It is interesting to note that the density profile in Figure 2.5a shows the presence of a plateau with a plasma density about 65% of the magnetosheath level. The flow speed near the magnetopause is close to its magnetosheath value in Figure 2.5a. The plasma density profile in Figure 2.5b shows some vortex structures, with a poor correlation with the flow velocity. It can be seen that from the velocity distribution in Figure 2.5 there are enhanced flow regions inside the boundary layer.

### 2.3.2 Case B: Uniform Injection at the Magnetopause

In Case B, the simulation results with a uniform diffusion flux along the whole magnetopause are presented. Along this boundary the plasma density and the tangential velocity are maintained at their magnetosheath values. The plasma density is maintained at  $N_1 = 10N_0$  and the velocity tangential to the magnetopause is set to  $v_x = V_0$ . A uniform grid mesh is used which contains  $321 \times 65$  grid points, which is the same as in Case A. In solving Poisson equation  $\nabla^2 \psi = -\Omega$ , the boundary condition used is  $\psi = 0$  at the upper boundary ( $x = 0$ ). This means that the tangential velocity,  $v_x$ , must be zero at the corner point  $(x, y) = (0, 0)$ . To resolve this problem, we allow the tangential velocity to increase from zero at  $x = 0$  to the value  $v_x = V_0$  in a short distance along the  $x$ -axis. This distance is taken to be  $0.25 R_E$ . The normal velocity is maintained at a constant value  $v_y = v_{n0}$  along the whole magnetopause. We choose  $v_{n0} = 0.05V_0$  in Case B, which corresponds to 10 km/s for  $V_0 = 200$  km/s. As in Case A, the values imposed at the inflow boundary ( $y = 0$ ) increase from the magnetospheric values to the magnetosheath ones in a time interval  $\delta t = 0.4t_0$ .

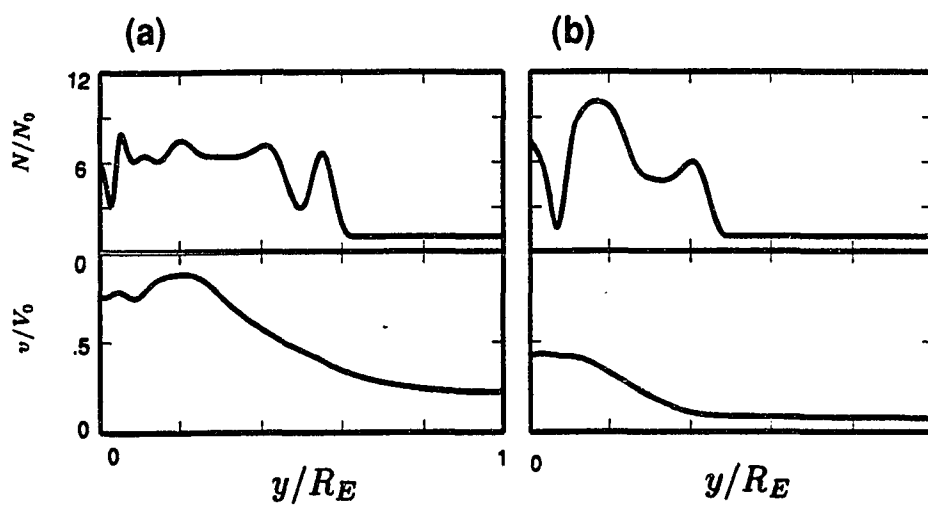


**Figure 2.5** Profiles of the plasma density and the flow velocity across the boundary layer in Case A at (a)  $x = 3.91 R_E$  and (b)  $x = 2.84 R_E$ , at  $t = 10t_0$ .

Figures 2.6a and 2.6b show contour plots of the plasma density and vector plots of the flow velocity at different simulation times, respectively. The vortex structures are formed initially near the central part ( $x \sim 2.5 R_E$ ) along the  $x$ -direction, as shown in Figure 2.6a at time  $t = 4t_0$ . These structures are then convected tailward. In the meantime, the vortex structures move further inward into the magnetosphere. Unlike Case A, in which the transport of magnetosheath plasma is limited to a finite region near the magnetopause, the thickness of the vortex structures in Case B keeps increasing during the tailward convection of the vortices due to the maintained driven condition along the whole magnetopause.

The coalescence of vortices is observed in both Cases A and B. As shown in Figure 2.6a, at  $t = 4t_0$ , "A", "B", "C", "D", "E", "F", and "G" denote seven different vortex structures in the simulation domain. At  $t = 6t_0$ , these vortex structures have grown to large sizes and are convected tailward. The vortex structure "A" has been convected further tailward and out of the simulation domain. The vortex structures "C" and "D" coalesce and form a large vortex. Similarly, the vortex structures "F" and "G" also coalesce and form a large one. In the meantime, more vortex structures are formed. At  $t = 8t_0$ , the vortex structures "F/G" and "H" coalesce. As time goes on, more vortices are formed and more coalescing takes place. At  $t = 12t_0$ , the vortex structure "FGHI" is more than  $1.5 R_E$  in length and  $\sim 0.9 R_E$  in width.

Vector plots of the flow velocity for Case B, shown in Figure 2.6b, show that in Case B there are more large vortex motions and the motions are more complex than those in Case A. The vortex structures in Case B also penetrate deeper into the magnetosphere than those in Case A.

Figure 2.7 shows the one-dimensional profiles of the plasma density and the flow velocity at time  $t = 10t_0$  along the lines  $y = 0.125 R_E$  (Figure 2.7a) and  $y = 0.3125 R_E$  (Figure

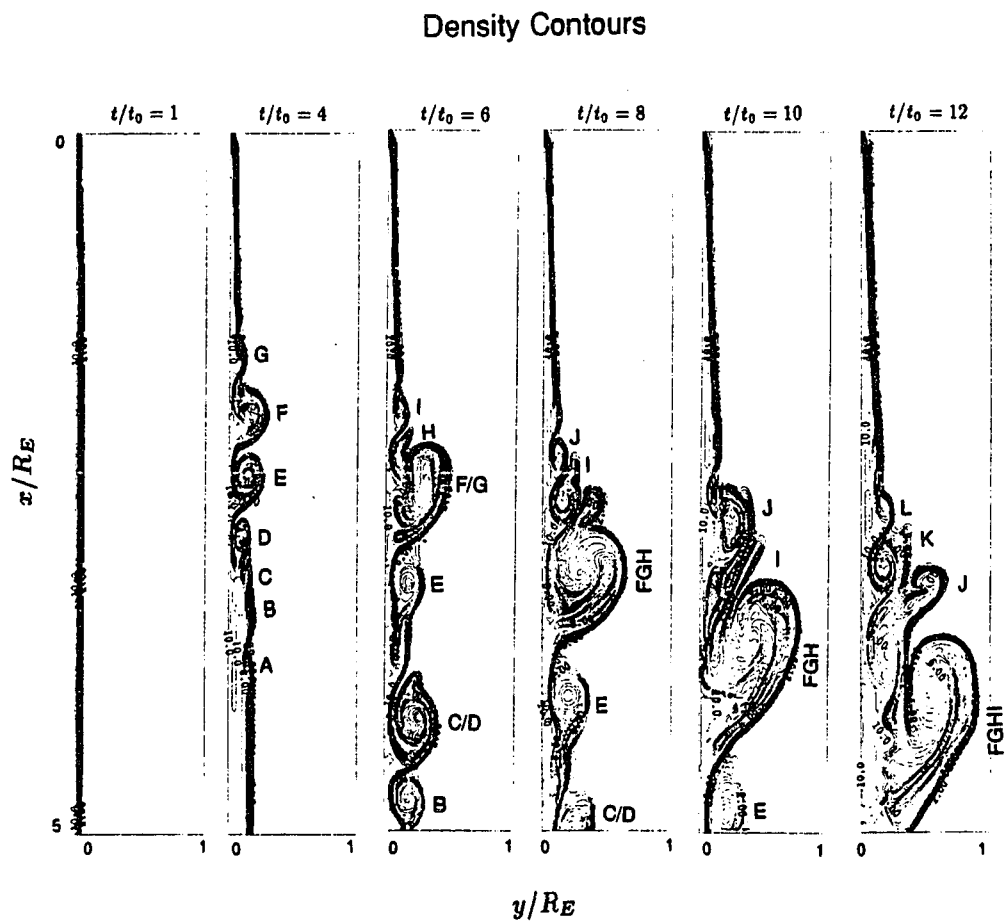


**Figure 2.6a** Contour plots of the plasma density at different simulation times in Case B.

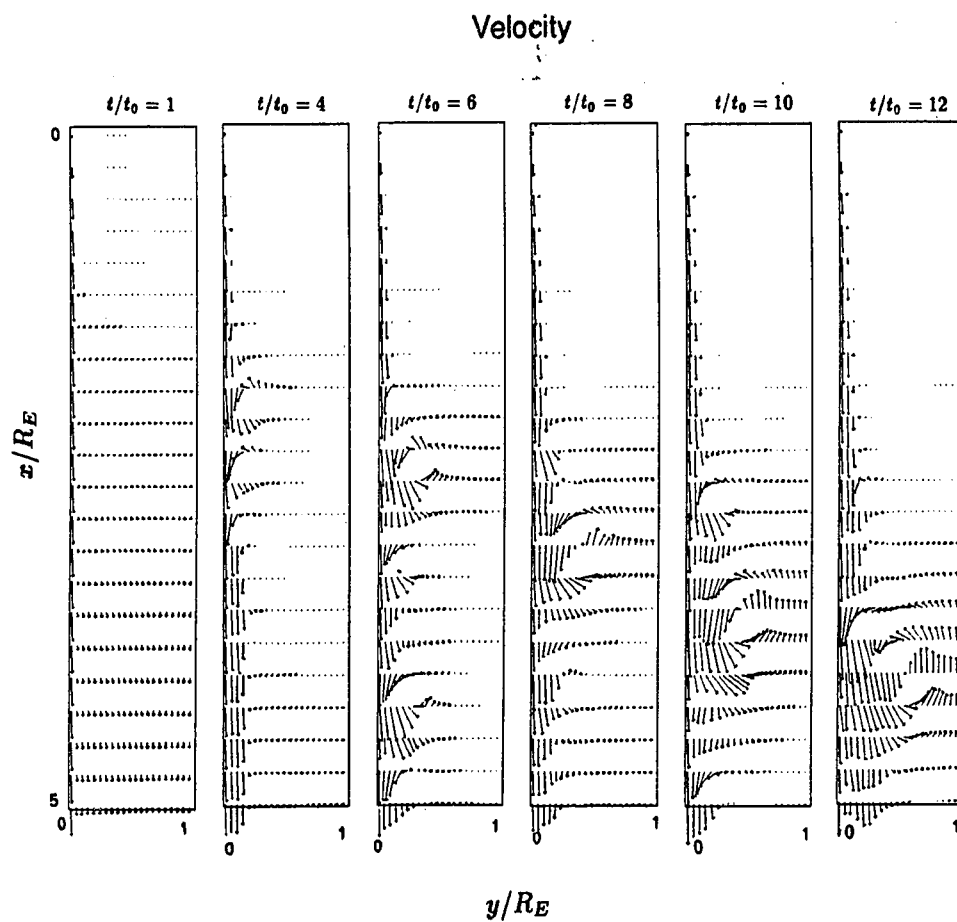


**Figure 2.6b** Vector plots of the flow velocity at different simulation times in Case B.

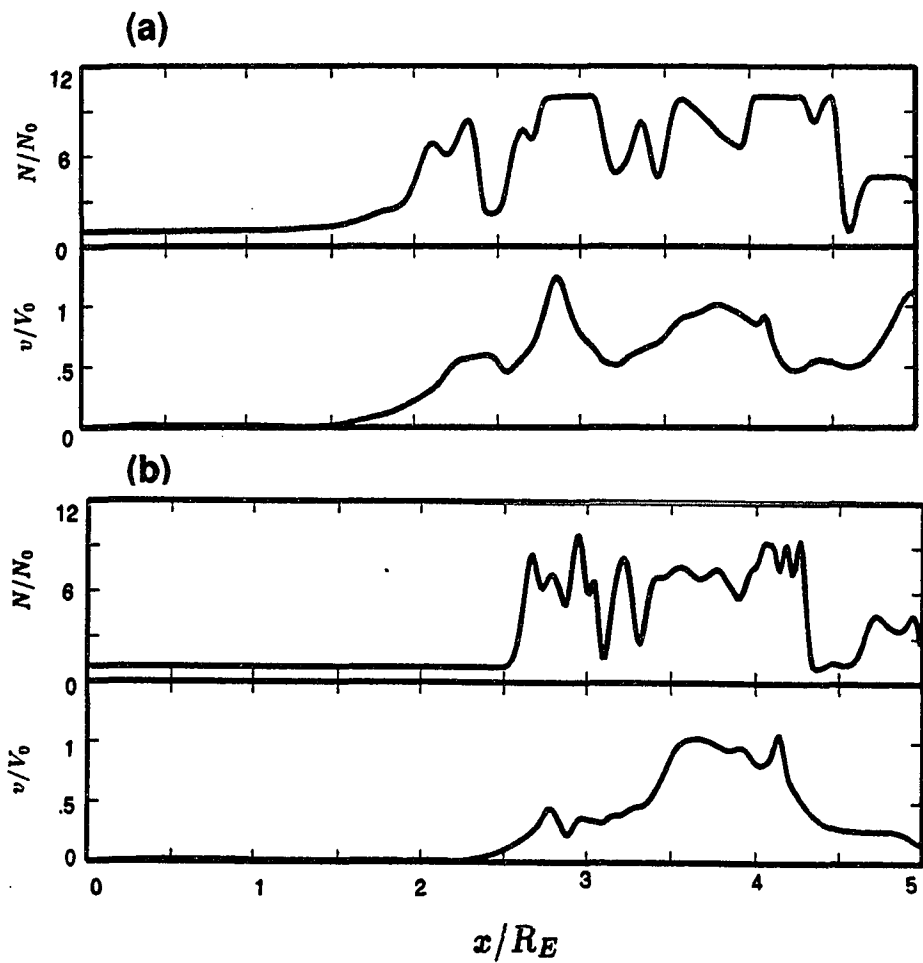


**Figure 2.7** Profiles of the plasma density and the flow velocity in the boundary layer parallel to the magnetopause in Case B at (a)  $y = 0.125 R_E$  and (b)  $y = 0.3125 R_E$ , at  $t = 10t_0$ .

2.7b) for Case B. These profiles also show vortex structures in the boundary layer. The result is similar to Case A, as shown in Figure 2.4. There exist some correlations between the plasma density and the flow velocity in Figure 2.7. The time profiles of the plasma density and the flow velocity observed at fixed positions in the simulation domain also give similar results as in Case A.

### 2.3.3 Case C: A Sheared Plasma Flow with Periodic Boundary Conditions

In Cases A and B, the simulation results with driven boundary conditions at the magnetopause are shown, either through a localized region of the magnetopause as shown in Case A or along the whole magnetopause as shown in Case B. The vortex structures are observed in the boundary layer. For comparison, the simulation results for the pure Kelvin-Helmholtz instability with periodic boundary conditions are shown here, in which periodic boundary conditions are imposed along the  $x$ -direction and the boundaries at  $y = 0$  and  $y = L_y$  are far away from the central shear region. The initial profiles of the plasma density and the flow velocity are given as

$$N = \frac{1}{2}(N_1 + N_2) - \frac{1}{2}(N_1 - N_2) \tanh\left(\frac{y - 0.5L_y}{a_v}\right) \quad (2.6)$$

$$v_x = \frac{1}{2}V_0 \left[1 - \tanh\left(\frac{y - 0.5L_y}{a_v}\right)\right] \quad (2.7)$$

where  $N_2 = N_0$  is the plasma density in the magnetosphere,  $N_1 = 10N_0$  is the plasma density in the magnetosheath,  $V_0$  is the tailward velocity at the magnetopause ( $y = 0$ ),  $L_y$  is the length of the simulation domain in the  $y$ -direction, and  $a_v$  is the half-thickness of the transition layer for both the plasma density and the flow velocity. The velocity in the magnetospheric side is zero. A uniform grid mesh is used which contains  $64 \times 64$  grid points.



The simulation domain is in the  $x$ - $y$  plane with  $L_y = L_x = 1R_E$ . Periodic boundary conditions are used along the  $x$ -direction. The boundary conditions along  $y = 0$  (left boundary) and  $y = L_y$  (right boundary) are  $\frac{\partial N}{\partial y} = \frac{\partial v_x}{\partial y} = \frac{\partial v_y}{\partial y} = 0$ .

From the flow velocity in (2.6), the initial vorticity profile can be obtained as

$$\Omega = 0.5(V_0/a_v) \operatorname{sech}^2 \left( \frac{y - 0.5L_y}{a_v} \right) \quad (2.8)$$

A small perturbation in vorticity is introduced explicitly at the beginning of the simulation, which has the following form

$$\delta\Omega = \delta_p \sin \left( \frac{2\pi x}{L_x} \right) \exp \left[ -\frac{(y - 0.5L_y)^2}{a_p^2} \right] \quad (2.9)$$

The perturbed wavelength is the total length in the  $x$ -direction ( $L_x$ ). We set  $a_v = 0.04 R_E$ ,  $\delta_p = 0.01V_0/a_v$  and  $a_p = 0.04 R_E$  in Case C. The simulation results are not sensitive to a small change of  $a_p$  and  $\delta_p$ . The maximum linear growth rate of the KH instability in Case C can be estimated as  $\gamma \approx 0.1V_0/a_v \approx 2t_0^{-1}$  [e.g., *Lee et al.*, 1981; *Miura and Pritchett*, 1982].

Figure 2.8 shows contour plots of the plasma density (top panel) and vector plots of the flow velocity (bottom panel) at different simulation times. Although the simulation in Case C is carried out in one wavelength along the  $x$ -direction, two wavelengths along the  $x$ -direction are plotted in Figure 2.8 for clarity of presentation. Due to the presence of the velocity shear, the KH instability develops, creating vortex-like motion in the simulation domain. The vortex-like motion twists the plasma density distribution. As a consequence, the vortex structures are formed. Since the perturbation wavelength is the total length of the simulation domain along the  $x$ -direction, only one vortex is formed within the simulation length ( $1R_E$ ). Note that in Case C coalescence of vortices cannot occur due to the imposed periodic boundary condition and the initial conditions. As the KH instability develops, the

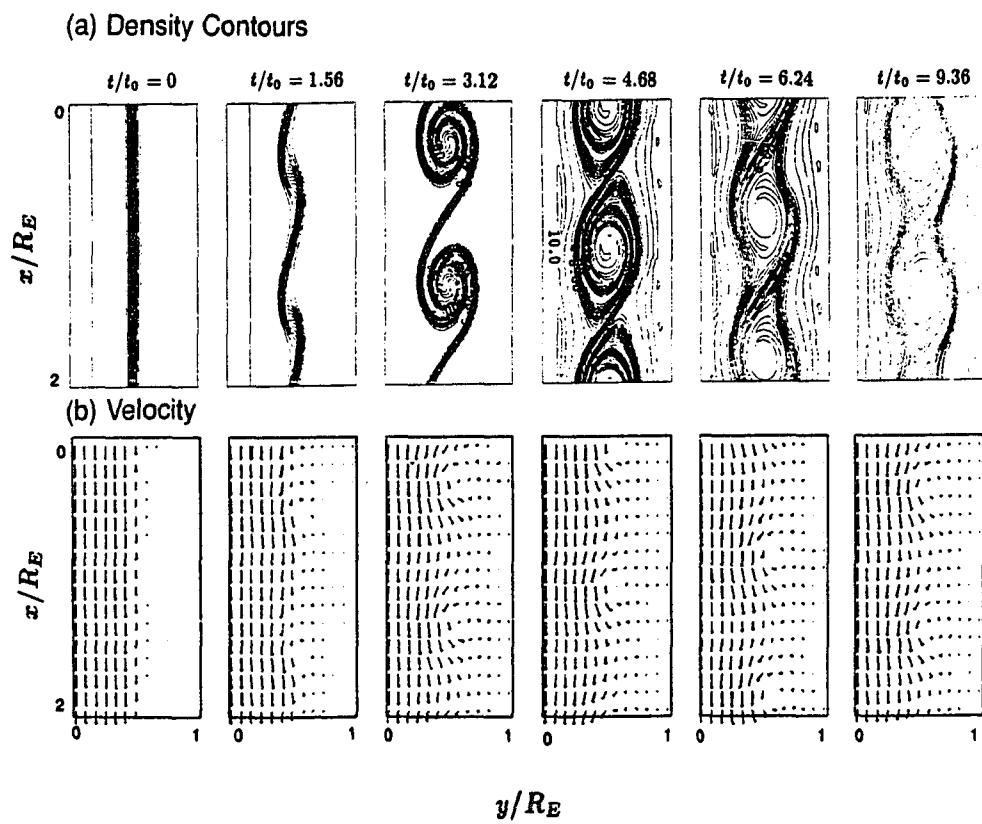


**Figure 2.8** (a) Contour plots of the plasma density and (b) vector plots of the flow velocity at different simulation times in Case C.

width of the vortex grows, as can be seen from the velocity plots in Figure 2.8. In the meantime, the plasma originating from the magnetosheath mixes with the plasma originating from the magnetosphere, as shown in the contour plots of the plasma density in Figure 2.8. As time goes on, the mixing of the magnetosheath and the magnetospheric plasmas is further enhanced. Finally, a region with a density plateau (a constant density region with the density value between those in the magnetosheath and in the magnetosphere) is formed near the central part of the boundary layer region. The one-dimensional plots of the plasma density in Figure 2.9 in the following clearly show these features. The density plateau can also be seen in Figure 2.5a of Case A.

Figures 2.9a through 2.9f show the one-dimensional profiles of the plasma density across the center of the vortex at different simulation times with  $t = 0$ ,  $t = 1.56t_0$ ,  $t = 3.12t_0$ ,  $t = 4.68t_0$ ,  $t = 6.24t_0$ , and  $t = 9.36t_0$ . Note that the  $x$ -coordinate of the vortex center varies with time. Figure 2.9a shows the initial density profile. The transition region of the plasma density is at the central part of the boundary layer. At  $t = 1.56t_0$  (Figure 2.9b) there are small variations in the plasma density near the central plane ( $y = 0.5 R_E$ ). At  $t = 3.12t_0$  (Figure 2.9c) highly variable density structures are formed. The thickness of the plasma mixing region is  $\sim 0.5 R_E$ . In the mixing region there is one place ( $y \sim 0.32 R_E$ ) where the plasma density reaches the magnetospheric value and another place ( $y \sim 0.56 R_E$ ) where the plasma density reaches the magnetosheath value. As the simulation progresses, the plasma density in the mixing region becomes more and more smoothly distributed. Finally, at  $t = 9.36t_0$  (Figure 2.9f), a plasma density plateau with a width of  $\sim 0.5 R_E$  is formed around the central part of the boundary layer.

Note that the plasma density plateau is formed as a combined effect of mixing and diffusion. The mixing is caused by the development of the KH instability. If there is no

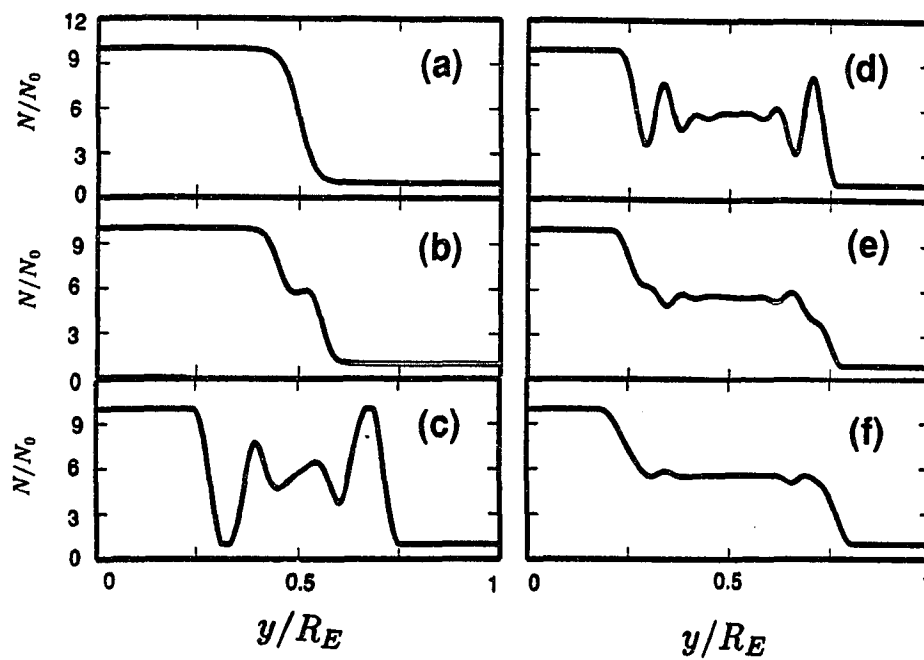


**Figure 2.9** Profiles of the plasma density across the center of the vortex in Case C at different simulation times with (a)  $t = 0$ , (b)  $t = 1.56t_0$ , (c)  $t = 3.12t_0$ , (d)  $t = 4.68t_0$ , (e)  $t = 6.24t_0$ , and (f)  $t = 9.36t_0$ .

mixing, the diffusion process is very slow and a density profile of the plateau shape cannot be formed by diffusion. If there is no diffusion, the fine-grained density distribution due to mixing can have only one of two values,  $N_1$  or  $N_2$ , and no smooth plateau can be formed. Mixing increases the length of the boundary between the two plasma regions with density values,  $N_1$  and  $N_2$ , while the diffusion process along the elongated boundary leads to a smooth transition between the two neighboring mixing regions.

Figure 2.10 shows the one-dimensional profiles of the plasma density and the flow velocity at time  $t = 3.12t_0$  as a function of  $x$  at  $y = 0.5 R_E$  (Figure 2.10a) and  $y = 0.375 R_E$  (Figure 2.10b). Similar to Figure 2.8, two wavelengths along the  $x$ -direction are plotted here. The vortex structures are apparent in the density plots, while the variations of the flow velocity are smaller than those in Cases A or B.

#### 2.3.4 Case D: A Sheared Plasma Flow with Outflow Boundary Conditions

In Case D, the simulation results for the pure Kelvin-Helmholtz instability associated with a sheared plasma flow with outflow boundary conditions are presented. The initial profiles of the plasma density and the flow velocity are the same as those given by (2.6) and (2.7) in Case C. The simulation domain is in the  $x$ - $y$  plane with  $0 \leq x \leq L_x = 5R_E$  and  $0 \leq y \leq L_y = 2R_E$ . The center of the transition region for both the plasma density and the flow velocity is located at  $y = 1R_E$  in Case D, in contrast to  $y = 0.5R_E$  in Case C. Other parameters are the same as those in Case C. The boundary conditions at  $x = 0$  (upper boundary) and  $x = 5R_E$  (lower boundary) are  $\frac{\partial N}{\partial x} = \frac{\partial v_x}{\partial x} = \frac{\partial v_y}{\partial x} = 0$  and the boundary conditions at  $y = 0$  (left boundary) and  $y = 2R_E$  (right boundary) are  $\frac{\partial N}{\partial y} = \frac{\partial v_x}{\partial y} = \frac{\partial v_y}{\partial y} = 0$ .

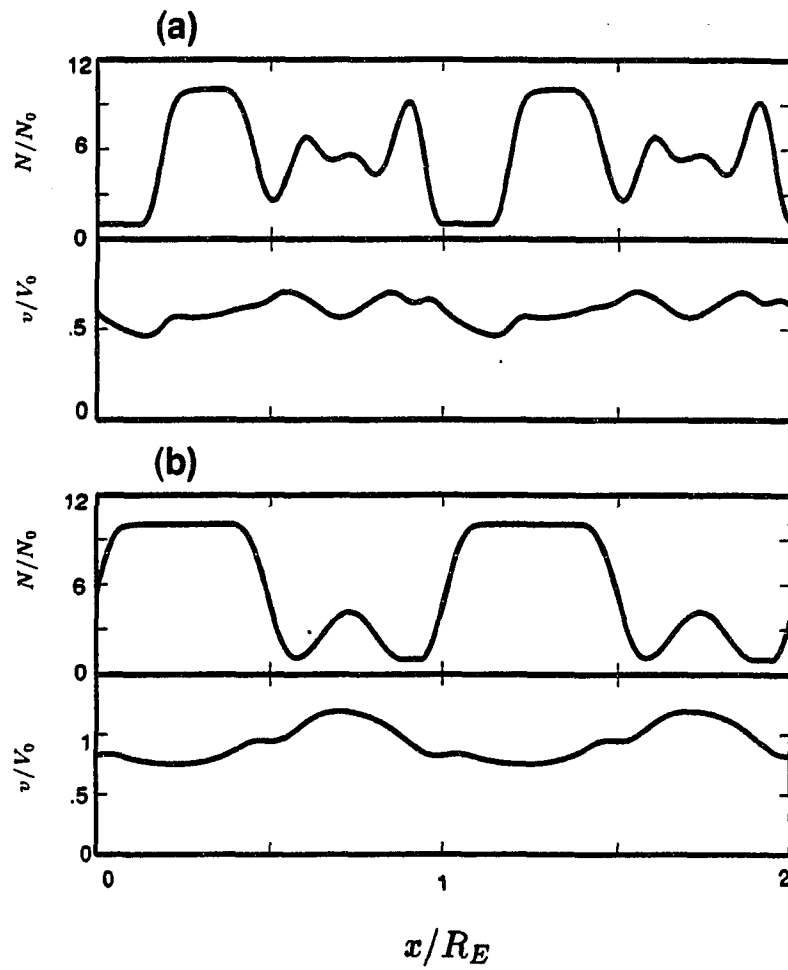


**Figure 2.10** Profiles of the plasma density and the flow velocity in the boundary layer parallel to the magnetopause in Case C at (a)  $y = 0.5 R_E$  and (b)  $y = 0.375 R_E$ , at  $t = 3.12t_0$ .

A random perturbation in vorticity is introduced explicitly at the beginning of the simulation.

A uniform grid mesh is used which contains  $321 \times 129$  grid points.

Figure 2.11 shows contour plots of the plasma density (top panel) and vector plots of the flow velocity (bottom panel) at different simulation times in Case D. Plasma vortices are formed as a consequence of the development of the KH instability. Magnetosheath and magnetospheric plasmas mix near the central shear region. Coalescence of the plasma vortices can be observed (see plots at  $t = 3.6t_0$  and  $t = 5.2t_0$ ), which leads to the growth of the vortex structure in size and an increase of the thickness of the boundary layer. As the plasma vortex convects further tailward, it grows to large size, which leads to more increase of the boundary layer thickness, as can be seen from the plots at  $t = 7.8t_0$ . The simulation results shown here are very similar to those in Case B with a uniformly driven condition along the magnetopause.

One noteworthy difference between Cases D and B is the plasma convection toward the left boundary in Case D. It can be seen from Figure 2.11 that in Case D the boundary layer plasma is convected toward the magnetosheath. However, we assume that the magnetopause is a fixed boundary in Case B and no plasma is allowed to flow from the boundary layer toward the magnetopause. If the IMF has only a  $B_z$  component, the magnetosheath magnetic field will be parallel or antiparallel to the magnetospheric magnetic field and the assumption of a fixed magnetopause becomes invalid. However, the magnetic fields in the magnetosheath and in the magnetosphere are generally not parallel or antiparallel. It has been shown that, if the rotation angle between the IMF and the magnetospheric magnetic field is larger than  $10^\circ$ , the tension force due to the no-parallel magnetic fields tends to stabilize the development of the KH instability at the magnetopause [Lee *et al.*, 1981]. This tension force at the magnetopause prohibits the outward motion of the boundary layer plasma.

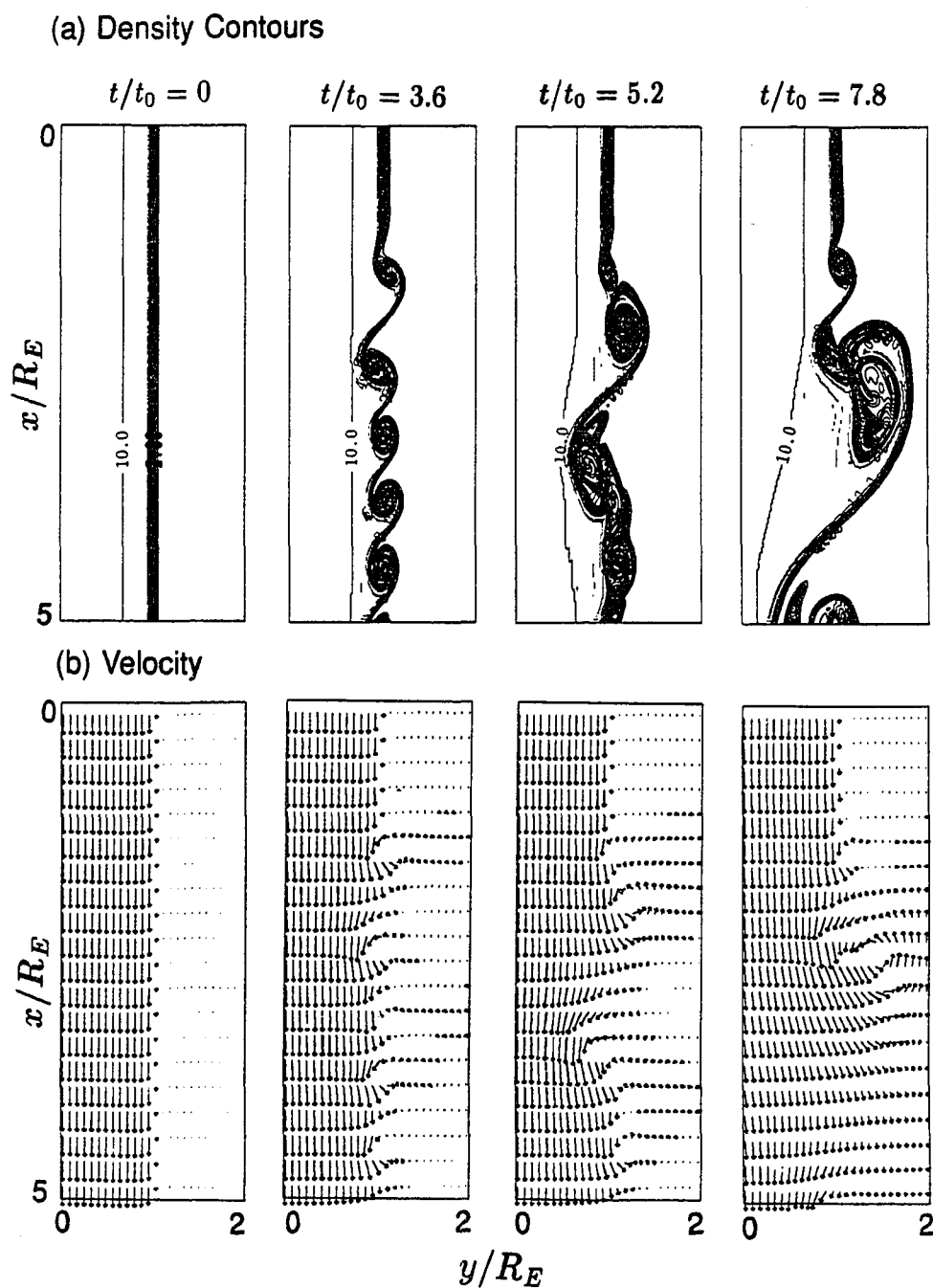


**Figure 2.11** (a) Contour plots of the plasma density and (b) vector plots of the flow velocity at different simulation times in Case D.



## 2.4 Discussion and Summary

This chapter presents studies of the plasma dynamics in the low-latitude boundary layer under different driven conditions at the magnetopause by two-dimensional MHD numerical simulations. In the simulation, plasma is driven into the boundary layer region by imposing a diffusion flux along the magnetopause. The Kelvin-Helmholtz instability leads to the formation of vortex structures in the low-latitude boundary layer. The vortex structures in the plasma density and the flow velocity may coalesce as they are convected tailward, causing them to grow in size. The boundary layer thickness increases with increasing longitudinal distance from the subsolar point in accord with satellite observations. The plasma density and the flow velocity tend to be positively correlated, as shown in Figure 2.3. A mixed region is formed where the magnetosheath plasma and the magnetospheric plasma mix due to the vortex motions. In the later stage of development, a density plateau is formed in the central part of the boundary layer. Many features of the satellite observations of the boundary layer can be explained by this numerical model.

In this chapter the numerical simulations use four different boundary conditions at the magnetopause-boundary layer region. In the presence of an anomalous transport due to plasma waves at the magnetopause, the boundary conditions used in Cases A and B are likely to occur at the magnetopause. The boundary condition in Case B is more favorable because the plasma waves are observed during most of the magnetopause crossings. The boundary condition in Case A corresponds only to occasions with the presence of an impulsive penetration or a localized injection of the magnetosheath plasma into the boundary layer through the magnetopause. On the other hand, Cases C and D are idealized cases which are used to study the isolated evolution of the KH instability.

A constant magnetic field perpendicular to the simulation plane is used in the simulation model. The magnetic pressure gradient associated with a variable magnetic field may affect the plasma dynamics in regions where the localized current produces large deformation of the magnetic field. In addition, the presence of the magnetic field components in the simulation plane is expected to slow down the development of the KH instability.

The numerical simulations presented in this chapter are based on an incompressible MHD numerical model. The effect of compressibility has been neglected. It is expected that the presence of plasma compressibility may lead to a better correlation between the plasma density and the flow velocity.

In this chapter, the magnetosphere-ionosphere coupling processes have also been neglected. The presence of the finite ionospheric conductivity will exert a dragging force on the plasma flow in the magnetosphere and slow down the magnetospheric convection [Sonnerup, 1980; Kan and Lee, 1980; Lotko *et al.*, 1987]. The simulations including the magnetosphere-ionosphere coupling effect will be the subject of the next chapter. It is noted that the vortex structures formed in the low-latitude boundary layer may lead to the formation of patchy auroras in the dayside polar cap region [Lanzerotti *et al.*, 1986; Sandholt *et al.*, 1986; Lui *et al.*, 1989; Potemra *et al.*, 1990]. The simulation model presented here predicts that the vortices generated in the duskside (dawnside) boundary layer lead to the presence of localized upward (downward) field-aligned currents in both the northern and the southern polar ionospheres.

The principal results obtained by the simulations in this chapter may be summarized as follows.

1. In the boundary layer region, the vortex motions associated with the Kelvin-Helmholtz instability are observed in the simulation. The plasma flows are mainly tailward but sunward flows are also observed.

2. The plasma density profiles in the boundary layer have vortex structures. The plasma density has some local maximum values, which approach the magnetosheath level, and some local minimum values, which approach the magnetospheric level.

3. The vortex structures may coalesce as they are convected tailward by a variable tailward convection velocity, as illustrated in Cases A, B, and D. Coalescence will cause the vortex structures to grow in size.

4. The thickness of the boundary layer increases with increasing longitudinal distance from the subsolar point. For Case A with a finite influx window, the maximum thickness of the boundary layer reaches a steady value. On the other hand, the maximum thickness in Cases B and D keeps increasing during the tailward convection of the vortex structures.

5. The plasma density and the flow velocity are highly variable. The flow velocity is generally correlated with the plasma density.

6. The plasma originating from the magnetosheath mixes with the plasma originating from the magnetosphere, forming a mixing region in the boundary layer. The mixing is due to the vortex motion associated with the KH instability. Due to the combined effect of mixing and diffusion, a region separated from both the magnetosheath and the magnetosphere is formed near the central part of the boundary layer in the later stage. In this region the plasma density is nearly constant and a plateau in the plasma density is formed.

7. The vortices generated in the duskside (dawnside) boundary layer lead to the presence of localized upward (downward) field-aligned currents in both the northern and the southern polar ionospheres. The upward field-aligned current filaments associated with the vortices

in the duskside region of the boundary layer may account for the observed dayside auroras which show bright features resembling “beads” or “pearls” [*Lui et al.*, 1989; *Potemra et al.*, 1990], which will be studied in the next chapter.

## CHAPTER 3

### Auroral Bright Spots

#### 3.1 Introduction

From the observations presented in Chapter 1, it can be seen that the formation of the post-noon auroral bright spots in the polar ionosphere may be associated with the Kelvin-Helmholtz instability in the low-latitude boundary layer in the magnetosphere. However, the presence of the finite ionospheric conductivity can damp the plasma motion in the boundary layer, as mentioned. The dynamics in the LLBL and in the polar ionosphere can be studied self-consistently by using a magnetosphere-ionosphere coupling model. A number of magnetosphere-ionosphere coupling models have been developed to study the interaction between the magnetosphere and the ionosphere and the formation of auroral arcs. *Sato* [1978] proposed that the coupled magnetosphere-ionosphere system is subject to a feedback instability, which may be used to explain the formation of auroral arcs. The above feedback theory was supported by numerical simulations [*Miura and Sato*, 1980]. The feedback instability has been further studied by *Lysak* [1991], who found that the nonuniform density in the topside ionosphere can lead to the formation of a resonant cavity and the existence of this cavity leads to a modification of the Alfvén wave reflection coefficient in the ionosphere. *Goertz and Boswell* [1979] found that a localized electromotive force applied across the geomagnetic field may propagate along the geomagnetic field with the Alfvén velocity. The field-aligned currents are treated as a manifestation of propagating Alfvén waves. A similar approach to

understand the electrodynamic structure of auroras has been used by *Lysak and Dum* [1983] and *Lysak* [1985].

An electrostatic, kinetic description of the auroral flux tube [*Knight*, 1973; *Chiu and Cornwall*, 1980; *Lyons*, 1980; *Chiu et al.*, 1981] gives an explanation for the current-voltage relationship along the geomagnetic field lines and the scale size of the current structures. A linear current-voltage relationship is valid for most of the plasma density and energy ranges and for both large-scale auroral formations and small-scale discrete auroral arcs, but may have a different proportionality for upward and downward FACs [*Knight*, 1973; *Chiu and Cornwall*, 1980; *Chiu et al.*, 1981; *Lyons*, 1981; *Weimer et al.*, 1987]. *Kan and Lee* [1980] presented a time-dependent imperfect magnetosphere-ionosphere coupling model with the presence of field-aligned potential drops. They found that the equipotential contours are distorted into a V-shaped structure near the convection reversal boundary and an S-shaped structure on the equatorward side to produce inverted V precipitation bands. *Seyler* [1988, 1990] developed a model for the structure and evolution of small-scale discrete auroral arcs based on the magnetosphere-ionosphere coupling processes and found that the collisionless tearing instability may be the origin of small-scale discrete auroral arcs.

*Sonnerup* [1980] developed a one-dimensional steady-state fluid model for the low-latitude boundary layer based on the magnetosphere-ionosphere coupling via FACs. It is found that the potential profile corresponds reasonably well to observed inverted V events. The corresponding two-dimensional model for the nonsteady boundary layer flow dynamics including the ionospheric drag and a parallel electric field was also developed [*Lotko et al.*, 1987]. The sheared plasma flow couples to the polar ionosphere and may be responsible for the formation of V shocks in and above the auroral acceleration region. The noteworthy difference between *Lotko et al.*'s [1987] model and other models is that the magnetospheric

convection pattern can evolve self-consistently through interaction with the ionosphere. Non-linear evolution of the KH instability in the polar ionosphere due to the sheared plasma flow in the magnetosphere including the finite Pedersen conductivity has also been studied [Keskinen *et al.*, 1988]. It is found that the ionospheric conductivity has a damping effect on the development of the KH instability.

In this chapter a more comprehensive time-dependent magnetosphere-ionosphere coupling model is developed. It describes the plasma dynamics self-consistently both in the low-latitude boundary layer and in the polar ionosphere. In the present model, the interaction of the solar wind and the magnetosphere is included, which is characterized as plasma transport across the magnetopause. A non-periodic boundary condition is used at the magnetopause, which differs significantly from the previous models [e.g., Lotko *et al.*, 1987; Keskinen *et al.*, 1988]. Both the Pedersen and the Hall conductivities are considered in the ionosphere and the conductivities are allowed to be enhanced due to precipitation of energetic electrons in the upward field-aligned current regions. The electric field parallel to the geomagnetic field is allowed to exist, which accelerates electrons and gives rise to a potential drop between the magnetosphere and the ionosphere. A linear current-voltage relationship is used for both upward and downward FACs along the geomagnetic field lines, but with different proportionality constants. These features of the present model are described in detail in next section.

In Chapter 2, it is found that the Kelvin-Helmholtz instability, with a driven flow at the magnetopause, can lead to the observed vortex flow and density structures in the boundary layer as suggested by Skopke *et al.* [1981] and Lee *et al.* [1981]. The results predict that the vortices generated in the duskside (dawnside) region of the boundary layer lead to the presence of localized upward (downward) FACs in both the northern and the southern polar

ionospheres. As a continuation, this chapter presents a magnetosphere-ionosphere coupling model to study the plasma dynamics in the magnetopause-boundary layer region and its coupling to the polar ionosphere. We attempt to relate the observed spatially periodic auroral bright spots in the post-noon sector of auroral oval to the vortex structures observed in the boundary layer.

It may be mentioned that *Rostoker and Eastman* [1987] suggested that the KH instability due to the velocity shear near the central plasma sheet and the magnetospheric boundary layer may also lead to the formation of auroral bright spots in the evening sector.

In section 3.2, we describe both the simulation model and governing equations. The simulation results of coupling of the magnetopause-boundary layer to the post-noon and pre-noon ionosphere are presented in section 3.3. Section 3.4 contains the summary and discussions of our simulation results and their comparisons with observations in the low-latitude boundary layer and the observed auroral bright spots in the post-noon sector along the auroral oval. The numerical techniques used for solving the magnetosphere-ionosphere coupling equations are given in the Appendix.

### 3.2 Simulation Model and Governing Equations

In this section, we present the model of the magnetosphere-ionosphere coupling process, as well as the governing equations in the magnetosphere, in the ionosphere, and along the geomagnetic field lines. The simulation domain, the numerical scheme, and the boundary conditions are also presented.

Consider the equatorial plane of the magnetopause-boundary layer region, as shown in Figure 1.2a. As the solar wind flows toward the subsolar point of the magnetopause, it is



diverted toward both the dawnside and duskside of the magnetosheath. A sheared plasma flow is built up due to the velocity difference between the magnetopause and the magnetosphere, which causes vortex motion in the boundary layer region, as mentioned in Chapters 1 and 2. In addition, in order to account for the observed thickness of the boundary layer, there must exist, on the average, a diffusion flux with an inward normal velocity on the order of 2 – 10 km/s along the magnetopause [Eastman, 1979], as shown schematically in Figure 1.2a. This nonzero diffusion velocity at the magnetopause can be due to the electrostatic and electromagnetic plasma waves observed at the magnetopause [Gurnett *et al.*, 1979; Anderson *et al.*, 1982; Tsurutani *et al.*, 1981; LaBelle and Treumann, 1988], as stated and justified in Chapter 2.

As mentioned in Chapter 1, a localized convection electric field is produced due to the vortex motion in the boundary layer. Consequently, the space charges are accumulated and then discharged to the conducting ionosphere through FACs. The dominant FAC flows upward (downward) in the duskside (dawnside) region of the boundary layer, as shown in Figure 1.2b. On the other hand, the dragging effect of the ionosphere due to the finite ionospheric conductivity may damp the plasma convection and cause the decay of the vortices in the boundary layer. Therefore, the magnetosphere and the ionosphere are a coupled system. Some ionospheric signatures may be explained by the coupling of the plasma vortices formed in the magnetopause-boundary layer region to the polar ionosphere. The observed spatially periodic auroral bright spots in the ionosphere may be caused by this coupling.

The magnetosphere-ionosphere coupling model used here consists of three parts: the LLBL in the magnetosphere, the polar ionosphere, and the field-aligned region. First, we consider the flow dynamics in the equatorial plane of the LLBL, as shown in Figure 1.2a. The simulation domain is chosen to be a rectangular box in the  $x$ - $y$  plane with  $0 \leq x \leq L_x$

and  $0 \leq y \leq L_y$ . The  $x$ -axis is along the magnetopause and points from the subsolar region to the magnetotail and the  $y$ -axis is perpendicular to the magnetopause and points from the magnetopause to the Earth, as shown in Figure 3.1a. This coordinate system is the same for both the duskside and dawnside of the boundary layer. The  $z$ -axis points upward from the equatorial plane. The governing equations in the magnetosphere are the mass conservation and the momentum equation:

$$\frac{\partial \rho}{\partial t} = -\nabla_m \cdot (\rho \mathbf{v}) \quad (3.1)$$

$$\frac{\partial \mathbf{v}}{\partial t} = -\mathbf{v} \cdot \nabla_m \mathbf{v} - \nabla_m P / \rho + \mathbf{J} \times \mathbf{B} / \rho + \nu \nabla_m^2 \mathbf{v} \quad (3.2)$$

where  $\rho$  is the plasma mass density,  $\mathbf{v}$  is the flow velocity in the  $x$ - $y$  plane,  $\nu$  is the kinematic viscosity,  $P$  is the plasma pressure,  $\mathbf{J}$  is the total current, and  $\mathbf{B}$  is the magnetic field. The subscript  $m$  indicates the magnetosphere. The velocity component  $v_z$  is set to zero. In the present calculation, the plasma flow is treated as incompressible ( $\nabla \cdot \mathbf{v} = 0$ ) and the flow velocity in the  $x$ - $y$  plane may be related to the streamline function,  $\psi$ , and the vorticity,  $\Omega$ , which are given as

$$\mathbf{v} = \nabla_m \psi \times \hat{\mathbf{z}} \quad (3.3)$$

$$\nabla_m^2 \psi = -\Omega \quad (3.4)$$

The convection electric field in the magnetosphere  $\mathbf{E}_m$  is given as

$$\mathbf{E}_m = -\nabla_m \phi_m = -\mathbf{v} \times B_0 \hat{\mathbf{z}} \quad (3.5)$$

where  $\phi_m$  is the electric field potential in the magnetosphere and  $B_0$  is the magnetospheric magnetic field in the equatorial plane.

Furthermore, if the plasma flow in the LLBL is not allowed to cause variation of the magnetic field, namely,  $\mathbf{B} = B_z \hat{\mathbf{z}}$  with  $B_z = B_0 = \text{constant}$ , the momentum equation (3.2)

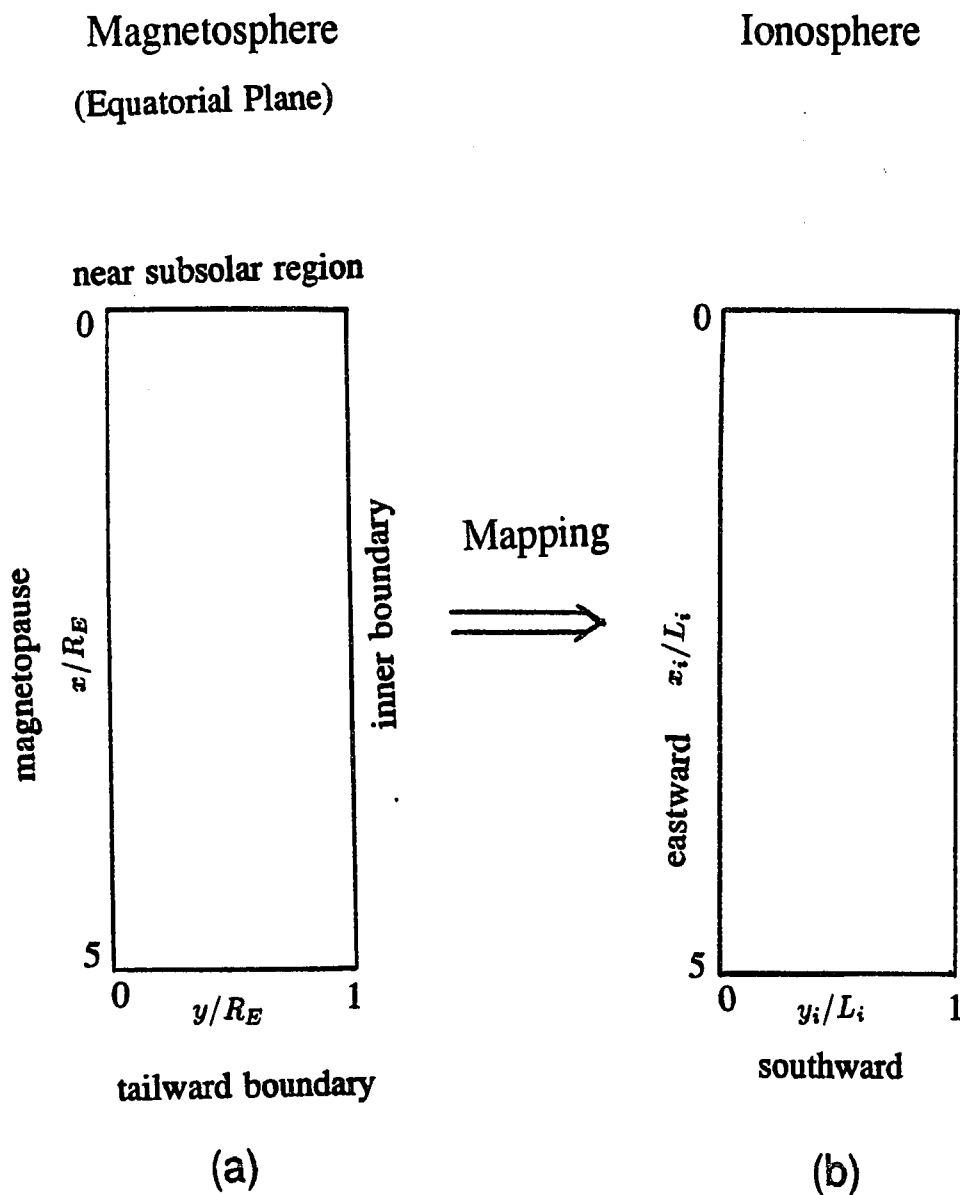


**Figure 3.1** Schematic sketches of simulation domains for the duskside magnetopause driven cases (a) in the magnetosphere and (b) its mapping to the polar ionosphere. An constant and isotropic length mapping factor is used. A length of  $1 R_E$  in the low-latitude boundary layer maps to a length of  $L_i = 185$  km in the polar ionosphere. In the ionosphere the  $x_i$ -axis points eastward and the  $y_i$ -axis points southward.

can be rewritten in the form of the vorticity by taken curl of (3.2). In order to let the curl of the second term on the right hand side of (3.2) vanish, it is assumed that the plasma pressure is only a function of the plasma density. The curl of the third term on the right hand side of (3.2) is related to the generation of FACs in the magnetosphere. By using the current continuity ( $\nabla_m \cdot \mathbf{J}_m = 0$ ) and the assumed constant magnetic field, it can be shown that [e.g., *Lotko et al.*, 1987]

$$\nabla \times ((\mathbf{J} \times \mathbf{B})/\rho) \simeq (B_0 \frac{\partial J_{\parallel}}{\partial z}) \hat{\mathbf{z}}/\rho \quad (3.6)$$

where  $J_{\parallel}$  is the FAC density. To simplify the FAC model, we assume that all of the FAC flowing in the magnetosphere can be treated as a current sheet concentrated within a finite region around the equatorial plane of the magnetosphere with an effective thickness  $2H$ , where  $H$  is the effective half-thickness of the current sheet at the northward (or southward) of the equatorial plane of the magnetosphere. Then, we have

$$\frac{\partial J_{\parallel}}{\partial z} \simeq \langle \frac{\partial J_{\parallel}}{\partial z} \rangle \equiv \frac{1}{H} \int_0^H \frac{\partial J_{\parallel}}{\partial z} dz = \frac{J_{\parallel m}}{H} \quad (3.7)$$

where  $J_{\parallel m}$  is the FAC density at its low-altitude boundary  $z = H$ . Therefore, taking curl of (3.2) and using (3.6) and (3.7), we have the vorticity equation:

$$\frac{\partial \Omega}{\partial t} = -\mathbf{v} \cdot \nabla_m \Omega + (B_0 J_{\parallel m})/(H\rho) + \nu \nabla_m^2 \Omega \quad (3.8)$$

The above approach for the plasma flow dynamics in the LLBL is similar to that used by *Sonnerup* [1980] and *Lotko et al.* [1987].

Next, we consider the ionospheric response. The polar ionosphere is assumed to be a thin conducting layer (local slab geometry), which is characterized by the current continuity

equation and the Ohm's law including the height-integrated Pedersen ( $\Sigma_p$ ) and Hall ( $\Sigma_h$ ) conductivities. The governing equation is

$$J_{\parallel i} = \nabla_i \cdot (\Sigma_p \mathbf{E}_i + \Sigma_h \hat{\mathbf{z}} \times \mathbf{E}_i) \quad (3.9)$$

where  $J_{\parallel i}$  is the FAC density in the ionosphere, subscript  $i$  indicates the ionosphere, and  $\mathbf{E}_i$  is the electric field in the ionosphere. The ionospheric electric field  $\mathbf{E}_i$  can be expressed as

$$\mathbf{E}_i = -\nabla_i \phi_i \quad (3.10)$$

where  $\phi_i$  is the electric field potential in the ionosphere. The coordinate system used in the polar ionosphere is consistent with that in the LLBL. When the coordinate system in the LLBL maps to the polar ionosphere, the  $x$ -axis points eastward and the  $y$ -axis points southward (equatorward), as shown in Figure 3.1b. The  $z$ -axis points downward. The magnetic field is vertical ( $\mathbf{B}_i = B_i \hat{\mathbf{z}}$ ) and may also be considered as a constant over the effective height of the ionosphere. The field-aligned current is chosen to be positive if it is directed downward from the magnetosphere to the polar ionosphere (along the  $z$ -direction).

In the present model, the ionospheric conductivity is allowed to be enhanced due to precipitation of accelerated electrons in the upward FAC region ( $J_{\parallel i} \leq 0$ ), which has the form

$$\Sigma_p = \Sigma_{p0} \begin{cases} (1 + \beta \phi_i^2)^{1/2} & \text{if } J_{\parallel i} < 0 \\ 1 & \text{if } J_{\parallel i} > 0 \end{cases} \quad (3.11)$$

where  $\Sigma_{p0}$  is the uniform background Pedersen conductivity and  $\beta$  is a function of the ionization and the recombination coefficient [Kan and Lee, 1980; Kan and Kamide, 1985].

The field-aligned potential drop ( $\phi_{\parallel}$ ) between the magnetosphere and the ionosphere may be expressed as

$$\phi_{\parallel} = \phi_i - \phi_m \quad (3.12)$$

For  $\phi_{\parallel} > 0$ , the potential rises toward the ionosphere and the FAC is directed upward ( $J_{\parallel} < 0$ ). For simplicity, the ratio of the Hall to Pedersen conductivities ( $R_{hp}$ ) is assumed to be a constant and independent of the energy of the precipitating electrons.

$$\Sigma_h = R_{hp}\Sigma_p \quad (3.13)$$

The model used for the field-aligned effects is the linear current-voltage relationship due to the mirror force along the convergent geomagnetic field lines for both upward and downward FACs, but with different proportionality [*Knight, 1973; Fridman and Lemaire, 1980*]:

$$\phi_{\parallel} = \begin{cases} -\alpha J_{\parallel i} & \text{if } J_{\parallel i} < 0 \\ -0.1\alpha J_{\parallel i} & \text{if } J_{\parallel i} > 0 \end{cases} \quad (3.14a)$$

$$(3.14b)$$

where  $\alpha$  depends on the number density and the temperature of the magnetospheric electrons. For upward FAC regions, equation (3.14a) has been used by several authors [*Chiu and Cornwall, 1980; Lyons, 1980, 1981; Chiu et al., 1981; Lotko et al., 1987*], holds for most of the electron energy range [*Knight, 1973; Fridman and Lemaire, 1980*], and is valid for both large-scale and small-scale auroras based on DE satellite observations [*Weimer et al., 1987*]. On the other hand, the relationship (3.14b) is a very rough approximation for downward FAC regions [*Chiu et al., 1981; Lysak and Dum, 1983; Lotko et al., 1987; Weimer et al., 1987; Lu et al., 1991*]. Since the downward FACs are mainly carried by the upward moving electrons, which have no any mirror effect and can move more easily along the geomagnetic field lines, the field-aligned potential drop is expected to be much smaller than that in the upward

FAC regions. A small coefficient (one order less than that in the upward FAC regions) is chosen for the downward FAC regions in the present model. In addition, the linear current-voltage relationship (3.14) is a lumped relation and the use of an electrostatic field-aligned potential drop and the lumped relation means that the Alfvén wave transit time between the magnetosphere and the ionosphere is shorter than the time scale of the evolution of plasma vortices.

To close the governing equations in the magnetosphere, in the ionosphere, and along the geomagnetic field lines, the relationships between  $J_{\parallel i}$  and  $J_{\parallel m}$  and  $\nabla_i$  and  $\nabla_m$  are needed. For simplicity a constant and isotropic length mapping factor ( $R_x = R_y$ ) is used in the present model, which gives an area mapping factor  $R_m = R_x^2$ . Therefore, we have

$$\nabla_i = R_x \nabla_m \quad (3.15)$$

From the conservation of magnetic flux between the magnetosphere and the ionosphere, one can obtain  $R_m = B_i/B_0$ . Then from the conservation of the total field-aligned current, we have

$$J_{\parallel i} = \frac{B_i}{B_0} J_{\parallel m} = R_m J_{\parallel m} \quad (3.16)$$

Equations (3.1), (3.3)–(3.5), (3.8)–(3.16), together with appropriate boundary conditions in the magnetosphere and in the ionosphere, are sufficient to determine the dynamics in the magnetosphere, in the ionosphere, and along geomagnetic field lines.

In summary, the magnetosphere-ionosphere coupling model presented here is an incompressible fluid model for the plasma flow dynamics in the LLBL and its interaction with the polar ionosphere via FACs and a parallel electric field. The principal characteristics of the model are: (a) the magnetosphere is modeled as an incompressible flow with the mass transport across the magnetopause; (b) the ionosphere is characterized by the current continuity

equation and the Ohm's law including the height-integrated Pedersen conductivity and Hall conductivity; and (c) a linear current-voltage relationship is used for both upward and downward FACs along the magnetic field lines. In the present model, the ionospheric conductivity is allowed to be enhanced due to precipitation of the accelerated electrons in the upward FAC region.

Simplifications of the magnetosphere-ionosphere coupling equations are possible if some variations can be ignored. If the ionospheric conductivities are assumed to be uniform (by setting  $\beta = 0$  in the present model), as have been used by many authors [e.g., *Lotko et al.*, 1987; *Keskinen et al.*, 1988], the coupling equations can be simplified significantly. It can be obtained from (3.9) and (3.10) that

$$J_{\parallel i} = \Sigma_{p0} \nabla_i \cdot \mathbf{E}_i = -\Sigma_{p0} \nabla_i^2 \phi_i \quad (3.17)$$

As indicated by (3.17), the Hall conductivity has no effect on the coupling. Inserting (3.12), (3.14), and (3.15) into (3.17), one obtains

$$(1 - \kappa \lambda_m^2 \nabla_m^2) \phi_{\parallel} = -\kappa \lambda_m^2 \nabla_m^2 \phi_m \quad (3.18)$$

which is similar to equation (7) in *Lotko et al.*'s [1987] paper. In (3.18)  $\lambda_m = R_x \lambda_i = R_x \sqrt{\alpha \Sigma_p}$  and  $\lambda_m$  and  $\lambda_i$  are the resistive scale lengths in the magnetosphere and in the ionosphere, respectively [*Chiu and Cornwall*, 1980; *Lyons*, 1980; *Lotko et al.*, 1987; *Weimer et al.*, 1987]. We have  $\kappa = 1$  for upward FACs and  $\kappa = 0.1$  for downward FACs, similar to the definition in (3.14). In addition, it can be easily shown that by taking dot product of two expressions of (3.5)

$$\nabla_m^2 \phi_m = -B_0 \nabla_m^2 \psi = B_0 \Omega \quad (3.19)$$

The magnetosphere-ionosphere coupling model presented above is referred as the imperfect coupling because the geomagnetic field lines are non-equipotential ( $\phi_{\parallel} \neq 0$ ) [e.g.,



Kan and Lee, 1980]. If  $\phi_{\parallel} = 0$ , the magnetosphere-ionosphere coupling is called the perfect coupling, which can be obtained from our model by setting  $\alpha = 0$ . In this case,  $\Sigma_p = \Sigma_{p0}$ ,  $\phi_i = \phi_m$ , and one obtains from (3.15) and (3.9) that

$$J_{\parallel i} = R_m \Sigma_{p0} \nabla_m \cdot \mathbf{E}_m = -R_m \Sigma_{p0} B_0 \Omega \quad (3.20)$$

It can be seen that  $J_{\parallel i}$  is proportional to the vorticity. By using (3.16) and (3.20), (3.8) becomes

$$\frac{\partial \Omega}{\partial t} = -\mathbf{v} \cdot \nabla_m \Omega - \frac{B_0^2 \Sigma_{p0}}{H \rho} \Omega + \nu \nabla_m^2 \Omega \quad (3.21)$$

Therefore, equations (3.1), (3.21), (3.3), and (3.4) form a complete set of equations describing the perfect magnetosphere-ionosphere coupling. The first term on the right hand side of (3.21) is a nonlinear convection term and represents the convection of the plasma flow. The second term has a pure decay effect. The third term has the viscous effect, which is small and negligible. Furthermore, if it is assumed that the flow is one-dimensional,  $\rho = \text{constant} = \bar{N} m_i$  ( $\bar{N}$  is the average plasma number density in the boundary layer), and  $\nu = 0$ , (3.21) can be reduced to

$$\frac{\partial \Omega}{\partial t} = -\frac{B_0^2 \Sigma_{p0}}{H \bar{N} m_i} \Omega \quad (3.22)$$

which has a solution

$$\Omega = \Omega_0 e^{-t/T_d} \quad (3.23)$$

where

$$T_d = \frac{H \bar{N} m_i}{B_0^2 \Sigma_{p0}} \quad (3.24)$$

is the characteristic decay time and  $\Omega_0$  is the vorticity at time  $t = 0$ .

The coupling equations presented above are in dimensional forms. In the numerical simulation, the coupling equations can be put in dimensionless forms by appropriate normalizations. In the present study, the length is normalized by a characteristic perpendicular length in the magnetosphere,  $a$ ; the velocity by the plasma velocity parallel to the magnetopause,  $V_0$ ; the density by the magnetospheric uniform number density,  $N_0$ ; the magnetic field by the constant magnetospheric magnetic field,  $B_0$ ; and the ionospheric conductivity by the uniform background Pedersen conductivity,  $\Sigma_{p0}$ . The plasma density is related to the number density by  $\rho = m_i N$ , where  $m_i$  is the ion mass. In addition, the time can be normalized by  $t_0 \equiv a/V_0$ , the vorticity by  $V_0/a$ , the kinematic viscosity by  $aV_0$ , the electric potential by  $\phi_0 \equiv aV_0B_0$ , the field-aligned current by  $J_0 \equiv (B_0R_m)/(\mu_0a)$ , the electric field in the magnetosphere by  $E_0 \equiv B_0V_0$ , and the electric field in the ionosphere by  $E_{0i} \equiv B_0V_0R_x$ . The characteristic perpendicular length in the magnetosphere is chosen to be  $a = 1 R_E$ , where  $R_E = 6400$  km is the Earth radius. The Reynolds number is defined as  $R = aV_0/\nu$ . We set  $R = 1000$  in all cases presented below.

With the above normalizations, the coupling equations in the dimensionless forms can be expressed as

$$\frac{\partial N}{\partial t} = -\mathbf{v} \cdot \nabla N \quad (3.25)$$

$$\frac{\partial \Omega}{\partial t} = -\mathbf{v} \cdot \nabla \Omega + \gamma J_{\parallel i}/N + \nabla^2 \Omega/R \quad (3.26)$$

$$\mathbf{v} = \nabla \psi \times \hat{\mathbf{z}} \quad (3.27)$$

$$\nabla^2 \psi = -\Omega \quad (3.28)$$

$$\phi_m = -\psi \quad (3.29)$$

$$J_{\parallel i} = \Sigma_0 \nabla \cdot (\Sigma_p \mathbf{E}_i + R_{hp} \Sigma_p \hat{\mathbf{z}} \times \mathbf{E}_i) \quad (3.30)$$

$$\Sigma_p = \begin{cases} (1 + \beta_0 \phi_{\parallel}^2)^{1/2} & \text{if } J_{\parallel i} < 0 \\ 1 & \text{if } J_{\parallel i} > 0 \end{cases} \quad (3.31)$$

$$\phi_{\parallel} = \begin{cases} -\alpha_0 J_{\parallel i} & \text{if } J_{\parallel i} < 0 \\ -0.1\alpha_0 J_{\parallel i} & \text{if } J_{\parallel i} > 0 \end{cases} \quad (3.32)$$

$$\mathbf{E}_i = -\nabla \phi_i \quad (3.33)$$

$$\phi_{\parallel} = \phi_i - \phi_m \quad (3.34)$$

$$\gamma = \frac{R_E}{H} \frac{B_0^2}{\mu_0 N_0 m_i V_0^2} \quad \alpha_0 = \frac{\alpha R_m}{\mu_0 R_E^2 V_0} \quad (3.35)$$

$$\beta_0 = \beta \phi_0^2 \quad \Sigma_0 = \Sigma_{p0} \mu_0 V_0 \quad R_{hp} = \Sigma_{h0} / \Sigma_{p0}$$

Equation (3.29) is obtained from (3.19). The physical parameters are related to the five dimensionless parameters in (3.35).

Based on observations [e.g., *Kan and Lee, 1980; Sonnerup, 1980; Lotko et al., 1987; Weimer et al., 1987*], typical values of the physical parameters are given as follows:  $N_0 = 1 \text{ cm}^{-3}$ ,  $V_0 = 200 \text{ km/s}$ ,  $H = 10 R_E$ ,  $B_0 = 50 \text{ nT}$ ,  $B_i = 0.6 \text{ G}$ ,  $\Sigma_{p0} = 2 \text{ mho}$ ,  $\alpha = 10^8 \text{ m}^2/\text{mho}$ ,  $\beta = 1 \text{ kV}^{-2}$ . From the above parameters, it can be found that  $t_0 = 32 \text{ sec}$ ,  $R_m = B_i/B_0 = 1200$ , and  $R_x = \sqrt{R_m} \simeq 34.6$ ,  $\phi_0 = 64 \text{ kV}$ ,  $J_0 \simeq 7.46 \mu\text{A}/\text{m}^2$ ,  $E_0 = 10 \text{ mV/m}$ , and  $E_{0i} \simeq 346 \text{ mV/m}$ . The dimensionless parameters in (3.35) are  $\gamma \simeq 2.97$ ,  $\alpha_0 \simeq 0.0117$ ,  $\beta_0 = 4096$ , and  $\Sigma_0 \simeq 0.5$ , which will be used in our simulations. The value of  $R_{hp}$  is different for different cases and is specified for each case shown below.

The effects of numerical errors should be minimized in order to simulate the fine vortex structures in the boundary layer region. To reduce the numerical diffusion, a high-order finite differencing scheme is used to solve equations (3.17)–(3.20), which has been described in detail in Chapter 2. Since the ionospheric Pedersen and Hall conductivities are not constant, the process to solve the coupling equations is very complicated. To solve for  $\phi_{\parallel}$  or  $J_{\parallel i}$  and

other ionospheric quantities, an iteration method is used. The numerical scheme used to solve  $\phi_{\parallel}$  is the fast Fourier transform along one direction and the tridiagonal method along another direction. The detailed numerical techniques used to solve the coupling equations are given in the Appendix.

At the driven part of the magnetopause boundary ( $y = 0$ ), the plasma density ( $N$ ) and the tangential velocity ( $v_x$ ) are maintained at their magnetosheath values ( $N = 10N_0$  and  $v_x = V_0$ ); the normal velocity ( $v_y$ ) is kept constant during the simulation but may be different at different locations. For the remaining portion, boundary conditions for the plasma density and the flow velocity are  $\frac{\partial N}{\partial y} = \frac{\partial v_x}{\partial y} = \frac{\partial v_y}{\partial y} = 0$ . Along the inner boundary ( $y = L_y$ ), we set  $N = N_0$ ,  $\Omega = 0$ , and  $\psi = 0$ . At the tailward ( $x = L_x$ ) and the subsolar ( $x = 0$ ) boundaries, we set  $\frac{\partial N}{\partial x} = 0$ ,  $\frac{\partial \psi}{\partial x} = 0$ , and  $\frac{\partial \Omega}{\partial x} = 0$  to allow an outflow of the boundary layer plasma. The boundary conditions for  $\phi_{\parallel}$  are  $\frac{\partial \phi_{\parallel}}{\partial x} = 0$  at  $x = 0$  and  $x = L_x$  and  $\frac{\partial \phi_{\parallel}}{\partial y} = 0$  at  $y = 0$  and  $y = L_y$ . We set  $L_x = 5 R_E$  and  $L_y = 1 R_E$ . A uniform grid mesh is used which contains  $321 \times 65$  grid points.

### 3.3 Simulation Results

In this section the simulation results from different cases with different boundary conditions at the magnetopause are presented. First, we show the results with periodic boundary conditions in the magnetosphere. Second, the driven boundary conditions are used along the whole duskside region of the magnetopause. Third, the driven boundary conditions are used in a localized region of the duskside region of the magnetopause. Finally, the coupling of the dawnside region of the magnetopause to the pre-noon side of the polar ionosphere is presented.

### 3.3.1 Periodic Cases

Here we show the simulation results for the pure Kelvin-Helmholtz instability in the duskside region of the boundary layer, in which a periodic boundary condition is imposed along the  $x$ -direction and the boundaries at  $y = 0$  and  $y = 1 R_E$  are far away from the central shear region. The simulation domain and the boundary conditions are different from those with the driven boundary conditions and are specified below. The initial profiles of the plasma density and the flow velocity are given as

$$N = \frac{1}{2}(N_1 + N_2) - \frac{1}{2}(N_1 - N_2) \tanh\left(\frac{y - 0.5R_E}{a_v}\right) \quad (3.36)$$

$$v_x = \frac{1}{2}V_0 \left[1 - \tanh\left(\frac{y - 0.5R_E}{a_v}\right)\right] \quad (3.37)$$

where  $N_1 = 10N_0$  is the plasma density in the magnetosheath,  $N_2 = N_0$  is the plasma density in the magnetosphere,  $V_0$  is the tailward velocity at the magnetopause ( $y = 0$ ), and  $a_v = 0.04 R_E$  is the half-thickness of the transition layer for both the plasma density and the flow velocity. As given in (3.37), the velocity in the magnetosphere side is zero. A uniform grid mesh is used which contains  $64 \times 64$  grid points.

The simulation domain is in the  $x$ - $y$  plane with  $0 \leq x \leq 1 R_E$  and  $0 \leq y \leq 1 R_E$ . The periodic boundary condition is used along the  $x$ -direction. The boundary conditions along  $y = 0$  (left boundary) and  $y = 1 R_E$  (right boundary) are  $\frac{\partial N}{\partial y} = \frac{\partial v_x}{\partial y} = \frac{\partial v_y}{\partial y} = 0$ . A small perturbation in vorticity is introduced explicitly at the beginning of the simulation. The perturbed wavelength is half of the total length in the  $x$ -direction. The details may be found in Chapter 2.

Figure 3.2 shows contour plots of the magnetospheric plasma density, vector plots of the flow velocity, contour plots of the FAC density, and contour plots of the ionospheric

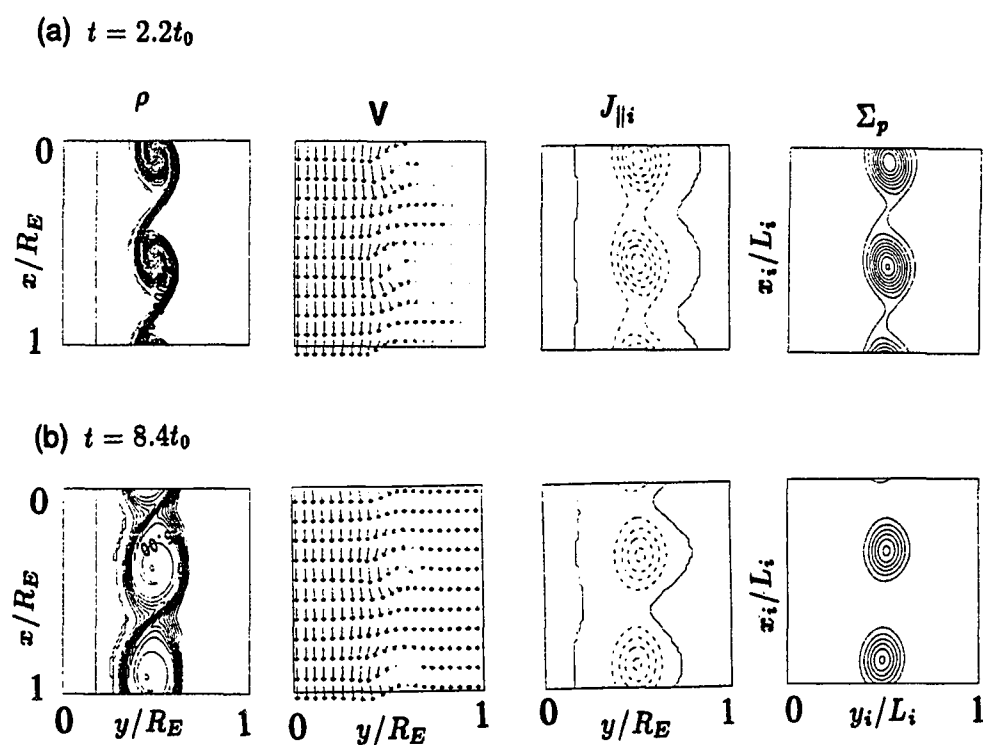


**Figure 3.2** Four two-dimensional plots for a case with periodic boundary conditions in the boundary layer and  $R_{hp} = 1$ . Shown above are contour plot of the plasma density, vector plot of the flow velocity in the magnetosphere, contour plot of the FAC density, and contour plot of the ionospheric conductivity at two simulation times (a)  $t = 2.2t_0$  and (b)  $t = 8.4t_0$ .

Pedersen (or Hall) conductivity at two simulation times (a)  $t = 2.2t_0$  and (b)  $t = 8.4t_0$  for the case with  $R_{hp} = 1$ . Due to the presence of the velocity shear, the KH instability develops, creating vortex motion in the simulation domain. The vortex motion twists the plasma density distribution. As a consequence, the vortex structures are formed. As the KH instability develops, the width of the vortex grows and the plasma originating from the magnetosheath mixes with the plasma originating from the magnetosphere, as can be seen from Figure 3.2. Finally, a plasma density plateau is formed around the central part of the boundary layer, which is due to the combined effect of mixing and diffusion.

The coupling of the magnetopause-boundary layer region to the polar ionosphere leads to the damping of the vortices developed in the boundary layer. As a consequence, both the growth rate and the degree of plasma mixing are smaller than those without the coupling process as presented in Chapter 2 (refer Figure 2.8). The width of the mixing region here is relatively small. When the duskside-region of the magnetopause-boundary layer couples to the post-noon polar ionosphere, the generated FAC is directed upward. Contour plots of the FAC density shown in Figure 3.2 are similar to the vortex structures in the boundary layer. Dashed lines indicate that the FAC flows upward from the ionosphere to the magnetosphere ( $J_{\parallel i} < 0$ ). The contour interval for the FAC density is  $1 \mu A/m^2$ . Two enhanced upward FAC regions are formed in the simulation domain, which lead to enhancement of the ionospheric conductivity, as shown in Figure 3.2. The contour interval for the conductivity is 0.1 mho and the background Pedersen (or Hall) conductivity is 2 mho.

Note that for the coupling of the dawnside region of the magnetopause-boundary layer to the pre-noon polar ionosphere, there is nearly no conductivity enhancement, because the FAC is mainly directed downward. On the other hand, the plasma dynamics in the dawnside region are similar to that in the duskside region of the boundary layer. If the background

ionospheric Pedersen conductivity is increased, it can be found that the damping process will be more rapid. In addition, if the average plasma density in the mixing region is larger than the plasma density in the magnetosphere, the damping process will be slower than the case with a uniform magnetospheric density  $\rho_0$ . These can also be seen from the characteristic decay time given in (3.24). If the conductivity  $\Sigma_{p0}$  decreases or the average plasma density  $\bar{N}$  increases, the decay time will be longer and the decay process will be slower.

### 3.3.2 Uniformly Driven Cases Along the Duskside Magnetopause

In this subsection, we study cases with a uniformly driven plasma flow along the duskside magnetopause. The coupling to the post-noon sector of the ionosphere is mainly through the upward FAC. Along the magnetopause boundary, the plasma density is maintained at  $N_1 = 10N_0$  and the velocity tangential to the magnetopause is set to  $v_x = V_0$ . The normal velocity is maintained at a constant value  $v_y = v_{n0}$  along the whole magnetopause. We choose  $v_{n0} = 0.05V_0$  here, which corresponds to 10 km/s for  $V_0 = 200$  km/s. A uniform grid mesh is used which contains  $321 \times 65$  grid points. To avoid large gradients in the plasma density and the flow velocity near the magnetopause, the values imposed at the inflow boundary ( $y = 0$ ) increase from the magnetospheric values to the magnetosheath ones in a time interval  $\delta t = 0.4t_0$ . Two cases with different conductivity ratios ( $R_{hp} = 1$  and 2) and some cases with different  $\alpha$  are presented below.

Figure 3.3 shows (a) contour plot of the plasma density, (b) vector plot of the flow velocity in the magnetosphere, (c) contour plot of the FAC density, (d) contour plot of the Hall portion of the FAC density, and (e) contour plot of the ionospheric Pedersen (or Hall) conductivity at a later stage of the simulation for the case with  $R_{hp} = 1$ . Solid (dashed)



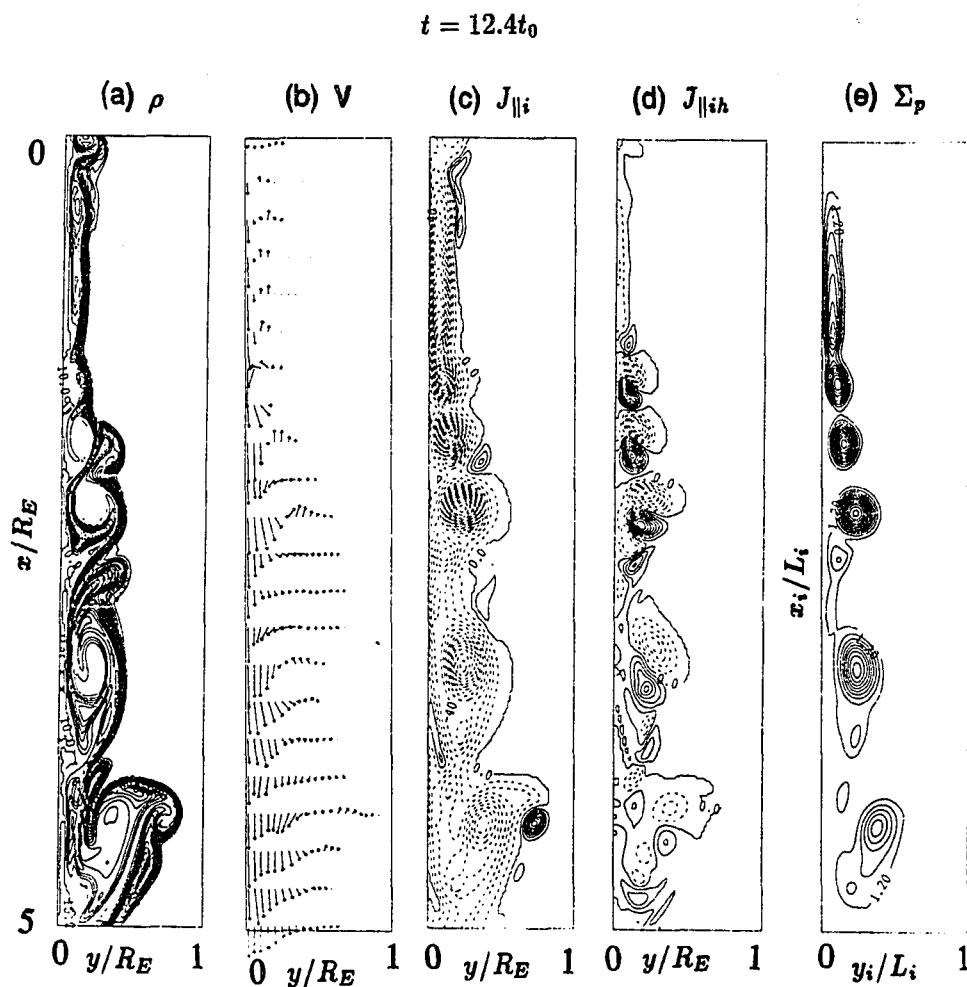


**Figure 3.3** Five two-dimensional plots for a case with the uniform driven condition at the duskside region of the magnetopause and  $R_{hp} = 1$ . Show above are (a) contour plot of the plasma density, (b) vector plot of the flow velocity in the magnetosphere, (c) contour plot of the FAC density, (d) contour plot of the Hall portion of the FAC density, and (e) contour plot of the ionospheric Pedersen conductivity at a later stage of the simulation.

lines indicate positive (negative) values. The contour interval for the FAC is  $1.9 \mu\text{A}/\text{m}^2$  and the contour interval for the conductivity is 0.2 mho. The background Pedersen (or Hall) conductivity is 2 mho. The sheared plasma flow is built up in the boundary layer near the magnetopause due to the tangential plasma flow at the magnetopause. As a consequence, the KH instability develops, leading to the formation of localized vortices in the boundary layer. These vortex structures are first formed near  $x = 1 R_E$  and then convected tailward. In the mean time, they are observed to grow in size. The boundary layer thickness is observed to increase with increasing distance from the subsolar point. The plasma flow in the boundary layer is mainly tailward and a small portion of sunward flow is also observed. The simulation results of the plasma flow here are similar to the transient flow patterns associated with the 14 MLT auroral event observed by radar [Sandholt *et al.*, 1990].

Due to the damping effect through the finite ionospheric conductivity, the motion of the boundary layer plasma is slowed down. The boundary layer thickness becomes smaller than that of the similar case in Chapter 2 (refer Figure 2.6). The coalescence of vortices is also observed, but the effect is much smaller than the case without coupling as shown in Figure 2.6.

The FAC density plot shown in Figure 3.3 indicates that the FAC flows mainly upward, although some small return current regions are also observed. Several enhanced upward FAC regions are observed, which are associated with the vortex motion in the boundary layer. The maximum enhanced FAC region is located at  $x \sim 2.3 R_E$  (or  $x_i \sim 2.3 I_i$  along the auroral oval). The maximum upward FAC density is  $\sim 35 \mu\text{A}/\text{m}^2$ , which gives a maximum field-aligned potential drop of  $\sim 3.5 \text{ kV}$ . As can be seen, the enhanced FAC region is formed in the boundary layer near the subsolar region. The intensity reaches maximum as the vortex convects tailward and then the intensity decreases as the vortex convects further tailward. The

Hall portion of the FAC ( $J_{\parallel ih} = \nabla \Sigma_h \cdot \hat{z} \times \mathbf{E}_i$ ) is also shown in Figure 3.3. The noteworthy feature is the paired structure of  $J_{\parallel ih}$ . Each paired structure corresponds to an enhanced FAC region or an enhanced conductivity region (which will be studied in detail later), as can be seen from the FAC density and conductivity plots in Figure 3.3. The maximum upward  $J_{\parallel ih}$  is  $14 \mu\text{A}/\text{m}^2$  and the maximum downward  $J_{\parallel ih}$  is  $18 \mu\text{A}/\text{m}^2$ . The Hall portion of the FAC density ( $J_{\parallel ih}$ ) may have a significant contribution to the total FAC density in certain regions.

The Hall portion of the FAC ( $J_{\parallel ih}$ ) is due to the nonuniform conductivity in the ionosphere. If the ionospheric conductivity is uniform, then it can be seen that  $J_{\parallel ih} = \nabla \Sigma_h \cdot \hat{z} \times \mathbf{E}_i = 0$ . To explain the paired structure of  $J_{\parallel ih}$ , we assume  $\mathbf{E}_i \sim \mathbf{E}_m$  for simplicity. Using (3.5) and the above assumption, it can be shown that  $J_{\parallel ih} \sim -\mathbf{v} \cdot \nabla \Sigma_h$ . For each of the enhanced conductivity regions,  $\nabla \Sigma_h$  is directed toward the center of the region. On the other hand, the plasma flow is mainly tailward in the boundary layer (or eastward along the auroral oval). Therefore, in the westward (sunward) part of an enhanced conductivity region (a small  $x_i$ )  $\nabla \Sigma_h \parallel \mathbf{v}$  and  $J_{\parallel ih} < 0$ , while at the eastward (tailward) part of the region (a large  $x_i$ )  $\nabla \Sigma_h \parallel -\mathbf{v}$  and  $J_{\parallel ih} > 0$ . Therefore, each paired structure of  $J_{\parallel ih}$  corresponds to an enhanced conductivity region or an enhanced upward FAC region.

The conductivity plot in Figure 3.3 shows several enhanced regions, corresponding to the enhanced upward FAC regions. The maximum Pedersen (or Hall) conductivity is  $\sim 7.4$  mho, which is about 3.7 times of its background value. We use the enhancement of the ionospheric conductivity as an indication of the intensity of auroral activity since the conductivity enhancement represents the ionospheric ionization and recombination effect. A high enhancement of the ionospheric conductivity indicates an intense auroral activity. Therefore, each of the enhanced conductivity regions represents an auroral bright spot. To see the development and evolution of these auroral bright spots in detail, Figure 3.4 shows

### Pedersen (or Hall) Conductivity Contours

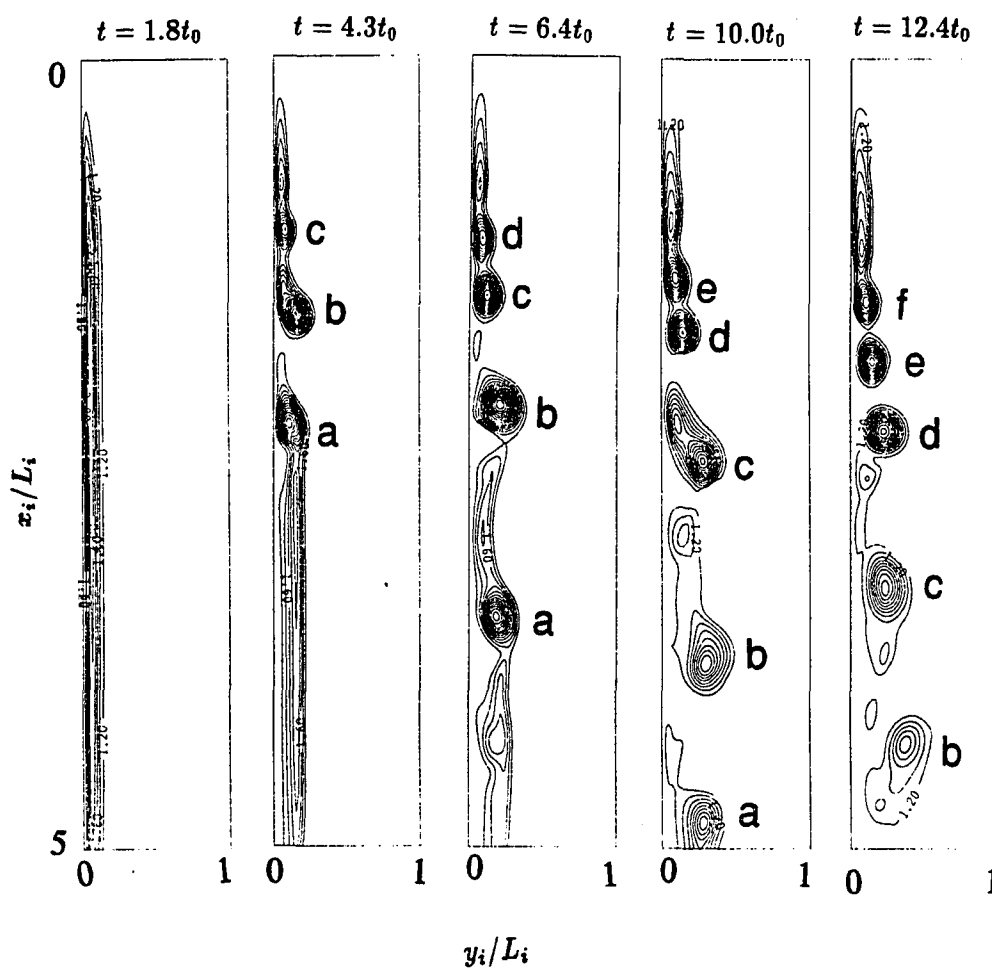


**Figure 3.4** Contour plots of the ionospheric Pedersen (or Hall) conductivity at different simulation times for the above case. The background conductivity is 2 mho and the contour interval is 0.2 mho.

the conductivity plots at different simulation times. It can be seen that, as time goes on, several bright spots are formed and they are convected eastward along the auroral oval (or tailward motion in the magnetosphere). The auroral bright spot is first formed at about  $x_i \sim 1L_i$ , coincidence with the development of the KH instability in the magnetosphere. As the auroral bright spot moves eastward, the intensity increases and reaches maximum at about  $x_i \sim 2.5L_i$ . Then the intensity decreases and the auroral bright spot becomes dim. Finally, the auroral bright spot decays away due to the ionospheric damping effect. The convection speed of the auroral bright spots is  $\sim 1 - 2$  km/s in the polar ionosphere, which corresponds to a tailward convection speed of  $\sim 36 - 72$  km/s in the magnetosphere. The scale size of each auroral bright spot is  $\sim 40 - 100$  km and becomes large when it moves eastward. The separation distance between two successive auroral bright spots is  $\sim 50 - 200$  km and also becomes large when the auroral bright spots convect eastward. It should be mentioned that the constant length mapping factor between the magnetosphere and the ionosphere used in the present model becomes invalid at the tailward region of the magnetopause-boundary layer. A very large tailward region may just map to a very small region in the polar ionosphere. When this mapping distortion effect is considered, both the scale size and the separation distance of the auroral bright spots and the eastward convection speed along the auroral oval will approximately be the low limit as given above. The convection speed, the scale size, and the separation distance of these auroral bright spots observed in the simulation are consistent with the observed auroral bright spots by the Viking satellite [Lui *et al.*, 1989].

Figure 3.5 shows (a) contour plot of the plasma density, (b) vector plot of the flow velocity in the magnetosphere, (c) contour plot of the FAC density, (d) contour plot of the Hall portion of the FAC density, and (e) contour plot of the ionospheric Pedersen conductivity at a later stage of the simulation for the case with  $R_{hp} = 2$ . This case is similar to the case

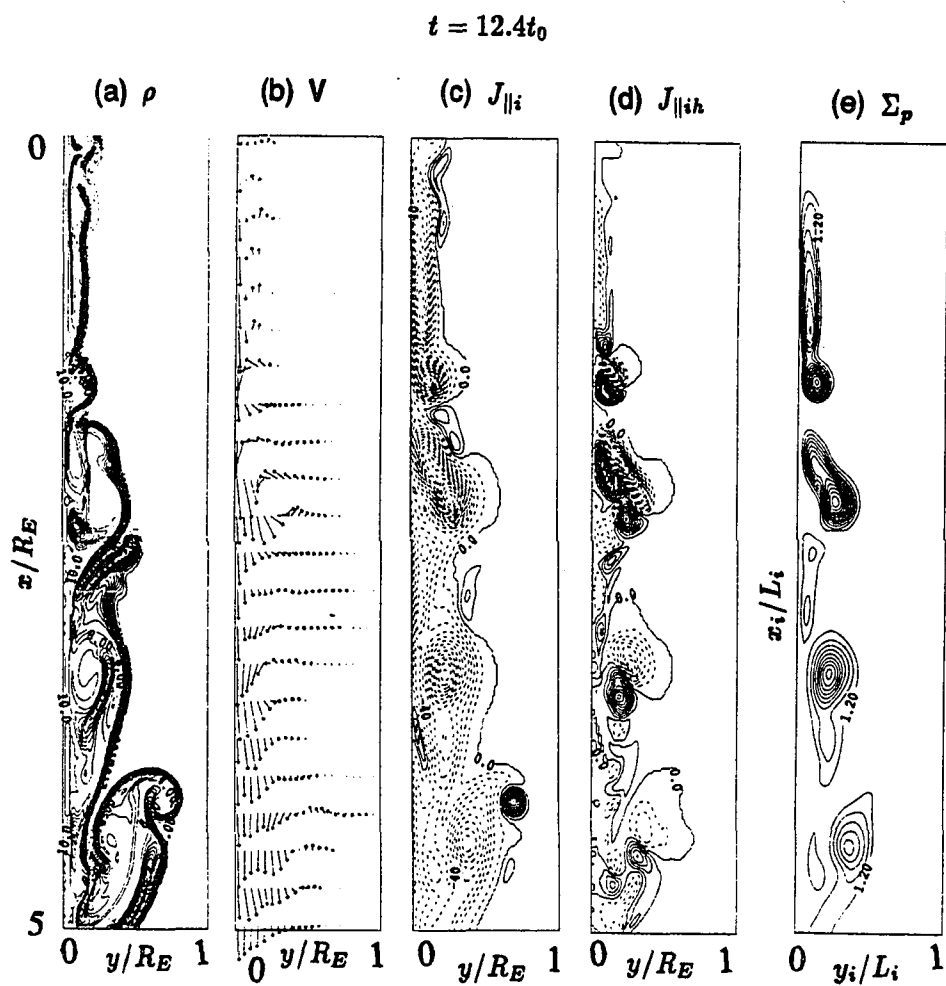


**Figure 3.5** Same as Fig. 3.3, but for a case with the uniform driven condition at the duskside region of the magnetopause and  $R_{hp} = 2$ .

shown before (Figure 3.3) except for a large Hall conductivity. The arrangement and contour intervals are the same as in Figure 3.3. It can be seen that the overall simulation results are similar to the previous case shown in Figure 3.3 except the distribution of the FAC density. The maximum upward FAC density is  $\sim 34 \mu\text{A}/\text{m}^2$ , which gives a maximum field-aligned potential drop of  $\sim 3.4 \text{ kV}$ . The maximum upward  $J_{\parallel ih}$  is  $29 \mu\text{A}/\text{m}^2$  and the maximum downward  $J_{\parallel ih}$  is  $45 \mu\text{A}/\text{m}^2$ . The maximum enhancement of the ionospheric conductivity is about 3.5 times of its background value, which gives a maximum Pedersen conductivity of  $\sim 7 \text{ mho}$  and a maximum Hall conductivity of  $\sim 14 \text{ mho}$ .

The noteworthy difference between the case shown previously (with  $R_{hp} = 1$ ) and the case shown here (with  $R_{hp} = 2$ ) is the intensity of Hall portion of the FAC density,  $J_{\parallel ih}$ . From the data given above, it can be seen that the maximum value of  $|J_{\parallel ih}|$  can exceed the maximum value of  $|J_{\parallel i}|$  at some regions. Therefore, the distribution of the FAC density may be different at these regions from the case with  $R_{hp} = 1$ , as can be seen near the region of  $x \sim 1.7R_E$  in Figures 3.3 and 3.5.

The formation and decay of the enhanced conductivity regions in the post-noon ionosphere are, respectively, due to the development of the KH instability in the magnetosphere and the finite ionospheric conductivity. In the presence of a driven plasma flow along the magnetopause, a sheared plasma flow is built up in the boundary layer. Consequently, the KH instability develops, leading to the formation of vortices in the boundary layer. Several enhanced FAC regions are observed, which are associated with the vortices in the boundary layer. The enhanced upward FAC regions will lead to the enhancement of the ionospheric conductivity. On the other hand, the finite ionospheric conductivity provides the damping to the plasma dynamics in the boundary layer, which leads to the decay of the vortices. The reduced vortices lead to a relatively small enhancement of the FAC density, and, therefore, a

small enhancement of the ionospheric conductivity in the upward FAC regions. The competing effect of the formation and decay of vortices leads to the formation of strong vortices only in limited regions in the boundary layer, and hence limited enhanced conductivity regions along the auroral oval in the post-noon ionosphere.

To quantify the process described above, the characteristic growth and decay times may be estimated as follows. For the formation and the growth of the vortices, the maximum linear growth rate of the KH instability may be used, which is approximately given as  $\gamma_g \simeq 0.1V_0/\Delta a$  [e.g., Lee *et al.*, 1981; Miura and Pritchett, 1982; Miura, 1984], where  $V_0$  is the velocity difference between the magnetopause and the inner boundary of the boundary layer and  $\Delta a$  is the transition width of the velocity shear. For the simulation cases shown above,  $V_0 = 200$  km/s and  $\Delta a$  increases with increasing distance from the subsolar point. From Figures 3.3 and 3.5, it can be seen that, near the subsolar region,  $\Delta a \simeq 1000$  km and the growth time can be estimated as  $T_g = \gamma_g^{-1} \simeq 50$  sec, while near the tailward boundary,  $\Delta a \simeq 3200$  km and  $T_g = \gamma_g^{-1} \simeq 160$  sec. To estimate the decay of vortices due to the ionospheric conductivity, we assume  $\alpha = 0$  (the perfect magnetosphere-ionosphere coupling) and  $N = \bar{N} = \text{constant}$  for simplicity, where  $\bar{N} \simeq 5N_0$  is the average plasma density in the boundary layer. Using these assumptions, the decay time can be estimated as in (3.24), which is given as  $T_d \simeq (H\bar{N}m_i)/(\Sigma_{p0}B_0^2) \simeq 107$  sec with the parameters used in the simulations. It can be seen that the decay time is larger than the growth time near the subsolar region ( $T_d > T_g$ ), but smaller than the growth time near the tailward boundary ( $T_d < T_g$ ). Therefore, the KH instability can develop near the subsolar region and form vortices. As the plasma flows tailward, the decay gradually becomes the dominant process which leads to the damping of the vortices formed previously. The combined effect leads to



limited regions of the enhanced vorticity, which leads to finite enhanced conductivity regions along the post-noon auroral oval.

The effects of the FAC and the field-aligned potential drop can be studied with different field-aligned proportional coefficients. Figure 3.6 shows the maximum FAC density ( $|J_{\parallel i max}|$ ) recorded at time  $t = 8t_0$  as a function of the coupling coefficient  $\alpha$ . The maximum FAC density recorded at  $t > 8t_0$  shows no significant difference. The case with  $\alpha = 0$  is for the perfect magnetosphere-ionosphere coupling. It can be seen that increasing  $\alpha$  leads to a decrease of the maximum FAC density. A small  $|J_{\parallel i max}|$  leads to a slow decay of the vorticity in the magnetosphere, as can be seen from (3.26). Therefore,  $\alpha$  has a destabilizing effect for the dynamics of the magnetopause-boundary layer.

We also simulated some cases with different magnetosheath plasma density ( $N_1$ ) and the background ionospheric Pedersen conductivity ( $\Sigma_{p0}$ ). The cases shown above are the results with  $N_1 = 10 N_0$  and  $\Sigma_{p0} = 2$  mho. It is found that decreasing  $N_1$  or  $\Sigma_{p0}$  leads to a decrease of the maximum values of the enhancement of the ionospheric conductivity, the field-aligned potential drop, and the FAC density. These results can be understood as follows. When  $N_1$  decreases, the average plasma density in the boundary layer decreases, which leads to a large decay, as can be seen from (3.26) (the second term on the right hand side). This large decay leads to a relatively small increase of the FAC density, the field-aligned potential drop, and the ionospheric conductivity. When  $\Sigma_{p0}$  decreases,  $J_{\parallel i}$  decreases, as can be seen from (3.20). The decrease of the FAC density ( $J_{\parallel i}$ ) leads to a decrease of the field-aligned potential drop and a decrease in the enhancement of the ionospheric conductivity.

The simulation results shown above are for a uniformly driven plasma flow along the duskside magnetopause. They are the coupling results of Case B in Chapter 2 to the polar ionosphere. As discussed in Chapter 2, the simulation results of Case D for a sheared plasma

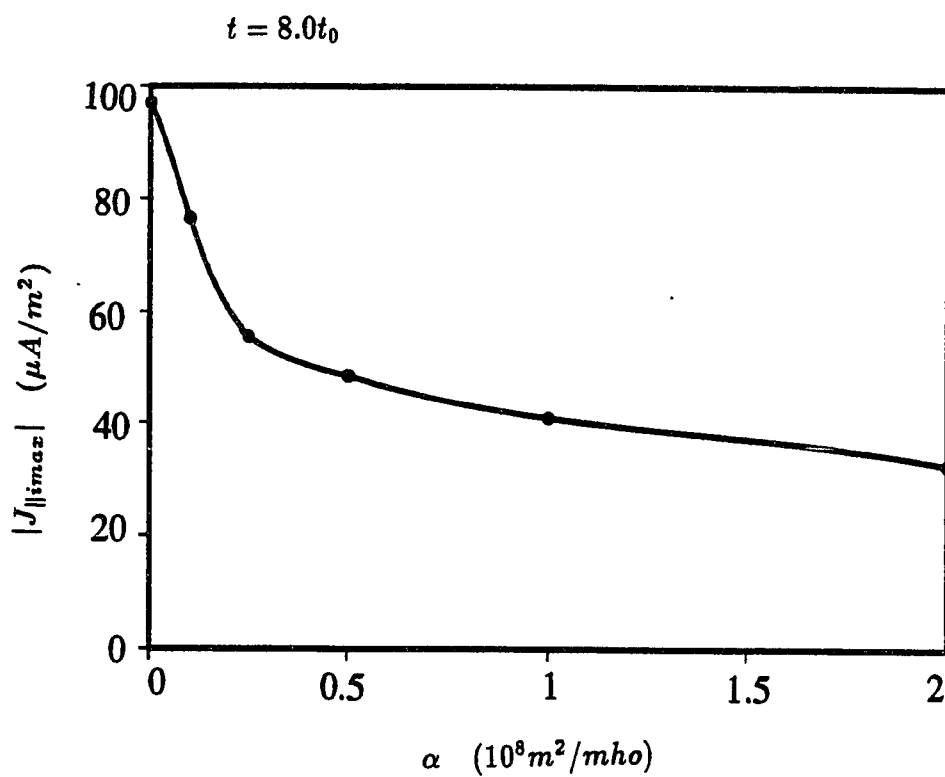


**Figure 3.6** Maximum upward FAC density as a function of the coupling coefficient  $\alpha$  for the uniform driven condition at the duskside region of the magnetopause. Here  $R_{hp} = 1$ . The case with  $\alpha = 0$  is for the perfect magnetosphere-ionosphere coupling.

flow with outflow boundary conditions are similar to those in Case B. Therefore, it is expected that their ionospheric effects will also be similar and the same kind of auroral bright spots will be produced if a sheared plasma flow with outflow boundary conditions (as in Case D of Chapter 2) in the magnetosphere couples to the ionosphere.

### 3.3.3 Locally Driven Cases Along the Duskside Magnetopause

In this subsection, the simulation results of coupling of the duskside region of the magnetopause-boundary layer to the post-noon ionosphere are shown, but the driven boundary conditions are imposed only in a localized region of the magnetopause. The plasma density and the tangential velocity are maintained at their magnetosheath values in the driven region. The plasma density is maintained at  $N_1 = 10N_0$  and the tangential velocity is maintained at  $v_x = V_0$ . A uniform grid mesh is used which contains  $321 \times 65$  grid points.

For simplicity, the normal velocity is taken to be  $v_y = v_{n0} \cos[\frac{\pi}{2h}(x - x_0)]$  in the driven region along the magnetopause  $\{x_0 - h < x < x_0 + h\}$ , where  $v_{n0}$  is the characteristic normal velocity and  $2h$  is the length of the driven region. Outside the driven region, we set  $\frac{\partial N}{\partial y} = \frac{\partial v_x}{\partial y} = \frac{\partial v_y}{\partial y} = 0$  as mentioned before. The normal velocity reaches maximum at the center of the driven region and smoothly decreases to zero at the edges. For this case, we choose  $v_{n0} = 0.15 V_0$ ,  $x_0 = \frac{5}{6} R_E$ , and  $h = \frac{5}{12} R_E$ . To avoid large gradients in the plasma density and the flow velocity in the driven region, the values imposed at the localized driven region at the magnetopause increase from the magnetospheric values to the magnetosheath ones in a time interval  $\delta t = 0.4 t_0$ . These localized driven conditions are the same as those used in Chapter 2.

Figure 3.7 shows (a) contour plot of the plasma density, (b) vector plot of the flow velocity in the magnetosphere, (c) contour plot of the FAC density, (d) contour plot of the Hall portion of the FAC density, and (e) contour plot of the ionospheric Pedersen conductivity at a later stage of the simulation for the case with  $R_{hp} = 2$ . The contour interval for the FAC density is  $1.9 \mu\text{A}/\text{m}^2$  and the contour interval for the ionospheric conductivity is 0.2 mho. The background Pedersen conductivity is 2 mho and the background Hall conductivity is 4 mho. The vortex structures are first formed near  $x = 1.2 R_E$  and grow to the maximum size near  $x = 1.8 R_E$ . Finally, the vortex structures decay away and the boundary layer thickness becomes small due to the ionospheric damping effect, in contrast to the case shown in Chapter 2 (refer Figure 2.2), where the boundary layer thickness can reach a constant value as the plasma flows further tailward. The plasma flow in the boundary layer is mainly tailward and a small portion of sunward flow is observed. A sunward flow is also observed near the subsolar region.

The FAC density shown in Figure 3.7 flows mainly upward with some small return current regions. Several regions of enhanced upward FACs are observed, which are associated with the vortex motion in the boundary layer region. The maximum enhanced FAC region is located at  $x \sim 1.8 R_E$ , corresponding to the maximum vorticity in the boundary layer. The intensity of the FAC density decreases rapidly when the plasma flows further tailward from  $x \sim 2 R_E$ , because of the lack of the driven plasma flow. The Hall portion of the FAC ( $J_{\parallel ih}$ ) in Figure 3.7 also shows the paired structures, similar to those in Figure 3.3. The intensity of the Hall portion of the FAC density may exceed the total FAC density at some regions, similar to the results shown in Figure 3.5. The conductivity plot in Figure 3.3 also shows several enhanced regions, corresponding to the enhanced upward FAC regions. The maximum conductivity enhancement is about 3.8 times of its background value, which

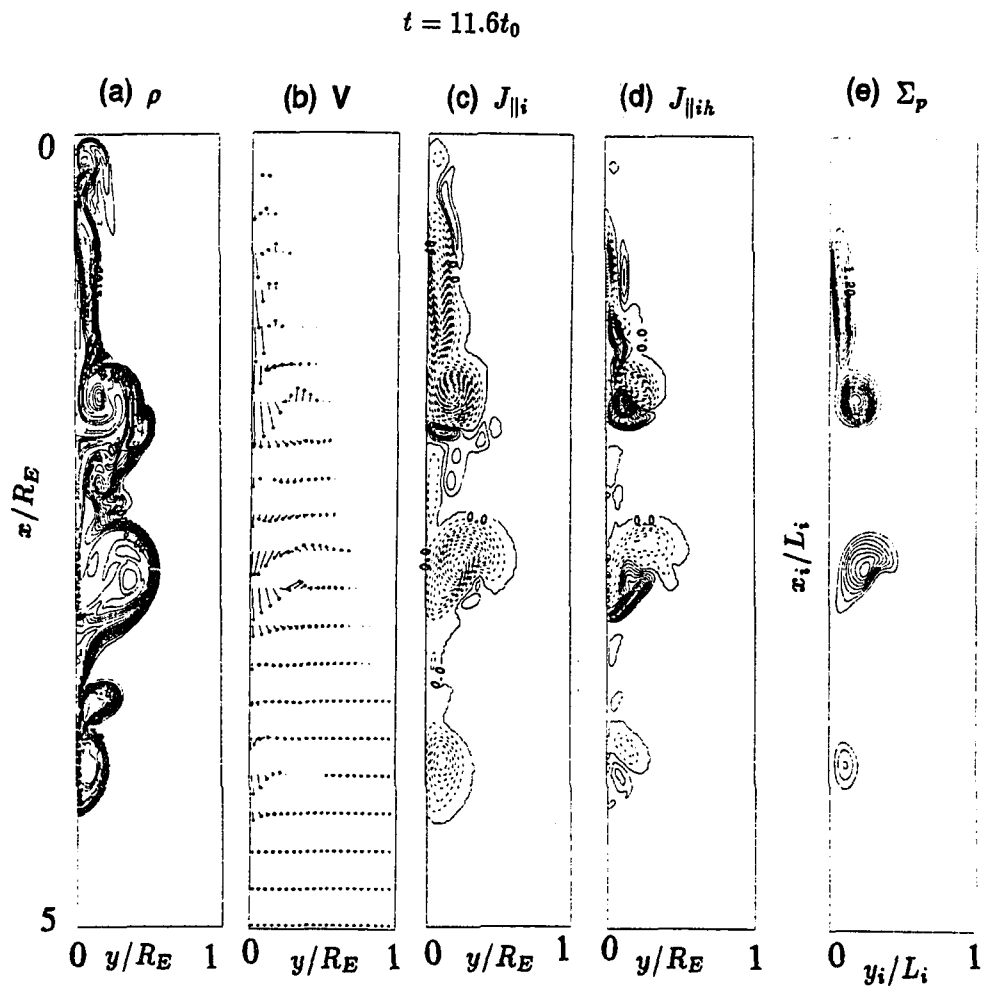


**Figure 3.7** Same as Fig. 3.3, but for a case with the localized driven condition at the duskside region of the magnetopause and  $R_{hp} = 2$ .

gives a maximum Pedersen conductivity of  $\sim 7.6$  mho and a maximum Hall conductivity of  $\sim 15.2$  mho. The enhanced conductivity regions decay away very fast, in contrast to those shown in Figure 3.5.

If the conductivity ratio ( $R_{hp}$ ) is changed, the noteworthy difference is the change of the intensity of the Hall portion of the FAC density,  $J_{\parallel ih}$ . The paired structures are still the dominant feature of  $J_{\parallel ih}$ . When  $R_{hp}$  increases, the intensity of  $J_{\parallel ih}$  increases, which gives a large return current and adds to a significant portion to the total FAC density. Consequently, the distribution of the total FAC density will be different, especially around the region of  $x \sim 1.8 R_E$ . More return (downward) FAC regions are observed. When  $R_{hp}$  decreases, the intensity of  $J_{\parallel ih}$  decreases and the results are similar to those shown in Figure 3.7, except the intensity of  $J_{\parallel ih}$ . In addition, when the maintained plasma density in the driven region at the magnetopause,  $N_1$ , or the background ionospheric conductivity,  $\Sigma_{p0}$ , or the field-aligned coupling coefficient,  $\alpha$ , is changed, the simulation results are similar to those with uniform driven cases shown in the previous subsection.

### 3.3.4 Dawnside Magnetopause Driven Cases

In the previous subsections, we showed the simulation results either with periodic boundary conditions or with driven boundary conditions at the duskside region of the magnetopause. To complete the discussion, we show here the simulation results of coupling of the dawnside region of the magnetopause-boundary layer to the pre-noon ionosphere where the downward FAC is dominant. The driven boundary conditions may be either along the whole magnetopause or through a localized region at the dawnside region of the magnetopause. The treatment of the plasma density and the flow velocity (both tangential and normal) at the

driven region along the magnetopause is the same as in subsection 3.3.2 for the uniform magnetopause driven condition or in subsection 3.3.3 for the localized magnetopause driven condition.

Figure 3.8 shows (a) contour plot of the plasma density, (b) vector plot of the flow velocity in the magnetosphere, (c) contour plot of the FAC density, (d) contour plot of the Hall portion of the FAC density, and (e) contour plot of the ionospheric Pedersen conductivity at a later stage of the simulation in the case with the uniform driven plasma flow at the dawnside region of the magnetopause for  $R_{hp} = 3$ . The plasma density and the flow velocity are similar to those shown in Figure 3.3. The contour intervals are the same as for the duskside magnetopause driven cases. The FAC flows mainly downward, although some very small upward FAC regions can also be observed. The maximum conductivity enhancement is about 1.01 times of its background value, which gives a maximum Pedersen conductivity of 2.02 mho and a maximum Hall conductivity of 6.06 mho. The conductivity enhancement here is much smaller than that for the duskside driven cases because the FAC flows mainly downward for the dawnside region and no conductivity enhancement in the downward FAC regions based on (3.31) in the present model. Therefore, it may be concluded that there is nearly no enhancement of the ionospheric conductivity. In addition, there is nearly no Hall portion of the FAC, because it is proportional to  $\nabla \Sigma_h$  and  $\Sigma_h$  is nearly constant here. Therefore, the effect of  $R_{hp}$  is negligible for the dawnside driven conditions. Since the enhancement of the ionospheric conductivity is used as the indication of the intensity of auroral activity, it may be concluded that no auroral bright spot can be observed in the pre-noon sector of the ionosphere.

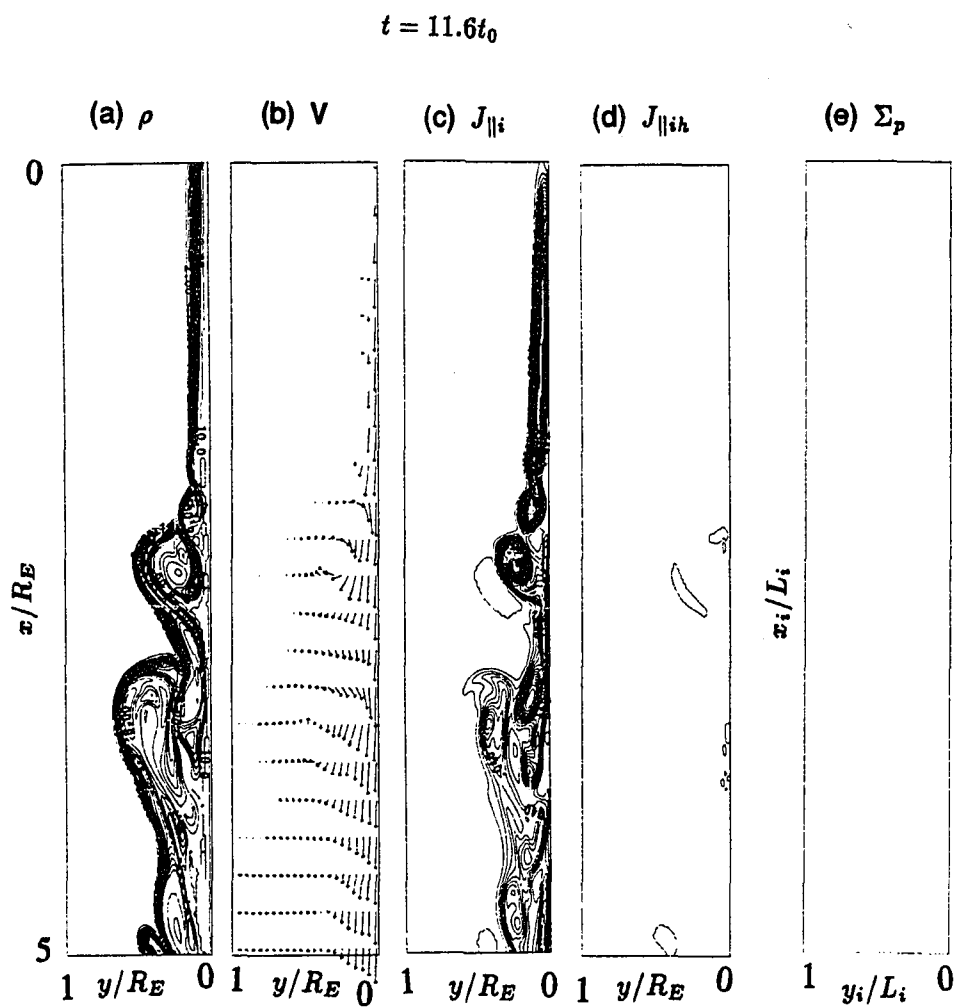


**Figure 3.8** Same as Fig. 3.3, but for a case with the uniform driven condition at the dawnside region of the magnetopause and  $R_{hp} = 3$ .



### 3.4 Summary and Discussion

In this study we have investigated the plasma dynamics in the low-latitude boundary layer and its coupling to the polar ionosphere under driven boundary conditions at the magnetopause. Some features included in this model are: the mass transport across the magnetopause, the divergence of the FAC through the finite conductivity in the ionosphere, the enhancement of the ionospheric conductivity due to the precipitating energetic electrons in the upward FAC regions, a linear current-voltage relationship for the FAC, and the non-periodic boundary conditions in the low-latitude boundary layer. It is found that, in the presence of a driven plasma flow along the magnetopause, the KH instability can develop. This leads to the formation of vortices in the low-latitude boundary layer which will grow to large sizes as they are convected tailward. The vorticity generated in the duskside (dawnside) region of the boundary layer leads to the presence of localized upward (downward) FAC regions along the post-noon (pre-noon) sector in both the northern and the southern polar ionospheres. On the other hand, the finite ionospheric conductivity provides dissipation, which leads to the decay of the plasma vortices. The competing effect of the formation and decay of vortices leads to the formation of strong vortices only in limited regions. Several enhanced conductivity regions which are associated with the boundary layer vortices and the upward FAC regions can be found along the post-noon auroral oval, while the conductivity enhancement in the pre-noon auroral oval is very small. These enhanced conductivity regions along the post-noon auroral oval may account for the observed dayside auroras which show bright features resembling "beads" or "pearls".

In this study, we neglect the Alfvén transit time between the magnetosphere and the ionosphere, which is a valid approximation if the Alfvén transit time is relatively short,

compared with the characteristic time for the vortex formation. In reality, the Alfvén transit time can be on the same order as the growth and decay times. The neglect of the Alfvén transit time leads to an overestimation of the damping effect of the ionosphere to the dynamics in the boundary layer. The background ionospheric Pedersen conductivity used in all of the cases shown in this study is  $\Sigma_{p0} = 2$  mho, which is relatively small. Since the finite ionospheric conductivity provides the damping effect, a small value of the conductivity may compensate some Alfvén waves effect. Some properties of the Alfvén wave propagation will be studied in next chapter.

The principal results obtained by the simulations may be summarized as follows.

(1) In the boundary layer region, the vortex motions associated with the KH instability are observed in the simulation. The plasma flows mainly tailward but small sunward flows are also observed. The plasmas originating from the magnetosheath and the magnetosphere mix in the boundary layer, forming a density plateau at some regions of the boundary layer. The plasma density profiles in the boundary layer have vortex structures. Coalescence of the vortices is also observed. The thickness of the boundary layer increases with increasing longitudinal distance from the subsolar point. These results are similar to those in Chapter 2.

(2) The vortices generated in the duskside (dawnside) region of the boundary layer mainly lead to the presence of localized upward (downward) field-aligned current regions along the post-noon (pre-noon) sector in both the northern and the southern polar ionospheres. Some return field-aligned current regions are also observed. The enhanced FAC regions are limited in space.

(3) The Hall portion of the FAC has paired structures. Each paired structure is coincident with each enhanced FAC region. If the Hall to Pedersen conductivity ratio becomes large ( $R_{hp} \geq 2$ ), the Hall portion of the FAC density may be as large as the total FAC density,

or even larger than the total FAC density. Therefore, the Hall conductivity effect may be significant in some regions. The Hall conductivity effect becomes insignificant at pre-noon sector of the auroral oval because there is nearly no conductivity enhancement.

(4) Several enhanced conductivity regions are observed along the post-noon auroral oval, which are caused by the enhanced localized upward FAC regions. These enhanced conductivity regions represent the auroral bright spots. The convection speed, the scale size, and the separation distance of these auroral bright spots obtained from the numerical simulations are consistent with the observations of the Viking satellite [*Lui et al.*, 1989]. These enhanced conductivity regions (or auroral bright spots) may account for the observed dayside auroras which show bright features resembling "beads" or "pearls" [*Lui et al.*, 1989; *Potemra et al.*, 1990].

## CHAPTER 4

### Evolution of Magnetic Flux Ropes and Plasma Vortices

#### 4.1 Introduction

As studied in the previous chapters, the plasma vortices are generated by the sheared plasma flow in the low-latitude boundary layer. The vortex structures associated with the sheared plasma flow in the LLBL are schematically shown in Figure 4.1. In the figure, "A" is a counterclockwise vortex in the duskside region of the boundary layer, "B" is a clockwise vortex in the dawnside region of the boundary layer, and "C" and "D" are their corresponding footprints in the polar ionosphere. These vortex structures lead to the presence of localized FAC regions, as have been discussed earlier. In Figure 4.1, the FAC inside the vortex "A" is directed upward (from "C" to "A") and the FAC inside the vortex "B" is directed downward (from "B" and "D"). The plasma vortex and the FAC are carried by Alfvén waves propagating between the magnetosphere and the ionosphere.

As mentioned in Chapter 3, the linear current-voltage relationship (3.14) used in the magnetosphere-ionosphere coupling model is a lumped relation. The use of the field-aligned potential drop and this lumped relation eliminates the possibility of describing transit time effects and assumes that the Alfvén transit time between the magnetosphere and the ionosphere is much shorter than the time scale of the evolution of plasma vortices in the boundary layer. In reality, the Alfvén transit time can be comparable to the growth and decay times of the plasma vortices. The neglect of Alfvén transit time leads to an overestimation of the

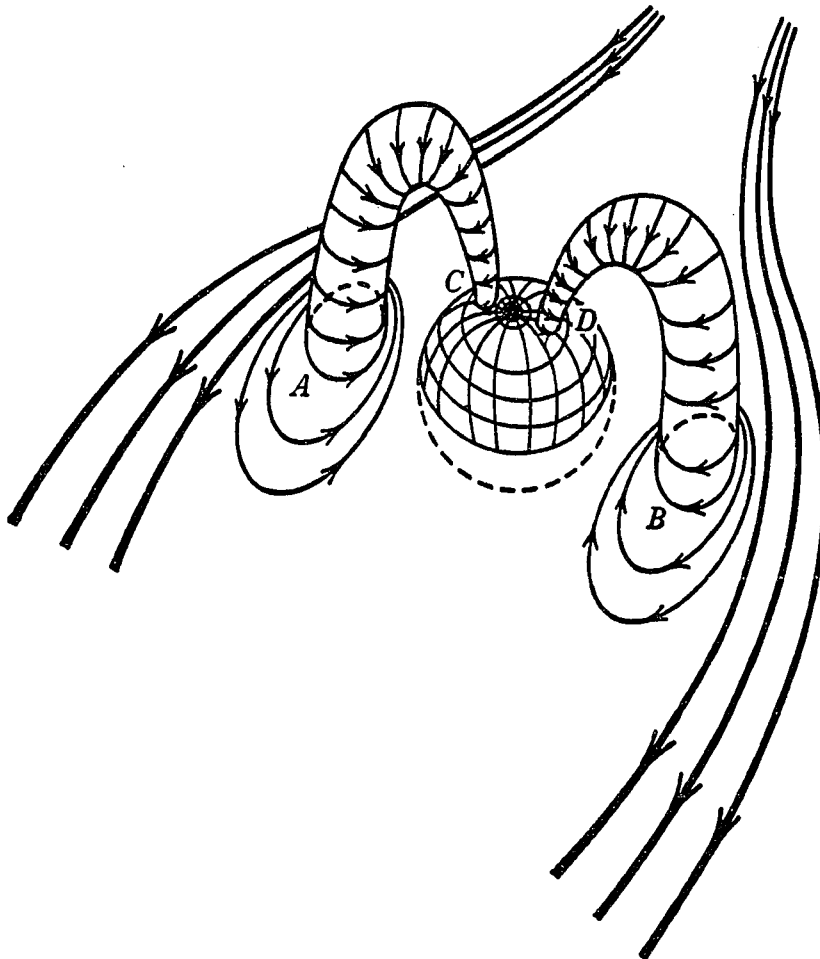


**Figure 4.1** Schematic representation of how boundary layer vortices couple to the polar ionosphere. The velocity difference between the solar wind and the magnetosphere creates vortices "A" and "B" in the boundary layer, which produce footprints "C" and "D" in the polar ionosphere, respectively, along the geomagnetic field lines [Ratcliffe, 1972].

ionospheric damping effect. Field-aligned currents, the major link for the magnetosphere-ionosphere coupling process, are carried by the Alfvén waves propagating between the magnetosphere and the ionosphere. It has been found in the previous chapters that the field-aligned currents can be associated with localized plasma vortices. In addition, similar field-aligned currents can be generated by helical magnetic field structures at the magnetopause [e.g., *Russell and Elphic, 1979; Saunders et al., 1984; Lee, 1986*]. In this chapter, as a first step to include the propagation of the Alfvén waves in the magnetosphere-ionosphere coupling model, we study the generation and propagation of the Alfvén waves from the evolution of plasma vortices. In addition, the evolution of helical magnetic field structures may also generate large-amplitude Alfvén waves. Observations and formation of plasma vortices in the magnetopause-boundary layer region have been discussed in detail in the previous chapters. In the following, observations and formation of helical magnetic field structures at the magnetopause, as well as in other space environments, are presented.

Localized magnetic flux tubes, or magnetic ropes, have been observed in the Venus ionosphere [*Russell et al., 1979a, b; Elphic et al., 1980*], in the solar atmosphere [*Alfvén and Falthammar, 1963; Alfvén, 1981*], in the interplanetary space [*Burlaga et al., 1981; Burlaga, 1984*], at the Earth's dayside magnetopause [*Russell and Elphic, 1979*], and in the Earth's magnetotail [*Sibeck et al., 1984; Elphic et al., 1986*]. The magnetic field in the magnetic rope consists of an axial component and an azimuthal component, leading to the presence of helical magnetic field lines. The current associated with the magnetic field of the helical flux tube is constricted to a cylinder and forms a line current [e.g., *Parker, 1979; Priest, 1990*]. Under certain conditions, the magnetic flux tubes tend to coincide with material filaments that have a higher plasma density than surroundings. The constriction mechanism of helical magnetic flux tubes may explain many filamentary structures observed in the solar corona,

in the interplanetary space, and in the planetary ionosphere or magnetosphere [Alfvén, 1981]. The formation and evolution of helical magnetic flux tubes are an interesting and important problem in the study of cosmic plasmas.

The flux transfer events (FTEs) observed at the Earth's dayside magnetopause by ISEE 1 and 2 satellites [Russell and Elphic, 1979] are evidence of magnetic flux tubes. The properties of FTEs have been further studied and discussed by many researchers [e.g., Paschmann *et al.*, 1982; Saunders *et al.*, 1984; Lee and Fu, 1985; Lee, 1986; Scholer, 1988; Southwood *et al.*, 1988; Papamastorakis *et al.*, 1989] and can be summarized as follows: (1) FTEs have a strong IMF  $B_z$  dependence and are observed to occur every 5 – 15 min with about 2 min duration; (2) The cross section of the FTE flux tube is typically  $1 R_E^2$  at the magnetopause; (3) Twisted magnetic field lines are observed inside the open flux tube at the magnetopause, which indicate the presence of the field-aligned current ( $J_{\parallel}$ ) in the flux tube; (4) Alfvén waves associated with the twisted magnetic field, which carry the field-aligned currents, are observed to propagate along the flux tube toward the magnetosheath and the magnetosphere, and subsequently to the ionosphere and produce footprints of the flux tube in the ionosphere.

The formation of FTE flux tubes at the Earth's dayside magnetopause may be due to the patchy and intermittent reconnection [Russell and Elphic, 1979], the multiple X line reconnection [Lee and Fu, 1985; Lee, 1986], or the bursty single X line reconnection [Southwood *et al.*, 1988; Scholer, 1988]. The twisting of the magnetic field during an FTE is an inherent feature of the multiple X line reconnection model [Lee and Fu, 1985]. On the other hand, the magnetic helicity may also exist in the flux tube formed in the patchy and intermittent reconnection model and in the bursty single X line reconnection model [Wright and Berger, 1989; Song and Lysak, 1989]. The existence of the magnetic helicity or the magnetic field

twist indicates that helical magnetic field lines are present inside the FTE flux tube in which an azimuthal field component is superposed on an axial field component.

Based on the observations of the Pioneer Venus Orbiter, *Russell et al.* [1979a, b] found that in the ionosphere of Venus, discrete magnetic ropes with a diameter of  $\sim 10 - 20$  km and a magnetic field strength of  $\sim 1 - 80$  nT were frequently observed [*Russell et al.*, 1979a, b; *Russell*, 1990]. *Burlaga et al.* [1981] used spacecraft data to identify the presence of magnetic clouds in the interplanetary space, which are magnetic structures with a large rotation of the magnetic field vector [*Burlaga et al.*, 1981; *Klein and Burlaga*, 1982]. The total magnetic and plasma pressure inside the magnetic cloud is observed to be higher than the total pressure outside the magnetic cloud. *Burlaga et al.* [1981] and *Klein and Burlaga* [1982] suggested that a magnetic cloud will expand as it moves away from the Sun as a result of the low external pressure in the solar wind, and the average expansion speed between the Sun and the Earth is estimated to be of the order of half the ambient Alfvén speed. *Klein and Burlaga* [1982] further found that the interplanetary magnetic clouds are usually associated with the coronal mass ejections.

The magnetic ropes are also observed in the Earth's magnetotail [*Sibeck et al.*, 1984; *Elphic et al.*, 1986]. ISEE 1 and 2 observations in the near-Earth magnetotail [*Elphic et al.*, 1986] show the existence of the magnetic ropes with a diameter of  $\sim 4 R_E$  (Earth's radius), which consist of loops of closed magnetic field lines. Plasmoids observed in the magnetotail may also have magnetic rope properties [*Birn et al.*, 1989]. These magnetic ropes in the magnetotail have similar properties as the dayside flux transfer events.

As mentioned in the previous chapters, the sheared plasma flow exists in the low-latitude boundary layer, creating vortex motions. The sheared plasma flow also exists along the magnetospheric tail plasma sheet outer and inner boundaries. The vortex motion associated



with the sheared plasma flow leads to the presence of localized FAC regions, which in turn leads to the presence of an azimuthal component of the magnetic field. When this azimuthal magnetic field adds to the guiding axial magnetic field, a helical magnetic field structure is formed in the region containing the localized FACs. This helical magnetic field structure is similar to the magnetic flux rope mentioned earlier.

The purpose of this chapter is to study the evolution of localized magnetic flux ropes and localized plasma vortices based on a two-dimensional magnetohydrodynamic numerical simulation in the cylindrical coordinates. It will be shown that large-amplitude Alfvén waves are generated by both localized magnetic flux ropes and plasma vortices. These Alfvén waves, carrying FACs, provide the link for the coupling of the helical magnetic field structures and the plasma vortices in the magnetosphere to the ionosphere. The simulation results are then applied to the evolution of magnetic ropes associated with the flux transfer events and the evolution of plasma vortices formed in the magnetopause-boundary layer.

In the simulation study of the astrophysical jets, *Shibata and Uchida* [1985] used the same set of MHD equations and a similar initial configuration of the magnetic field as we use below. But there are several noteworthy differences between their work and the present work. First, their purpose was to study the formation of jets in the astrophysical situation, while we study the evolution of an isolated magnetic rope. Second, their boundary conditions are different from ours. Third, they only studied the initial phase of the evolution. More comparisons will be given as we present our simulation results in the following sections.

## 4.2 Simulation Model

In this section, we present the governing equations, the initial conditions and boundary conditions for an initial helical magnetic field structure. The initial and boundary conditions for a plasma vortex, together with the simulation results, will be presented in section 4.4.

### 4.2.1 Governing Equations

In the present study we use the following compressible MHD equations:

$$\frac{\partial \rho}{\partial t} = -\nabla \cdot (\rho \mathbf{V}) \quad (4.1)$$

$$\frac{\partial}{\partial t}(\rho \mathbf{V}) = -\nabla \cdot \left[ \left( P + \frac{1}{2\mu_0} B^2 \right) \vec{\mathbf{I}} + \rho \mathbf{V} \mathbf{V} - \frac{1}{\mu_0} \mathbf{B} \mathbf{B} \right] \quad (4.2)$$

$$\frac{\partial \varepsilon_T}{\partial t} = -\nabla \cdot \left[ \left( \varepsilon_T + P + \frac{1}{2\mu_0} B^2 \right) \mathbf{V} - \frac{1}{\mu_0} (\mathbf{V} \cdot \mathbf{B}) \mathbf{B} + \frac{\eta}{\mu_0^2} (\nabla \times \mathbf{B}) \times \mathbf{B} \right] \quad (4.3)$$

$$\frac{\partial \mathbf{B}}{\partial t} = \nabla \times (\mathbf{V} \times \mathbf{B}) + \frac{\eta}{\mu_0} \nabla^2 \mathbf{B} \quad (4.4)$$

with

$$\varepsilon_T = \frac{1}{2} \rho \mathbf{V}^2 + \frac{1}{\gamma - 1} P + \frac{1}{2\mu_0} \mathbf{B}^2 \quad (4.5)$$

where  $\rho$  is the plasma mass density,  $\mathbf{V}$  is the plasma velocity,  $P$  is the plasma pressure,  $\mathbf{B}$  is the magnetic field,  $\varepsilon_T$  is the total energy density,  $\gamma$  is the ratio of the specific heats ( $\gamma = 5/3$ ),  $\mu_0$  is the permeability in vacuum,  $\eta$  is the magnetic resistivity, and  $\vec{\mathbf{I}}$  is a unit tensor. For a small value of  $\eta$ , the term  $\nabla \cdot \left[ \left( \eta / \mu_0^2 \right) (\nabla \times \mathbf{B}) \times \mathbf{B} \right]$  in the energy equation (4.3) is small and can be neglected. In order to study the evolution of the magnetic flux rope, we use the cylindrical coordinates  $(r, \theta, z)$  and assume that the spatial structure is cylindrically

symmetric. All variables depend only on the coordinates  $r$  and  $z$ . The two-dimensional compressible MHD equations in the cylindrical coordinates can be written as

$$\frac{\partial \rho}{\partial t} = -\frac{1}{r} \frac{\partial}{\partial r} (r \rho V_r) - \frac{\partial}{\partial z} (\rho V_z) \quad (4.6)$$

$$\begin{aligned} \frac{\partial}{\partial t} (\rho V_r) &= -\frac{\partial}{\partial r} [P + \rho V_r^2 - \frac{1}{2\mu_0} (B_r^2 - B_\theta^2 - B_z^2)] \\ -\frac{\partial}{\partial z} (\rho V_r V_z - \frac{1}{\mu_0} B_r B_z) &- \frac{1}{r} [\rho V_r^2 - \rho V_\theta^2 - \frac{1}{\mu_0} (B_r^2 - B_\theta^2)] \end{aligned} \quad (4.7)$$

$$\begin{aligned} \frac{\partial}{\partial t} (\rho V_\theta) &= -\frac{\partial}{\partial r} (\rho V_r V_\theta - \frac{1}{\mu_0} B_r B_\theta) - \frac{\partial}{\partial z} (\rho V_\theta V_z \\ &- \frac{1}{\mu_0} B_\theta B_z) - \frac{2}{r} (\rho V_r V_\theta - \frac{1}{\mu_0} B_r B_\theta) \end{aligned} \quad (4.8)$$

$$\begin{aligned} \frac{\partial}{\partial t} (\rho V_z) &= -\frac{1}{r} \frac{\partial}{\partial r} [r (\rho V_r V_z - \frac{1}{\mu_0} B_r B_z)] \\ &- \frac{\partial}{\partial z} [P + \rho V_z^2 + \frac{1}{2\mu_0} (B_r^2 + B_\theta^2 - B_z^2)] \end{aligned} \quad (4.9)$$

$$\begin{aligned} \frac{\partial}{\partial t} (\frac{1}{2} \rho \mathbf{V}^2 + \frac{1}{\gamma-1} P + \frac{1}{2\mu_0} \mathbf{B}^2) &= \\ -\frac{1}{r} \frac{\partial}{\partial r} \{ r [(\frac{1}{2} \rho \mathbf{V}^2 + \frac{\gamma}{\gamma-1} P + \frac{1}{\mu_0} \mathbf{B}^2) V_r - (B_r V_r + B_\theta V_\theta + B_z V_z) B_r / \mu_0] \} \\ -\frac{\partial}{\partial z} [(\frac{1}{2} \rho \mathbf{V}^2 + \frac{\gamma}{\gamma-1} P + \frac{1}{\mu_0} \mathbf{B}^2) V_z - (B_r V_r + B_\theta V_\theta + B_z V_z) B_z / \mu_0] \end{aligned} \quad (4.10)$$

$$\frac{\partial B_r}{\partial t} = -\frac{\partial}{\partial z} (V_z B_r - V_r B_z) + \frac{\eta}{\mu_0} (\nabla^2 B_r - \frac{B_r}{r^2}) \quad (4.11)$$

$$\frac{\partial B_\theta}{\partial t} = \frac{\partial}{\partial z} (V_\theta B_z - V_z B_\theta) - \frac{\partial}{\partial r} (V_r B_\theta - V_\theta B_r) + \frac{\eta}{\mu_0} (\nabla^2 B_\theta - \frac{B_\theta}{r^2}) \quad (4.12)$$

$$\frac{\partial B_z}{\partial t} = \frac{1}{r} \frac{\partial}{\partial r} [r (V_z B_r - V_r B_z)] + \frac{\eta}{\mu_0} \nabla^2 B_z \quad (4.13)$$

where  $V_r$ ,  $V_\theta$  and  $V_z$  are the three components of velocity  $\mathbf{V}$ , and  $B_r$ ,  $B_\theta$  and  $B_z$  are the magnetic field components.

### 4.2.2 Initial Conditions and Normalization

The initial configuration of the localized helical magnetic field structure consists of a localized azimuthal field superposed on a uniform axial field. The field components are given by

$$\begin{aligned}
 B_r &= 0 \\
 B_\theta &= \begin{cases} B_{\theta 0}(r/a) \exp(-r^2/a^2) \operatorname{erf}[(z_0 - |z|)/b] & \text{if } |z| \leq z_0 \\ 0 & \text{otherwise} \end{cases} \quad (4.14) \\
 B_z &= B_0
 \end{aligned}$$

where  $B_{\theta 0}$  is a constant,  $a$  is the initial radius of the flux tube,  $2z_0$  is the initial length of the flux tube,  $b$  is the transition width at the two ends of the flux tube, and  $\operatorname{erf}(x)$  is the error function. The initial velocity is assumed to be zero. Let the plasma density and pressure outside the flux tube be  $\rho_0$  and  $P_0$ , respectively. Also define  $\beta = P_0/(B_0^2/2\mu_0)$  as the ratio of the plasma pressure to the magnetic pressure.

In numerical computations the physical variables are normalized by the following quantities: length by a characteristic length,  $a$ ; density by the initial background density,  $\rho_0$ ; magnetic field by  $B_0$ ; velocity by the Alfvén velocity,  $V_A = B_0/(\mu_0\rho_0)^{1/2}$ ; time by the Alfvén transit time,  $t_A = a/V_A$ ; and pressures (both plasma pressure and magnetic pressure) by  $B_0^2/2\mu_0$ . Let the magnetic Reynolds number be  $R_m = \mu_0 V_A a/\eta$ , where  $\eta$  is the magnetic resistivity. The magnetic Reynolds number is taken to be  $R_m \simeq 100 - 500$  in numerical simulations and is different for different cases. Equations (4.6)–(4.13) are solved numerically based on a centered differencing scheme in space and the fourth-order Runge-Kutta time stepping scheme.

### 4.2.3 Simulation Box and Boundary Conditions

The simulations are carried out with  $101 \times 201$  grid points inside a box surrounded by four sides:  $0 \leq r \leq R$ ,  $0 \leq z \leq L$ , where the length along the  $r$ -direction (horizontal) is  $R = 8 a$  and the length along the  $z$ -direction (vertical) is  $L = 16 a$ .

The boundary conditions at  $r = 0$  can be obtained from the criterion that the physical quantities at  $r = 0$  are single-valued, finite, and continuous. From the single value condition at  $r = 0$ , we obtain

$$B_\theta = 0 \quad V_\theta = 0 \quad (4.15)$$

From  $\nabla \cdot \mathbf{B} = B_r/r + \partial B_r/\partial r + \partial B_z/\partial z = 0$ , and finite value condition at  $r = 0$ , we have

$$B_r = 0 \quad (4.16)$$

Similarly, since  $B_z$  is allowed to be nonzero at  $r = 0$ , we obtain from (4.13)

$$V_r = 0 \quad (4.17)$$

The following results may be obtained from the momentum and energy equations under the continuity condition at  $r = 0$

$$\frac{\partial \rho}{\partial r} = \frac{\partial \varepsilon_T}{\partial r} = \frac{\partial B_z}{\partial r} = \frac{\partial V_z}{\partial r} = 0 \quad (4.18)$$

At  $z = 0$ , a symmetric or antisymmetric boundary condition is used for each physical quantity to ensure that the wave propagating along the negative  $z$ -direction is exactly the same as the wave propagating along the positive  $z$ -direction. From the analysis of the basic equations with the given initial conditions, we find that  $\rho$ ,  $\varepsilon_T$ ,  $V_r$ ,  $B_\theta$ , and  $B_z$  are symmetric

about  $z = 0$ , while  $V_\theta$ ,  $V_z$  and  $B_r$  are antisymmetric about  $z = 0$ . Therefore, the boundary conditions at  $z = 0$  are

$$\frac{\partial \rho}{\partial z} = \frac{\partial \varepsilon_T}{\partial z} = \frac{\partial V_r}{\partial z} = \frac{\partial B_\theta}{\partial z} = \frac{\partial B_z}{\partial z} = 0 \quad (4.19)$$

$$V_\theta = V_z = B_r = 0 \quad (4.20)$$

Because of these symmetry properties, the numerical simulation is carried out only in the region with  $z \geq 0$ . We have simulated a case with  $-16a \leq z \leq 16a$ , and found that the boundary conditions in (4.19) and (4.20) are indeed the corrected ones for an initially helical magnetic field structure.

Note that in *Shibata and Uchida's* [1985] paper, the boundary conditions at  $z = 0$  are  $\partial f / \partial z = 0$  for any physical quantity  $f$ . Their boundary conditions are different from ours in (4.19) and (4.20). In their simulations the helical magnetic flux tubes cannot be separated into two tubes due to their assumed boundary conditions, which are not applicable for the evolution of an isolated flux tube as in the present study.

At  $z = L = 16a$ , the following boundary conditions are used:

$$\frac{\partial \rho}{\partial z} = \frac{\partial \varepsilon_T}{\partial z} = \frac{\partial V}{\partial z} = \frac{\partial B}{\partial z} = 0 \quad (4.21)$$

A damping zone is set up in the region  $0.9R \leq r \leq R$  to damp waves propagating toward or reflecting from the boundary  $r = R = 8a$ . In this zone a larger resistivity is used in (4.11)–(4.13).

### 4.3 Evolution of Magnetic Flux Tubes

Magnetic flux tubes may have different ratio of the azimuthal field to the axial field ( $B_\theta/B_z = B_\theta/B_0$ ). In addition, due to different formation mechanisms, the length-radius ratio of the magnetic flux tube,  $z_0/a$ , may also be different. To study the general evolution of the magnetic flux tubes, we present simulation results with different values of  $B_\theta/B_0$  and  $z_0/a$ . In Case A the magnetic flux tube with an initial value of  $B_{\theta\max}/B_0 \simeq 1$  is studied, while in Case B the magnetic flux tube with a large  $B_\theta/B_0$  is studied. Finally, we present some simulation results with different ratios of  $z_0/a$  and  $B_\theta/B_0$ .

#### 4.3.1 Case A: A Small $B_\theta/B_0$ Ratio

In Case A we choose  $z_0 = 3a$ ,  $b = a$ ,  $B_{\theta 0} = 2.33 B_0$ , and  $\beta = 1$ . The corresponding maximum initial azimuthal magnetic field at  $t = 0$  is  $B_{\theta\max} = B_0$ . This initial  $B_\theta$  is limited to a small region with  $0 \leq r \leq 2a$  and  $0 \leq z \leq z_0$ . The initial plasma density and pressure are assumed to be uniform inside and outside the flux tube.

Figure 4.2 (from top panel to bottom panel) shows contour plots of the plasma density,  $\rho$ , the azimuthal magnetic field,  $B_\theta$ , the azimuthal velocity,  $V_\theta$ , the plasma pressure,  $P$ , and the magnetic pressure,  $B^2/2\mu_0$ , at different simulation times. Because initially the velocity is assumed to be zero, the plasma density and pressure are uniform, and the magnetic flux rope is not a force-free tube, the existence of the helical magnetic field leads to an imbalance of the total force in the tube, which leads to the contraction or expansion of the helical flux tube and the presence of MHD waves along both the  $r$ -direction and the  $z$ -direction.

From Figure 4.2 it can be seen that at the earlier times ( $t = 1.66 t_A$  and  $t = 5.16 t_A$ ), a wave mode is propagating at a high speed in all directions (see contours of the plasma density,

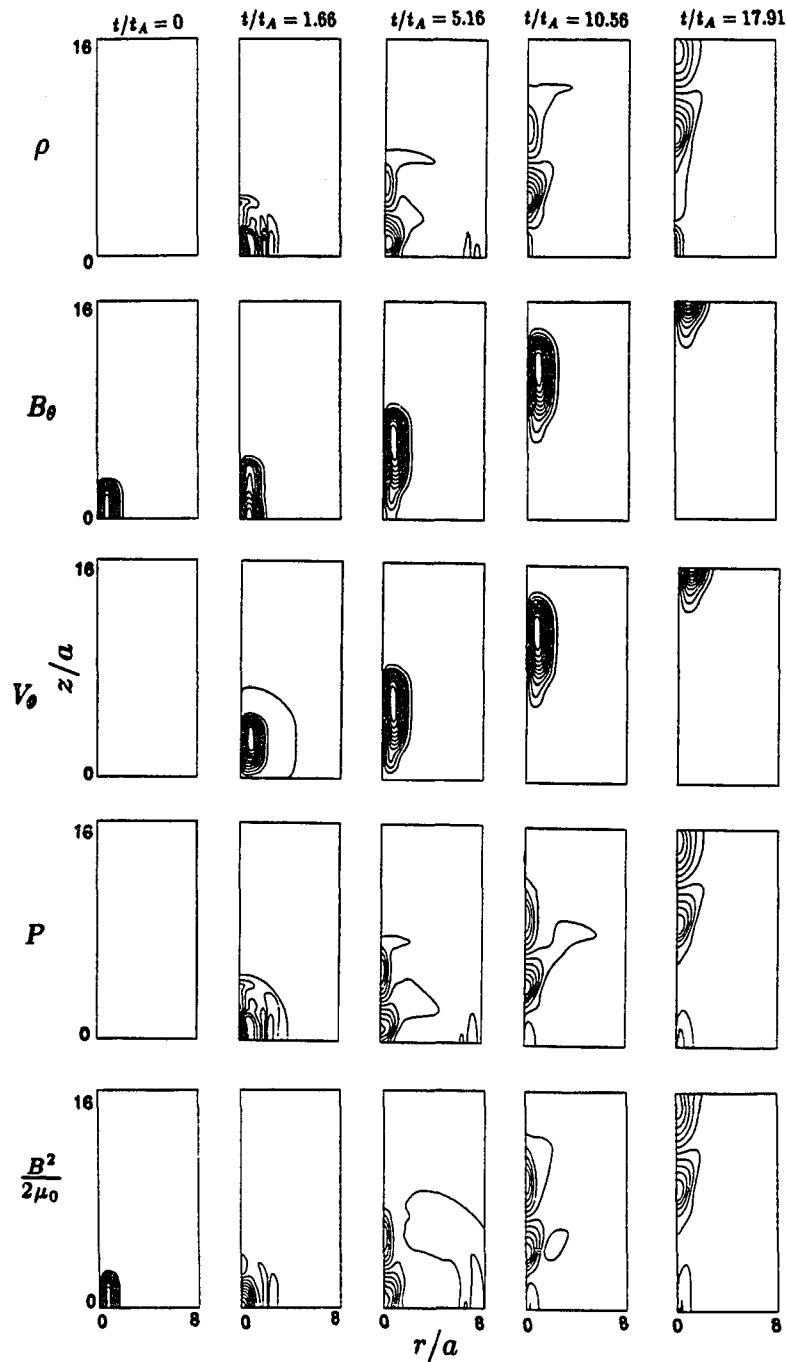


**Figure 4.2** From top panel to bottom panel, contour plots of the plasma density, the azimuthal magnetic field, the azimuthal velocity, the plasma pressure, and the magnetic pressure in Case A at various simulation times. The parameters used are  $B_{\theta\max}(t=0) = B_0$ ,  $z_0 = 3a$ ,  $b = a$ , and  $\beta = 1$ .



the plasma pressure, and the magnetic pressure). A careful calculation (see discussion later) of the propagation speed indicates that such a wave mode is the fast magnetosonic mode. It can be seen from Figure 4.2 that the fast mode has reached the boundary  $r = 8 a$  at  $t = 5.16 t_A$ . At  $t = 10.56 t_A$  as shown in Figure 4.2, the fast mode has propagated out of the simulation domain in the  $r$ -direction, but it is still inside the simulation domain in the  $z$ -direction. At  $t = 17.91 t_A$ , the wave front of the fast mode has propagated out of the entire simulation domain.

The  $B_\theta$  and  $V_\theta$  contours in the second and the third panels of Figure 4.2 have very similar patterns after an initial phase. These profiles are quite different from the density and the pressure profiles in Figure 4.2. The azimuthal magnetic field structure first expands along the  $z$ -direction to about twice its initial length and separates into two parts, one in the positive  $z$ -direction and another in the negative  $z$ -direction (see Figure 4.2 at  $t = 0$  and  $t = 5.16 t_A$  for the  $z > 0$  part). The expansion velocity of the azimuthal magnetic field structure along the  $z$ -axis is found to be the Alfvén velocity ( $V_A$ ) and the radial expansion speed is found to be very small and negligible. As time progresses, the amplitude of  $V_\theta$  increases and the amplitude of  $B_\theta$  decreases. The maximum values of  $B_\theta$  and  $|V_\theta|$  are located at nearly the same radial distance ( $r \simeq 0.8 a$ ) and the radial profiles of  $B_\theta$  and  $|V_\theta|$  are similar to the form of the function  $(r/a)\exp(-r^2/a^2)$ , which is the initial form of  $B_\theta$  along the  $r$ -direction. After some initial transitions ( $t \geq 6 t_A$ ),  $B_\theta$  and  $|V_\theta|$  are found to have the same contour profiles as shown in Figure 4.2. In fact, we find that  $V_\theta/V_A = -B_\theta/B_0$  for the region with  $z > 0$  and  $V_\theta/V_A = B_\theta/B_0$  for the region with  $z < 0$ . This property indicates the presence of the Alfvén wave propagating along the  $z$ -direction.

From above analysis, it may be concluded that the fast magnetosonic mode and the Alfvén mode coexist at an initial time. After this initial phase, the fast wave mode is

separated from the Alfvén wave mode and the dominant wave associated with the flux tube becomes the Alfvén wave, which propagates along the  $z$ -direction with the Alfvén velocity  $V_A$ .

In Case A the initial pressure gradient force ( $-\nabla P$ ) is zero and the total force along the  $r$ -direction is the Lorentz force, which consists of the magnetic gradient force  $-\nabla(B^2/2\mu_0)$  and the tension force  $\mathbf{B} \cdot \nabla \mathbf{B}/\mu_0$ . The Lorentz force may be calculated from the initial magnetic field configuration, which is given by equation (4.14). For the region with  $|z| \ll z_0$ ,  $\text{erf}[(z_0 - |z|)/b] \simeq 1$  and  $B_\theta = B_\theta(r)$ , the Lorentz force is given as

$$F_r = \frac{1}{\mu_0} [(\nabla \times \mathbf{B}) \times \mathbf{B}] \cdot \hat{\mathbf{r}} = -\frac{2B_{\theta 0}r}{\mu_0 a^2} \left(1 - \frac{r^2}{a^2}\right) \exp\left(-\frac{2r^2}{a^2}\right) \quad (4.22)$$

It can be seen that  $F_r$  is negative in the inner region with  $r < a$ . The negative  $F_r$  leads to an inward pinch of the flux tube, which causes the near-axis enhancement of the plasma density, the plasma pressure, and the magnetic field. The force  $F_r$  in the outer part ( $r > a$ ) is positive and causes an outward compression. Near the region  $z \sim z_0$ , it can be shown numerically that the Lorentz force  $F_z$  is positive and it also causes an outward compression along the  $z$ -direction. It is the initial imbalance of force that produces the fast magnetosonic wave.

The time evolution of the fast magnetosonic wave at the initial phase is illustrated in Figure 4.3, which shows the pressure variations along the  $r$ -direction at  $z = 0$ . The plasma pressure is uniform at  $t = 0$ . Due to the inward pinch effect, the plasma pressure is greatly enhanced in the inner region ( $r \leq 0.8a$ ), as shown at  $t = 1.66 t_A$  in Figure 4.3. A region with low density and low pressure is generated near  $r \simeq a$  as a consequence of the initial inward force at  $r < a$  and the outward force at  $r > a$ . At  $t = 3.41 t_A$ , the reflection of the inward compression wave at  $r = 0$  causes the presence of a rarefaction region in the near-axis

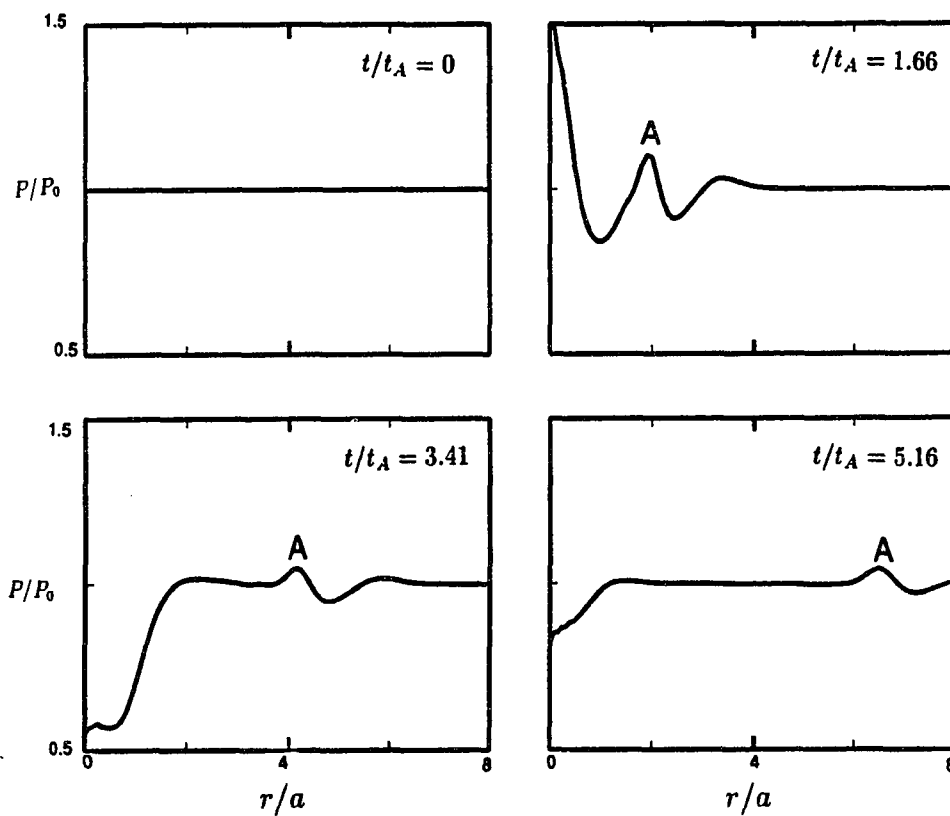


**Figure 4.3** Profiles of the plasma pressure ( $P$ ) along the radial direction at  $z = 0$  in Case A at simulation times  $t/t_A = 0, 1.66, 3.41,$  and  $5.16$ . Mark "A" indicates a wave front of the fast mode wave.

part. As time goes on, the rarefaction effect is reduced, as can be seen from Figure 4.3 at  $t = 5.16 t_A$ . In Figure 4.3, a wave front, as marked with "A," occurs at  $r/a \simeq 1.84, 4.16,$  and  $6.56$  for  $t/t_A = 1.66, 3.41,$  and  $5.16,$  respectively. Therefore, the propagation velocity along the  $r$ -direction for this wave is  $V_f/V_A = \Delta r/\Delta t \simeq 4.72/3.50 \simeq 1.35$ . Theoretically, the propagation velocity of the fast magnetosonic wave along the radial direction is  $V_f = (V_A^2 + C_s^2)^{1/2}$ , where  $C_s = (\gamma P_0/\rho_0)^{1/2}$  is the sound speed. Using  $\gamma = 5/3$  and  $\beta = 1$ , we obtain  $V_f \simeq 1.35 V_A$ . Therefore, the numerical value of the propagation speed agrees very well with the theoretical value of the propagation speed for the fast magnetosonic wave.

To study the propagation velocity of the Alfvén wave, Figure 4.4 shows the wave front position along the  $z$ -direction calculated from the configuration of  $V_\theta$  (Figure 4.4a), the corresponding velocity of the wave front along the  $z$ -direction (Figure 4.4b), and the maximum values of  $B_\theta$  and  $|V_\theta|$  as a function of the simulation time (Figure 4.4c). The wave front is defined as the position where the amplitude of  $|V_\theta|$  is 10% of its maximum value. It can be seen from Figure 4.4a that the wave front position is approximately a straight line. The wave front reaches the boundary  $z = 16a$  at about  $t = 12.6 t_A$ . It can be seen from Figure 4.4b that the wave propagates at nearly a constant velocity along the  $z$ -direction except for some small oscillations at the early time ( $t \leq 2 t_A$ ) due to the presence of the fast mode wave. After this initial phase, the propagation velocity along the  $z$ -direction is  $V_A$ , which is the Alfvén velocity based on the axial magnetic field. This also indicates that the wave mode is the Alfvén mode. It can be seen from Figure 4.4c that  $B_{\theta\max}$  first decreases and then increases due to the initial expansion and pinch of the flux tube. After the initial stage,  $B_{\theta\max}$  decreases monotonically and reaches a constant value. Also shown in Figure 4.4c is the time variation of  $|V_\theta|_{\max}$ . As time goes on,  $|V_\theta|_{\max}$  increases from zero and then also approaches a constant. The asymptotic value is  $|V_\theta|_{\max}/V_A = B_{\theta\max}/B_0 \simeq 0.35$ .

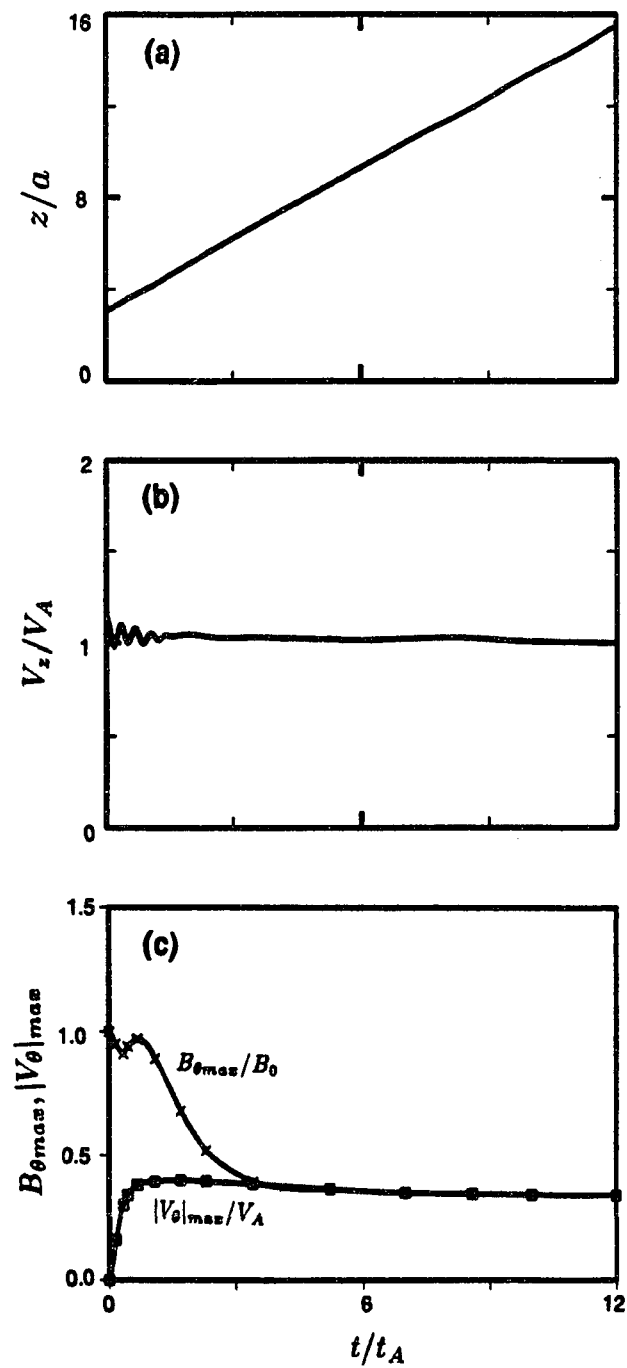


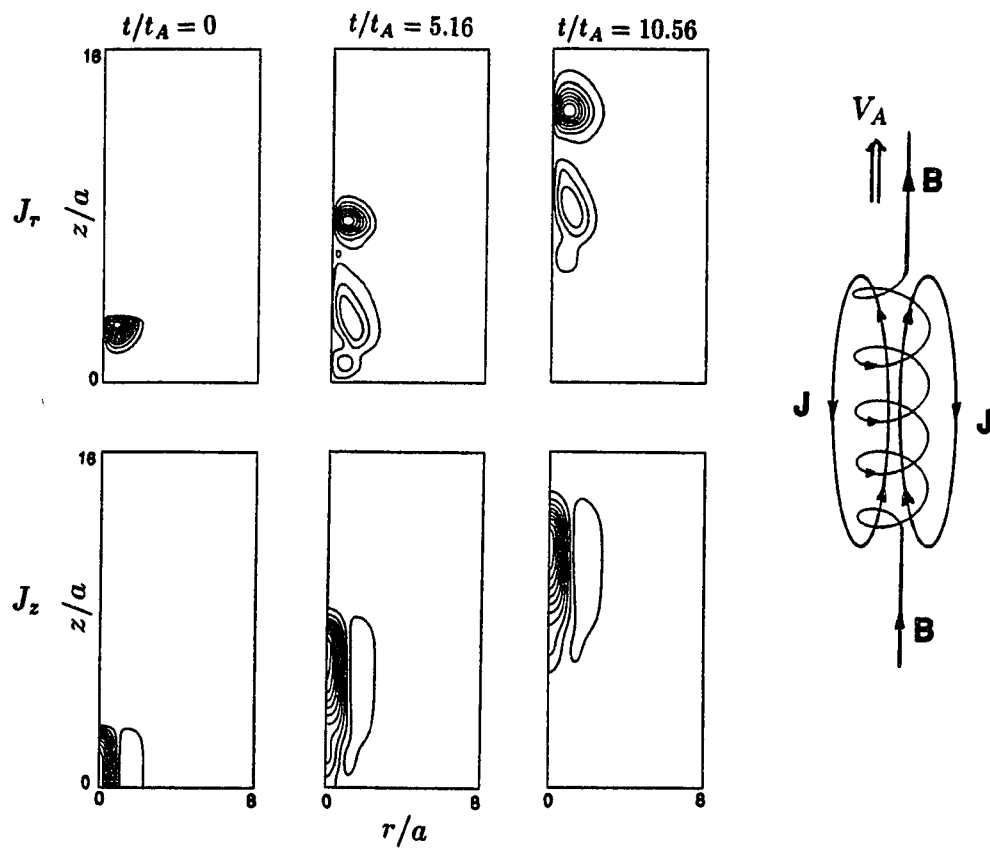
**Figure 4.4** (a) Wave front position along the  $z$ -direction, (b) the corresponding wave front velocity, and (c) the maximum values of  $B_{\theta}$  and  $|V_{\theta}|$  in Case A.

After some initial oscillations, the radial expansion velocity of the flux tube is found to be very small ( $\sim 0.03 V_A$ ). This small radial velocity is in fact caused by the numerical diffusion effect. The radial velocity is found to become smaller when more grid points are used in the simulations.

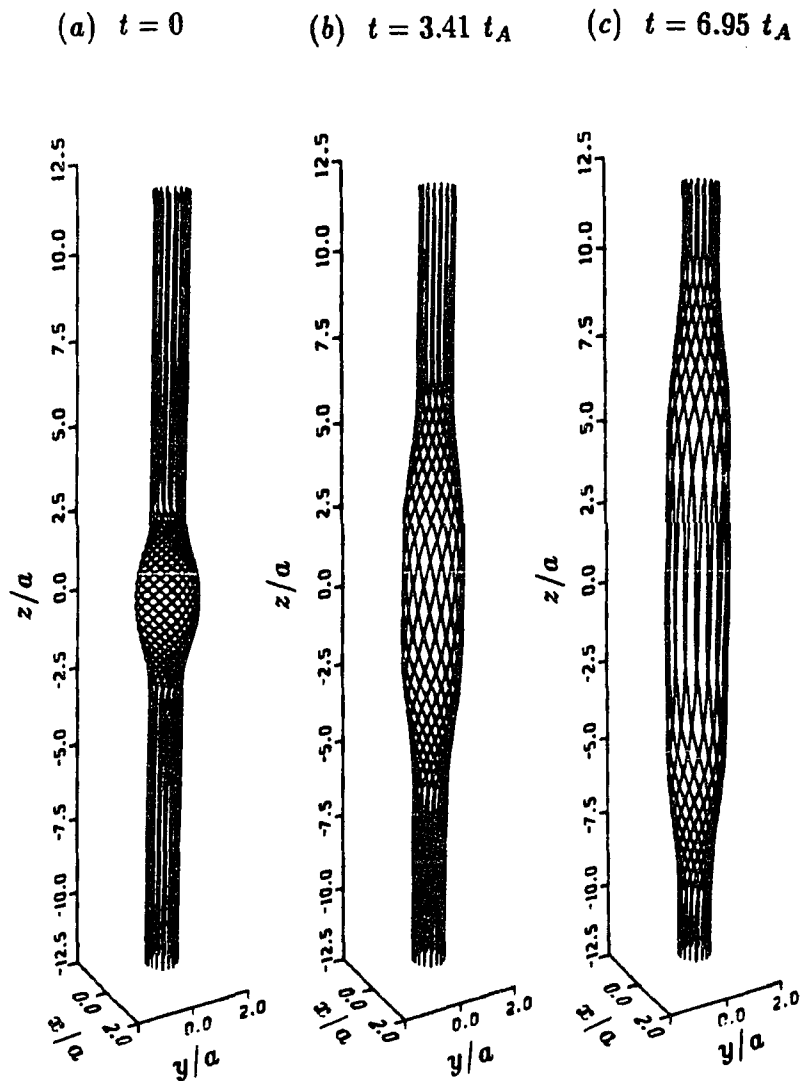
Initially, the transverse kinetic energy is zero and the total energy is in the form of the magnetic energy. As time goes on, the transverse kinetic energy increases and the transverse magnetic energy decreases. The diagnosis shows that after an initial time the transverse kinetic energy tends to have the same magnitude as that of the transverse magnetic energy.

Figure 4.5 shows contour plots of currents along the  $r$ -direction ( $J_r$ ) (top panel) and along the  $z$ -direction ( $J_z$ ) (bottom panel) at different simulation times. It can be seen that the radial current ( $J_r$ ) is mainly located at the wave front along the  $z$ -direction. The current along the  $z$ -direction ( $J_z$ ) flows along the positive  $z$ -direction in the inner region ( $r < a$ ) and the return current ( $J_z < 0$ ) flows in the outer part ( $r > a$ ). We have also checked that at a specific  $z$  the integrated value of the  $J_z$  over the entire plane with a constant  $z$  is zero, as expected from the current closure relation. A schematic closed path of the current and the helical magnetic field lines are shown on the right side of Figure 4.5.

Based on the simulation results in Case A, the magnetic field lines of the flux tube may be drawn, as shown in Figure 4.6. At each time, sixteen field lines are traced and plotted. Figure 4.6a shows the magnetic field lines at  $t = 0$ , namely, the initial helical magnetic field lines. The center of the flux tube is located at  $z = 0$  and the total length of the region with a nonzero azimuthal field is  $\sim 6 a$ . It can be seen that at both ends of the flux tube, the magnetic field lines are straight. Figure 4.6b shows the magnetic field lines at  $t = 3.41 t_A$ . The helical magnetic field structure expands toward both the positive and the negative  $z$ -directions. The length of the part of the flux tube with helical fields is  $\sim 12 a$ , namely,



**Figure 4.5** Contour plots of the currents (top) along the  $r$ -direction ( $J_r$ ) and (bottom) along the  $z$ -direction ( $J_z$ ) in Case A at different simulation times. A schematic sketch of the closed paths of the current and the helical magnetic field lines is also shown.



**Figure 4.6** The magnetic field lines in Case A at different simulation times. (a)  $t = 0$ , (b)  $t = 3.41 t_A$ , and (c)  $t = 6.95 t_A$ . Sixteen magnetic field lines are traced and plotted.



twice of the length of the initial helical tube. The magnitude of  $B_{\theta_{\max}}$  is about 39% of its initial value ( $B_{\theta_{\max}} \simeq 0.39 B_0$ ). The small value of  $B_{\theta_{\max}}$  leads to a looser helical structure of field lines. Figure 4.6c shows the magnetic field lines at  $t = 6.95 t_A$ . At this time the initial magnetic rope has evolved into two separated regions, propagating in opposite direction each with a speed of  $V_A$ . The magnitude of  $B_{\theta_{\max}}$  is found to be  $\sim 0.35 B_0$ .

#### 4.3.2 Case B: A Large $B_\theta/B_0$ Ratio

In Case B we choose  $z_0 = 3 a$ ,  $b = a$ , and  $B_{\theta 0} \simeq 7 B_0$ . The maximum initial azimuthal magnetic field  $B_{\theta_{\max}}(t = 0)$  corresponds to  $3 B_0$ , where  $B_0$  is the initial axial magnetic field. Other conditions are the same as those used in Case A. Because of the large azimuthal magnetic field component,  $B_{\theta_{\max}}(t = 0) = 3 B_0$ , the Lorentz force here is 3 times of the force in Case A. Therefore, the total force becomes more negative in the inner region of the flux tube and the pinch effect is also largely enhanced.

Figure 4.7 shows contour plots of the azimuthal magnetic field,  $B_\theta$  (top panel), and the azimuthal velocity,  $V_\theta$  (bottom panel), at different simulation times. The configurations of  $B_\theta$  and  $V_\theta$  are quite different from those in Case A shown in Figure 4.2. First, the large pinch effect in the inner region (the small  $r$  region) causes large enhancement of  $B_\theta$  and  $V_\theta$  there. This feature can be seen from the spatial profiles of the plasma density, the plasma pressure, and the magnetic pressure (not shown). On the other hand, the pinch effect in Case A is relatively small. Second, it can be seen that the contour profiles of  $B_\theta$  and  $V_\theta$  become nearly identical at about  $t = 10.56 t_A$ . On the other hand, the contour profiles of  $B_\theta$  and  $V_\theta$  in Case A shown in Figure 4.2 become nearly identical at about  $t = 5.16 t_A$ . This means that it takes a longer time to have  $V_\theta/V_A = -B_\theta/B_0$  in Case B than in Case A. Third, the

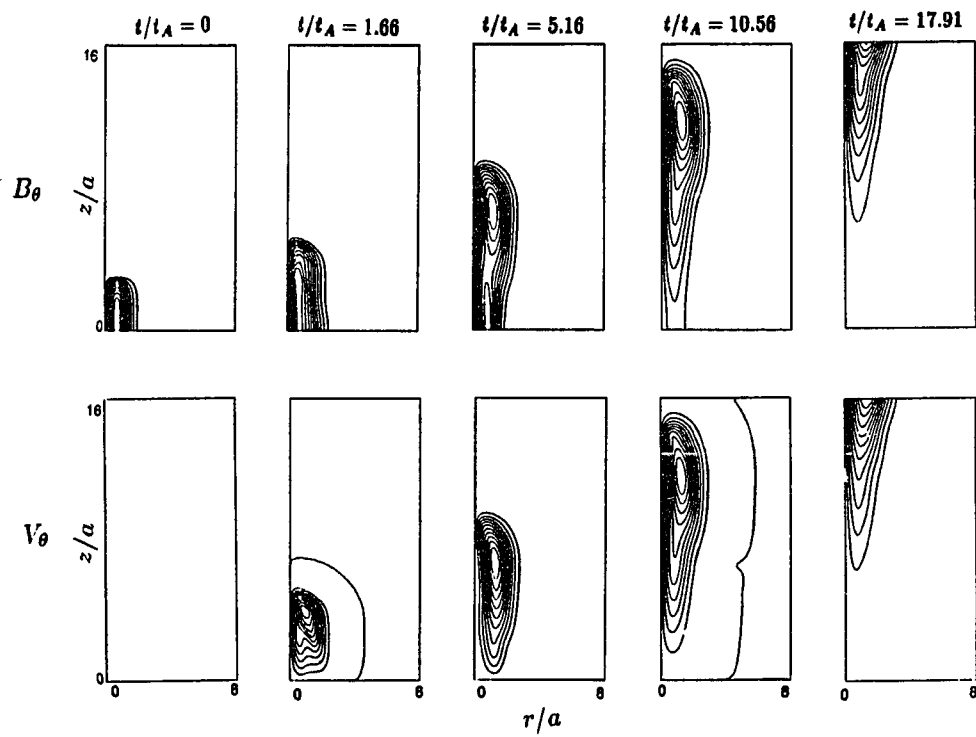


**Figure 4.7** (Top) Contour plots of the azimuthal magnetic field,  $B_\theta$ , and (bottom) the azimuthal velocity,  $V_\theta$ , in Case B at different simulation times. The parameters used in Case B are  $B_{\theta\max}(t=0) = 3 B_0$ ,  $z_0 = 3 a$ ,  $b = a$ , and  $\beta = 1$ .

most distinguished feature here is that along the  $z$ -direction the contour profiles of both  $B_\theta$  and  $V_\theta$  have a very long tail probably due to the enhanced pinch effect. Consequently, the magnetic flux tube is longer than that in Case A, although initially the tube lengths in both cases are the same.

Figure 4.8a shows the velocity of the wave front calculated from the configuration of  $V_\theta$  along the  $z$ -direction, and Figure 4.8b shows the maximum values of  $B_\theta$  and  $|V_\theta|$  as a function of the simulation time. It can be seen from Figure 4.8a that in the initial phase the velocity of the wave front is larger than the Alfvén velocity and shows some oscillations. This is due to the fact that both the fast magnetosonic wave and the Alfvén wave are developed in the flux tube in the initial phase. After this initial phase, the propagation speed of the wave front along the  $z$ -direction is the Alfvén velocity ( $V_A$ ) even for the large  $B_\theta$  in this case. Therefore, after the initial phase, the Alfvén wave becomes the dominant wave mode for the evolution of the flux tube. It is also found that the radial expansion velocity of the flux tube is very small. It can be seen from Figure 4.8b that  $B_{\theta\max}$  is enhanced to about  $4.24 B_0$  at  $t = 0.24 t_A$  due to the pinch of the flux tube in the inner region ( $r < a$ ). As time proceeds, the pinch effect is reduced and  $B_{\theta\max}$  decreases. Also shown in Figure 4.8b is the time variation of  $|V_\theta|_{\max}$ . As time goes on,  $|V_\theta|_{\max}$  increases from zero and then decreases. Finally,  $|V_\theta|_{\max}/V_A$  approaches the same magnitude as that of  $B_{\theta\max}/B_0$ .

### 4.3.3 Effect of Tube Length on the Evolution of the Magnetic Field

As the initial tube length increases, it will take a longer time for the magnetic ropes to evolve into two separated regions of helical field lines. As a comparison study, we run several cases with different  $z_0$ , where  $z_0$  is the initial length of the magnetic flux tube along the

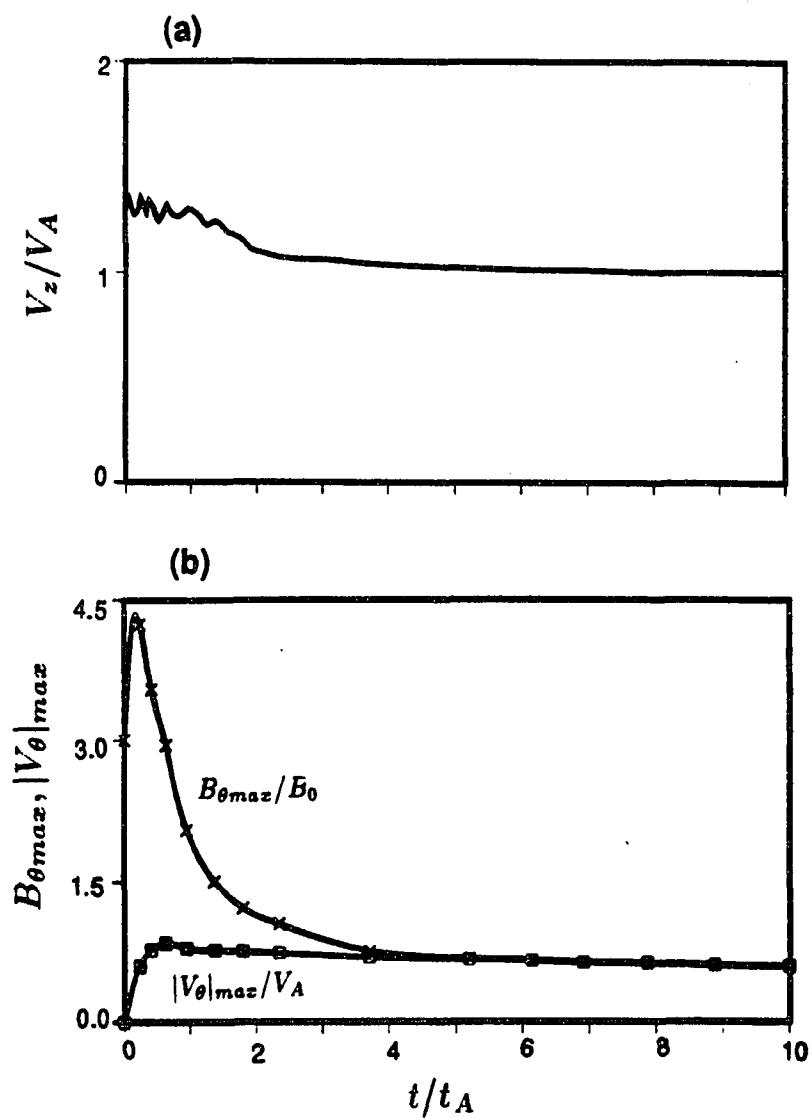
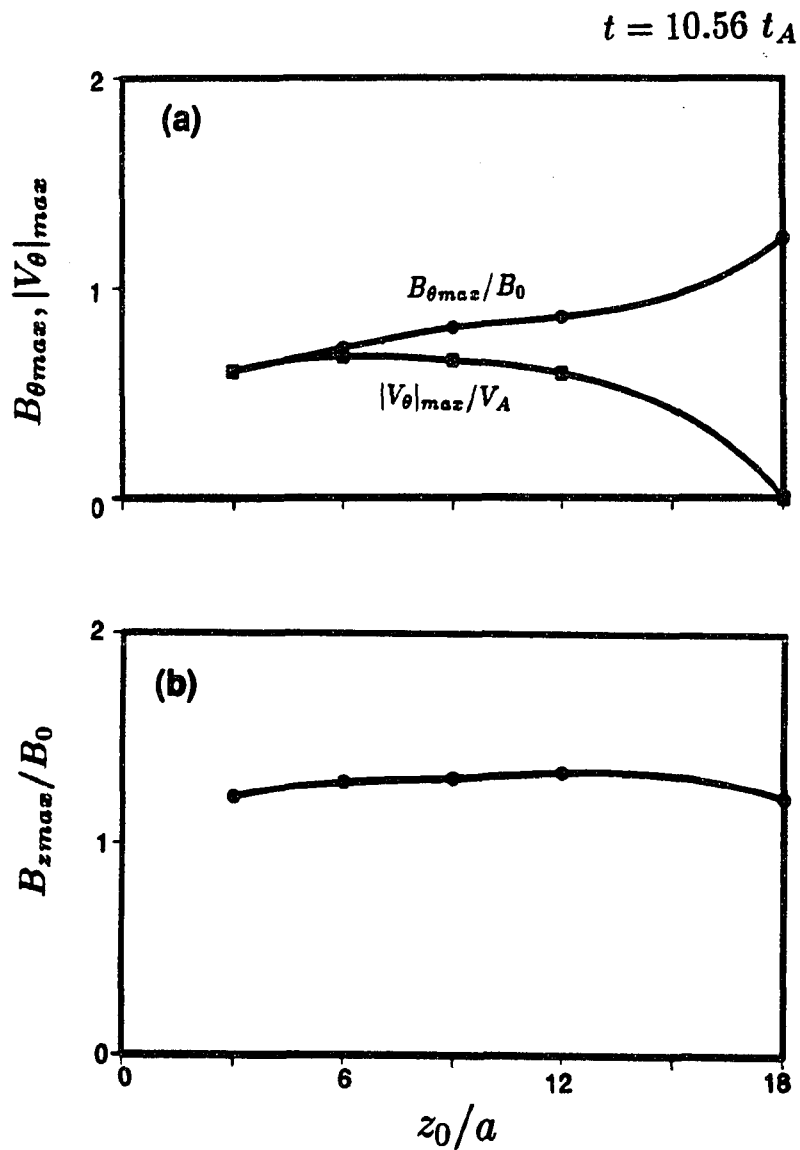


Figure 4.8 (a) The propagation speed of the wave front along the  $z$ -direction and (b) the maximum values of  $B_{\theta}$  and  $|V_{\theta}|$  in Case B.

positive  $z$ -direction. In these cases we set  $b = a$ ,  $\beta = 1$ , and  $B_{\theta 0} \simeq 7 B_0$ . The corresponding maximum initial azimuthal magnetic field at  $t = 0$  is  $B_{\theta \max} = 3 B_0$ . Figure 4.9a shows the maximum values of the azimuthal magnetic field  $B_{\theta}$  and the azimuthal velocity  $|V_{\theta}|$  as a function of  $z_0$ . The data are recorded at  $t = 10.56 t_A$ . It can be seen from Figure 4.9a that  $B_{\theta \max}$  increases as  $z_0$  increases. When  $z_0 \rightarrow \infty$ , namely, the one-dimensional case, the simulation result gives  $B_{\theta \max} = 1.24 B_0$ , which is a very large azimuthal magnetic field component. In the actual computation, because the simulation length along the  $z$ -direction is  $L_z = 16 a$ , it will suffice to set  $z_0 = 18 a$  for the case  $z_0 \rightarrow \infty$  (refer equation (4.14)), as we have done here. From the  $|V_{\theta}|_{\max}$  curve, it can be seen that as  $z_0$  increases  $|V_{\theta}|_{\max}$  first increases and then decreases. For the one-dimensional case ( $z_0 \rightarrow \infty$ ),  $|V_{\theta}|_{\max} = 0$ . This study indicates that as the initial length  $z_0$  increases it will take a longer time to reach the asymptotic state, in which  $V_{\theta}/V_A = \pm B_{\theta}/B_0$ . In the one-dimensional case, which corresponds to an infinitely long flux tube, the magnetic flux rope cannot evolve into two separated regions and no Alfvén wave can be detected. The cases with a short tube length and a small azimuthal magnetic field component are similar to the FTEs at the magnetopause, while the cases with a long tube length and a large azimuthal magnetic field component are similar to the magnetic clouds in the interplanetary space. Because of the large azimuthal magnetic field component in the one-dimensional case, the helical magnetic flux tube structure is tighter than that with a finite  $z_0$ .

Figure 4.9b shows the corresponding maximum value of the axial magnetic field,  $B_{z \max}$ , as a function of  $z_0$ . The maximum values are also recorded at  $t = 10.56 t_A$ . The initial axial magnetic field is  $B_0$  everywhere in the simulation domain. As simulation starts, the axial magnetic field can be enhanced to 7 – 8 times of its initial value in a very short time because of the large pinch effect. As the simulation proceeds, the maximum value of the



**Figure 4.9** (a)  $B_{\theta_{max}}$  and  $|V_{\theta}|_{max}$  values and (b)  $B_{z_{max}}$  values for different flux tube lengths with  $B_{\theta_{max}}(t=0) = 3 B_0$ . Other parameters are  $b = a$  and  $\beta = 1$ . All values are obtained at  $t = 10.56 t_A$ .

axial magnetic field,  $B_{z\max}$ , decreases. It can be seen that the asymptotic value of  $B_{z\max}$  can reach  $1.34 B_0$  in some simulation cases.

#### 4.3.4 Effect of Ratio $B_\theta/B_0$ on the Wave Speed

To study the propagation of large-amplitude Alfvén waves, we calculate the propagation velocities of the Alfvén wave along the  $z$ -direction for different initial azimuthal magnetic field components ( $B_{\theta\max}$ ). Other parameters are chosen as  $z_0 = 3a$ ,  $b = a$ , and  $\beta = 1$ . Figure 4.10 shows the propagation velocity of the Alfvén wave along the  $z$ -direction as a function of the initial maximum  $B_\theta$  ( $B_{\theta\max}$ ). The data are obtained from several runs with different initial  $B_{\theta\max}$  and the velocity in each case is the averaged velocity by excluding the initial ( $t < 2t_A$ ) oscillations. It can be seen from Figure 4.10 that even for a very large azimuthal component of the magnetic field ( $B_{\theta\max} \simeq 1 - 4B_0$ ) the propagation velocity along the  $z$ -direction is still nearly the Alfvén velocity.

We have also run cases in which the plasma density and pressure inside the helical flux tube are higher than outside uniform plasma density and pressure. A positive radial pressure gradient force exists in the initial flux tube. Consequently, the pinch effect is reduced and the amplitude of the fast magnetosonic wave is reduced. Other features, especially the propagation behavior of the Alfvén wave and the fast magnetosonic wave, are found to be similar to those cases with the initially uniform density and pressure.

Finally, it is pointed out that the evolution of the magnetic flux ropes studied here is an ideal MHD effect and the same results are expected to be obtained with a zero resistivity. The use of a finite resistivity in the present calculation is mainly for the stability of the numerical scheme.

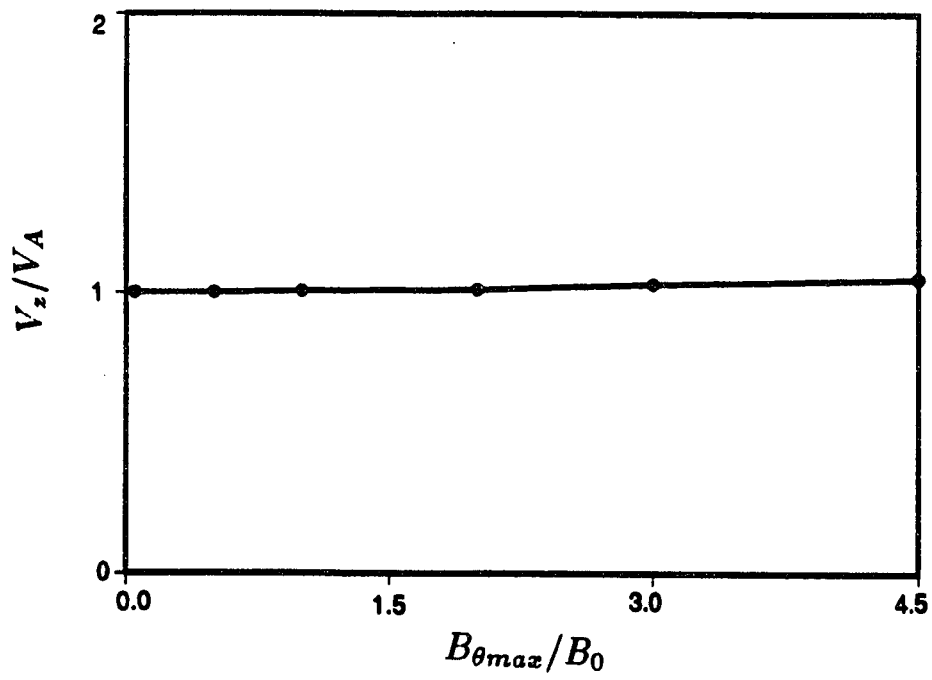


**Figure 4.10** The propagation velocity of the Alfvén wave along the z-direction for different azimuthal magnetic field components ( $B_{\theta_{max}}$ ).



#### 4.4 Evolution of Localized Plasma Vortices

As mentioned in the introduction of this chapter, plasma vortices may lead to the formation of helical magnetic field structures, similar to the magnetic flux ropes studied above. The Alfvén wave associated with the azimuthal magnetic field and the plasma vortex may propagate away from the source region. In this section, the simulation results of the formation of the helical magnetic field and the propagation of the Alfvén wave associated with the localized plasma vortices are presented.

##### 4.4.1 Initial and Boundary Conditions

The initial flow pattern of the localized plasma vortex structure is given by

$$\begin{aligned}
 V_r &= 0 \\
 V_\theta &= \begin{cases} V_{\theta 0}(r/a) \exp(-r^2/a^2) \operatorname{erf}[(z_0 - |z|)/b] & \text{if } |z| \leq z_0 \\ 0 & \text{otherwise} \end{cases} \quad (4.23) \\
 V_z &= 0
 \end{aligned}$$

where  $V_{\theta 0}$  is a constant,  $a$  is the characteristic size of the plasma vortex,  $2z_0$  is the initial length of the plasma vortex region, and  $b$  is the transition width at the two ends of the plasma vortex. The vortex has a finite length  $2z_0$  along the magnetic field. The initial magnetic field is assumed to be constant and is taken to be  $\mathbf{B} = B_z \hat{\mathbf{z}}$  with  $B_z = B_0$ .

The boundary conditions are the same as those for the flux tube cases except for  $V_\theta$  and  $B_\theta$  at  $z = 0$ . The  $V_\theta$  profile given in (4.23) is symmetric about  $z = 0$ . From the analysis of equations (4.6)–(4.13) with the presently given initial conditions, it can be found that  $\rho$ ,  $\varepsilon_T$ ,

$V_r$ ,  $V_\theta$ , and  $B_z$  are symmetric about  $z = 0$ , while  $V_z$ ,  $B_r$ , and  $B_\theta$  are antisymmetric about  $z = 0$ . Therefore, the boundary conditions at  $z = 0$  for the vortex evolution are

$$\frac{\partial \rho}{\partial z} = \frac{\partial \varepsilon_T}{\partial z} = \frac{\partial V_r}{\partial z} = \frac{\partial V_\theta}{\partial z} = \frac{\partial B_z}{\partial z} = 0 \quad (4.24)$$

$$V_z = B_r = B_\theta = 0 \quad (4.25)$$

By comparing the above relations with (4.19) and (4.20), one can see that only the symmetry properties for  $V_\theta$  and  $B_\theta$  are changed. For a given flux tube,  $B_\theta$  is symmetric and  $V_\theta$  is antisymmetric about  $z = 0$ , while  $V_\theta$  is symmetric and  $B_\theta$  is antisymmetric about  $z = 0$  for a given plasma vortex.

In addition, the simulation domain and the normalizations used in this section are the same as those for the flux tubes.

#### 4.4.2 Simulation Results

We present the simulation results for a case with an initial plasma vortex, as given in (4.23). The parameters chosen are  $z_0 = 3a$ ,  $b = a$ ,  $V_{\theta 0} = 1.17V_A$ , and  $\beta = 1$ . The corresponding maximum initial azimuthal velocity is  $V_{\theta \max} = 0.5V_A$ . This initial  $V_\theta$  is limited to a small region with  $0 \leq r \leq 2a$  and  $0 \leq z \leq z_0$ . The initial plasma density, plasma pressure, and the magnetic field are assumed to be uniform both inside and outside the flux tube.

Figure 4.11 (from top panel to bottom panel) shows contour plots of the plasma density,  $\rho$ , the azimuthal magnetic field,  $B_\theta$ , the azimuthal velocity,  $V_\theta$ , the plasma pressure,  $P$ , and the magnetic pressure,  $B^2/2\mu_0$ , at different simulation times. For an initially given plasma vortex, the magnetic field is twisted due to the vortex motion, leading to the formation of the

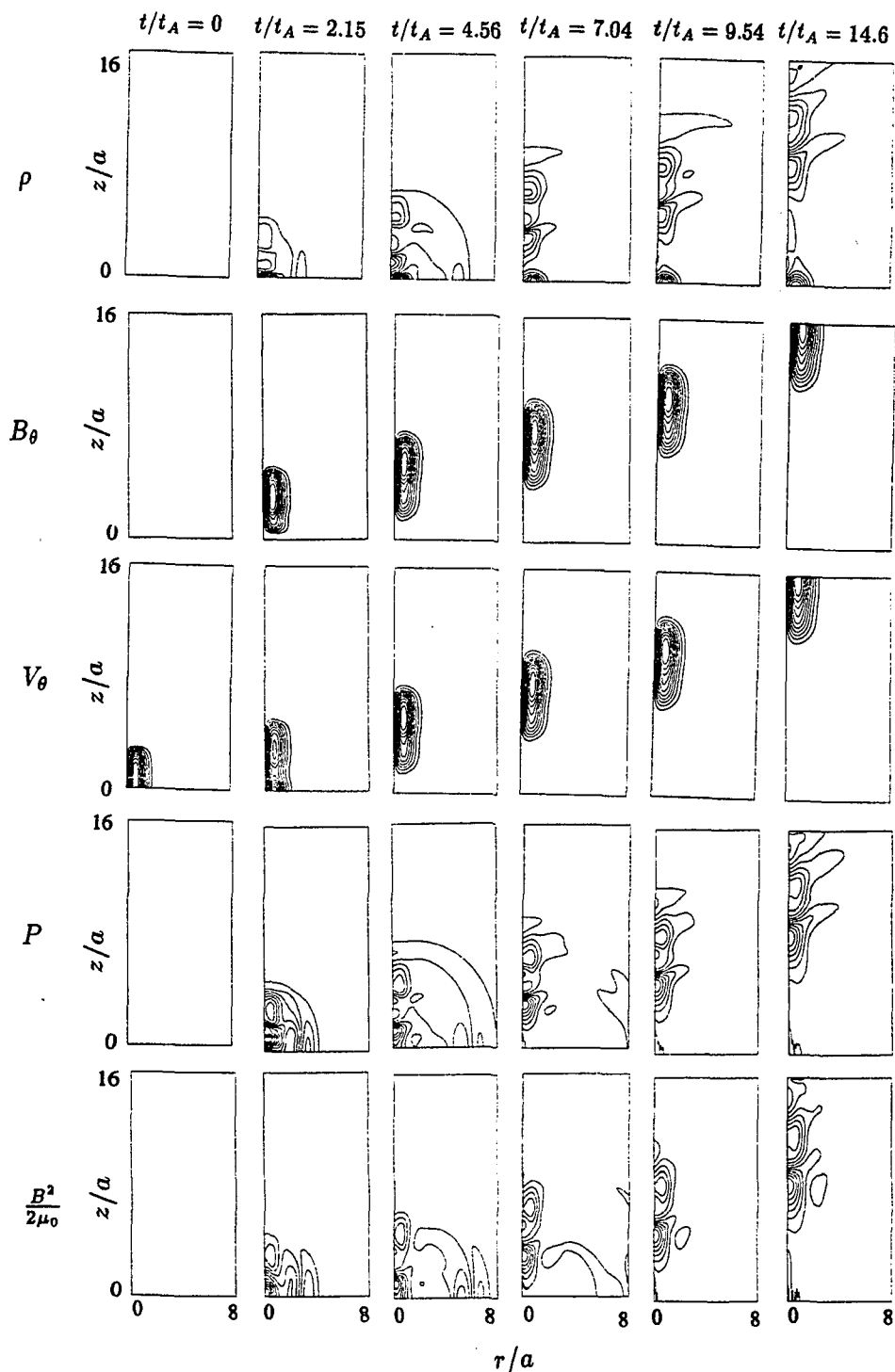


**Figure 4.11** Same as Fig. 4.2, but for an initially given plasma vortex. The parameters used here are  $V_{\theta\max}(t=0) = 0.5V_A$ ,  $z_0 = 3a$ ,  $b = a$ , and  $\beta = 1$ . The scale length is defined as  $a = V_A t_A$ , where  $V_A$  is the Alfvén velocity.

azimuthal magnetic field. The  $B_\theta$  and  $V_\theta$  contours in Figure 4.11 have very similar patterns after the initial phase. Note that  $V_\theta$  is positive and  $B_\theta$  is negative in Figure 4.11, while  $V_\theta$  is negative and  $B_\theta$  is positive for Case A shown in Figure 4.2. The azimuthal velocity structure first expands along the  $z$ -direction to about twice its initial length and separates into two parts, one in the positive  $z$ -direction and another in the negative  $z$ -direction (see Figure 4.11 at  $t = 0$  and  $t = 4.56 t_A$  for the  $z > 0$  part). In the mean time, two helical magnetic field structures are formed, which have the same profiles as the azimuthal velocity structures after an initial transition. After the separation, these structures propagate along the  $z$ -direction. The expansion and propagation velocity of the azimuthal magnetic field and the azimuthal velocity structure along the  $z$ -axis is found to be the Alfvén velocity ( $V_A$ ) and the radial expansion speed is found to be very small and negligible. After some initial transitions ( $t \geq 6 t_A$ ),  $V_\theta$  and  $|B_\theta|$  are found to have the same contour profiles as shown in Figure 4.11. In fact, we find that  $V_\theta/V_A = -B_\theta/B_0$  in the wave region. This property indicates the presence of the Alfvén wave propagating along the  $z$ -direction. From contours of the plasma density, the plasma pressure, and the magnetic pressure in Figure 4.11, it can be seen that at the earlier times ( $t = 2.15 t_A$ ,  $t = 4.56 t_A$ , and  $t = 7.04 t_A$ ), a wave mode is propagating in all directions with a high speed. Careful calculations of the propagation speed indicate again that this wave mode is the fast magnetosonic mode.

Figure 4.12 shows contour plots of currents along the  $r$ -direction ( $J_r$ ) (top panel) and along the  $z$ -direction ( $J_z$ ) (bottom panel) at different simulation times for the above case. It can be seen that the overall structure of the current system is similar to that for a magnetic flux tube as shown in Figure 4.5. The current along the  $z$ -direction ( $J_z$ ) flows along the

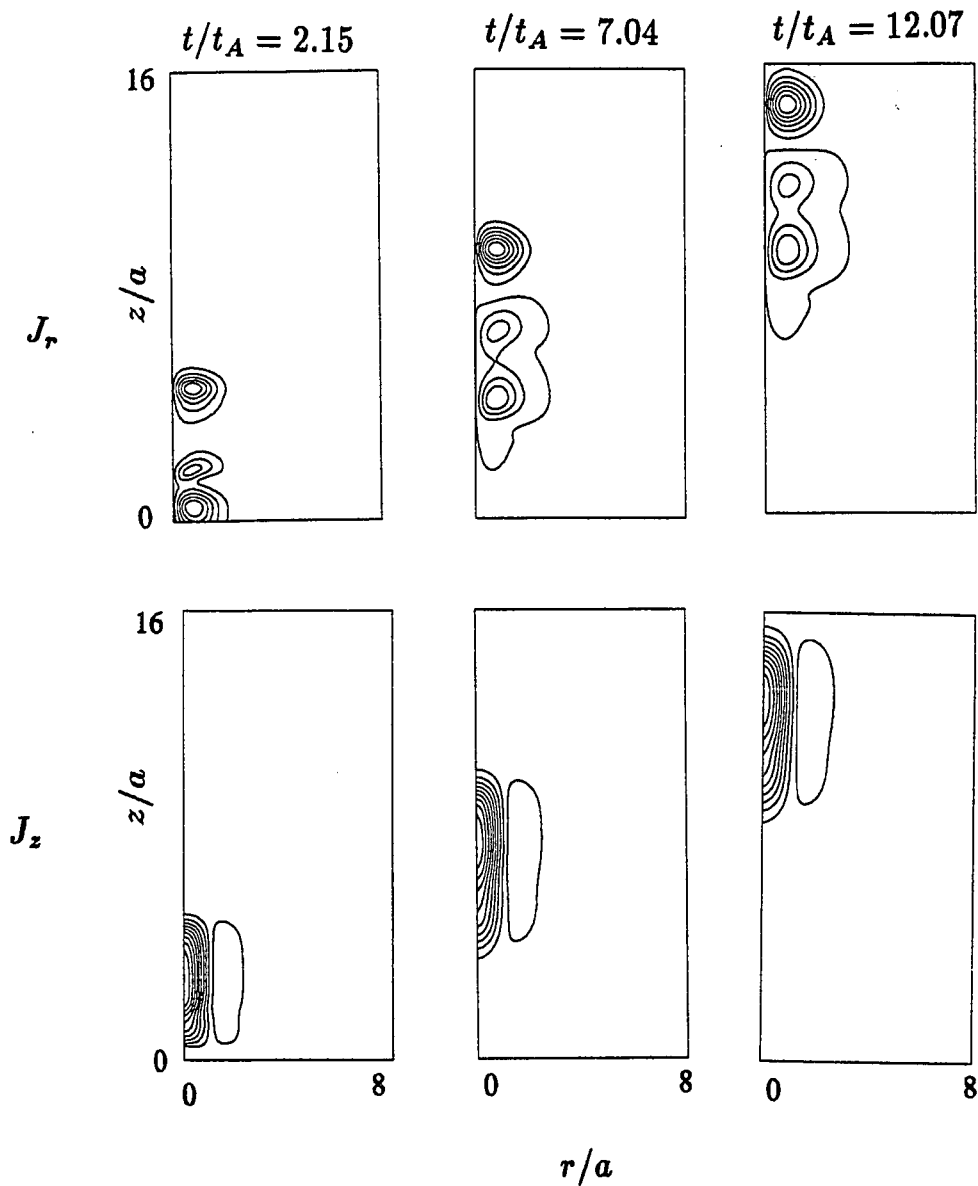


**Figure 4.12** Contour plots of the currents (top) along the  $r$ -direction ( $J_r$ ) and (bottom) along the  $z$ -direction ( $J_z$ ) for the above case at simulation times  $t/t_A = 2.15$ ,  $7.04$ , and  $12.07$ . For a given plasma vortex, the initial current is zero.

negative  $z$ -direction in the inner region ( $r < a$ ) and the return current ( $J_z < 0$ ) flows in the outer part ( $r > a$ ).

From the above analysis, it can be seen that the same conclusions drawn earlier for the evolution of magnetic ropes can also be obtained for the evolution of plasma vortices. At an initial phase, the fast magnetosonic mode and the Alfvén mode coexist. After this initial phase, the fast wave mode is separated from the Alfvén wave mode and the dominant wave becomes the Alfvén wave, which propagates along the  $z$ -direction with the Alfvén velocity,  $V_A$ . The localized azimuthal velocity structure first expands along its axial direction to about twice its initial length and generates a helical magnetic field structure, then evolves into two separate regions, and finally each region propagates at the Alfvén speed in opposite directions along its axial direction. The propagation velocity along its axial direction is the Alfvén velocity. On the other hand, the radial expansion of the region with the vortex motion is found to be small and negligible.

#### 4.5 Discussion

The magnetic field lines of the flux tube shown in Figure 4.6 can be considered as magnetic field lines which connect the IMF and the geomagnetic field during flux transfer events. As shown in Figure 4.6a, the center part of the flux tube corresponds to the part of the magnetopause where magnetic reconnection takes place. After the formation of the FTE flux tube, the magnetic flux tube first expands along the tube axis toward both the magnetosheath side and the magnetospheric side, as shown in Figure 4.6b. It then evolves into two separate regions as shown in Figure 4.6c. The propagation speed of the flux tube along the axial direction is the Alfvén speed, and the radial expansion speed is found to be negligible after

the initial stage. The maximum azimuthal magnetic field decreases and finally reaches to an asymptotic value. The length of each separate tube with azimuthal magnetic field remains constant during the propagation.

As mentioned in the introduction, helical magnetic field structures exist inside the FTE observed at the magnetopause. The helical magnetic field structure is formed at the magnetopause due to the magnetic reconnection with a southward IMF component ( $B_z$ ) and a finite IMF  $B_y$  component. The axial magnetic field is formed due to a finite IMF  $B_y$  component in the multiple X line reconnection model. The observed ratio of the azimuthal field component to the axial field component is  $B_\theta/B_0 \sim 0.3 - 0.5$  [e.g., *Saunders et al.*, 1984]. The radius of the flux tube is  $\sim 0.5 R_E$  and the length of the flux tube is  $\sim 1 - 4R_E$  near the magnetopause, depending on the formation models. After the formation of the flux tube, Alfvén waves associated with the helical magnetic field inside the flux tube are observed to propagate along the flux tube, as mentioned earlier. Our simulation results can be used to explain the propagation behavior of the FTE flux tube and some of the observed properties of the FTEs.

Based on equation (4.14), the initial helical magnetic field is confined in the region with  $0 \leq r \leq 2a$  and  $-z_0 \leq z \leq z_0$ . For FTEs, we choose  $a = 0.5 R_E$  and  $z_0 = (2 - 8)a = (1 - 4)R_E$ . Therefore, for the typical length of flux tubes of  $\sim 1 - 4R_E$  and  $B_{\theta\max}(t = 0) \simeq 1 - 3B_0$  in the source region, the asymptotic value of  $B_{\theta\max}$  is  $\sim 0.35 - 0.5B_0$ , as can be seen from Figure 4.4c. For the typical magnitude of magnetic field at the dayside magnetopause,  $B_0 = 30$  nT, the asymptotic value of  $B_{\theta\max}$  is  $\sim 10 - 15$  nT, which is consistent with observations [*Paschmann et al.*, 1982; *Saunders et al.*, 1984].

Based on our simulation result, the FTE flux tube formed at the magnetopause first expands along the axial direction of the flux tube to about twice its initial length and then

evolves into two separate flux tubes propagating in opposite directions with the Alfvén velocity, while the radial expansion of the flux tube is small after the initial stage. For the FTE flux tube having a length  $z_0/a \sim 2 - 8$ , the time leads to the separation of the flux tube is  $t_s \simeq z_0/V_A$ . The separation time may be estimated as follows. The Alfvén speed near the magnetopause is  $\sim 200$  km/s. If we choose  $z_0 \simeq 1 - 4R_E$ , then the time it takes for a flux tube to evolve into two separate flux tubes is  $t_s \simeq z_0/V_A \simeq 30 - 120$  s. The flux tube which propagates toward the ionosphere will produce footprints in the ionosphere, which may explain observations of Alfvén waves by *Goertz et al.* [1985], *Lanzerotti et al.* [1986], and *Lockwood et al.* [1990].

It may be noted that in our simulation the outflow boundary condition is used at  $z = L$ . However, the Alfvén waves from the dayside magnetopause may be modified by the reflection processes in the ionosphere, which may reduce electric fields and enhance field-aligned currents in the flux tube [e.g., *Lee*, 1986].

Recent simulation studies of the three-dimensional magnetic reconnections [*Fu et al.*, 1990; *Hesse et al.*, 1990; *Lee*, 1990] indicate that the magnetic ropes formed by the multiple X line reconnection process usually have a complicated field line topology at the two ends of the magnetic ropes. These magnetic ropes have frayed ends, in which the rope field lines at each end have mixed connections to the ambient fields. Our present simulation results cannot be directly applied to the evolution of these frayed magnetic ropes. It is speculated that the azimuthal field in the magnetic ropes may propagate as Alfvén waves along the connected field lines to the ambient fields on both sides, leading to the formation of four propagating ropes. This problem can only be studied by a three-dimensional simulation model.



#### 4.6 Summary

In this study, we have investigated the evolution of localized magnetic flux ropes and localized plasma vortices in space plasmas by using a two-dimensional compressible MHD simulation method. The simulation results are used to study the evolution of the plasma vortices in the magnetopause-boundary layer and magnetic flux ropes associated with flux transfer events at the dayside magnetopause. The principal results may be summarized as follows.

1. In the initial phase of the evolution of localized magnetic flux ropes or localized plasma vortices, both the fast magnetosonic wave and the Alfvén wave are developed. The fast magnetosonic wave propagates outward in all directions with the fast-mode speed. After this initial phase, the Alfvén wave becomes the dominant wave mode for the evolution of the magnetic flux ropes or the plasma vortices.
2. The localized magnetic flux rope or the localized plasma vortex first expands along its axial direction to about twice its initial length, then evolves into two separate regions, and finally each region propagates at the Alfvén speed in opposite directions along its axial direction. The propagation velocity along its axial direction is the Alfvén velocity. On the other hand, the radial expansion of the magnetic flux rope or the plasma vortex is found to be small and negligible.
3. The time needed for a magnetic flux rope to evolve into two separate flux ropes is typically  $\sim z_0/V_A$ , where  $z_0$  is the half-length of the initial rope and  $V_A$  is the Alfvén speed. However, as the ratio  $B_\theta/B_z$  becomes larger, the time it takes for a magnetic flux rope to evolve into two separate flux ropes also becomes longer.

4. Simulation results show that even for a very large azimuthal component of the magnetic field ( $B_\theta \simeq 1 - 4B_z$ ) the propagation velocity of the large-amplitude Alfvén waves along the axial direction of the magnetic flux rope remains the Alfvén velocity.

5. For flux transfer events at the Earth's magnetopause, the magnetic flux ropes first expands along its axial direction to about twice its initial length, then evolves into two separate flux ropes, which propagate in opposite directions with the Alfvén velocity. The simulation results indicate that after the evolution the azimuthal magnetic field is reduced to  $B_\theta \simeq 0.3 - 0.5B_0 \simeq 10 - 15$  nT (for  $B_0 = 30$  nT), which is consistent with satellite observations. The Alfvén waves, which carry the field-aligned currents, propagate along the flux rope toward the magnetosheath and toward the magnetosphere. The Alfvén waves also propagate to the ionosphere and produce footprints in the ionosphere.

6. The plasma vortices produced by the Kelvin-Helmholtz instability in the low-latitude boundary layer may generate twisted magnetic field lines and large-amplitude Alfvén waves, which carry field-aligned currents and provide the link for their coupling to the polar ionosphere.

## CHAPTER 5

### Summary and Discussion

The interaction between the solar wind and the Earth's magnetosphere consists mainly of the transfer of energy, momentum, and mass from the solar wind to the magnetosphere, and subsequently to the ionosphere. The magnetopause-boundary layer is the interface region where these transfers take place. The velocity difference across the magnetopause-boundary layer causes a sheared plasma flow, which in turn produces plasma vortices in the boundary layer region. The plasma vortices produce a localized convection electric field and generate Alfvén waves, which carry field-aligned currents and the convection electric field to the ionosphere. The finite conductivity in the ionosphere provides a dragging force to the plasma flow in the boundary layer and leads to the decay of the plasma vortices in the boundary layer region.

As mentioned earlier, Alfvén waves provide the link for the coupling of the plasma vortices in the magnetosphere to the polar ionosphere. Alfvén waves, which carry field-aligned currents, propagate along the magnetic field lines between the magnetosphere and the ionosphere. Along with the Alfvén waves, the electric field and the field-aligned currents also propagate from the magnetosphere to the ionosphere, producing footprints in the ionosphere. The Alfvén waves formed in the magnetosphere may be modified by the reflection processes in the ionosphere, which may reduce electric fields and enhance field-aligned currents [e.g., *Lee, 1986*].

Due to the complexity of the magnetosphere-ionosphere interaction, it is difficult to develop a complete three-dimensional model to address every aspect of the coupled system.

The approach of the work reported in this thesis is to divide the magnetosphere-ionosphere coupling system into several related components. Each component addresses certain aspects of the magnetosphere-ionosphere coupling process.

First, the plasma dynamics and structure of the magnetopause-boundary layer region are studied on the basis of a two-dimensional incompressible magnetohydrodynamic numerical model. In the simulation, plasma is driven into the boundary layer region by imposing a diffusion flux along the magnetopause. The vortex motions associated with the Kelvin-Helmholtz instability are observed in the simulation. The plasma flows are mainly tailward but small sunward flows are also observed. The plasma density profiles in the boundary layer show vortex structures. The resulting vortex structures in the plasma density and the flow velocity may coalesce as they are convected tailward, causing them to grow in size. The boundary layer thickness increases with increasing longitudinal distance from the subsolar point. A mixing region is formed where magnetosheath plasma and magnetospheric plasma mix due to the vortex motions. In the later stage of development, a density plateau is formed in the central part of the boundary layer. Many features of the satellite observations of the boundary layer can be explained using our numerical model.

A magnetosphere-ionosphere coupling model is presented in Chapter 3 to study the coupling of the plasma vortices in the boundary layer to the polar ionosphere. The presence of the finite ionospheric conductivity exerts a dragging force on the plasma motion in the magnetosphere and slows down the magnetospheric convection [Sonnerup, 1980; Kan and Lee, 1980; Lotko *et al.*, 1987]. In the model, the ionosphere is characterized by the current continuity equation and the Ohm's law with the Pedersen and Hall conductivities and the field-aligned potential drop is also included. In addition, the ionospheric conductivity is allowed to be enhanced due to precipitation of the accelerated electrons in the upward field-aligned

current regions. It is found that the plasma vortices generated in the duskside (dawnside) region of the boundary layer mainly lead to the presence of localized upward (downward) field-aligned current regions along the post-noon (pre-noon) sector in both the northern and the southern polar ionospheres. The competing effect of the formation and decay of vortices leads to the formation of strong vortices only in limited regions. Several enhanced conductivity regions which are associated with the boundary layer vortices and the upward field-aligned current regions can be found along the post-noon auroral oval. These enhanced conductivity regions may account for the observed dayside auroras which show bright features resembling "beads" or "pearls" [Lui *et al.*, 1989; Potemra *et al.*, 1990].

The Alfvén transit time between the magnetosphere and the ionosphere is assumed to be much shorter than the growth time of the plasma vortices in Chapter 3. In reality, the Alfvén transit time between the magnetosphere and the ionosphere is about 100 sec and is comparable to the vortex growth and decay times. The ionospheric response to changes in the magnetospheric plasma vortices will be delayed by the Alfvén transit time to the ionosphere and back. The neglect of the Alfvén transit time leads to an overestimation of the damping effect of the ionosphere to the dynamics in the boundary layer.

In Chapter 4, the generation and propagation of Alfvén waves along geomagnetic field lines from localized plasma vortices, as well as magnetic flux ropes, are studied. It is found that the evolution of the localized plasma vortices and the magnetic flux ropes leads to the generation of large-amplitude Alfvén waves, which carry field-aligned currents and provide the link for the coupling of helical magnetic ropes and plasma vortices in the magnetosphere to the polar ionosphere.

From the simulation results in Chapter 4, it can be seen that the FAC is a localized structure and is carried by Alfvén waves propagating between the magnetosphere and the

ionosphere with the Alfvén velocity. Therefore, it needs twice the Alfvén transit time for Alfvén waves to propagate from the magnetosphere to the ionosphere and then back to the magnetosphere. At this time, the ionospheric effects will affect the plasma dynamics in the magnetosphere. The model in Chapter 2 without the ionospheric effect is a simplified model. The use of the electrostatic field-aligned potential drop and the linear current-voltage relationship (3.14) in Chapter 3 implies that the Alfvén transit time is much shorter than the growth and decay times of the vortex. Therefore, the model in Chapter 3 overestimates the ionospheric damping effect. The use of a relatively small ionospheric background conductivity in Chapter 3 may compensate some of the Alfvén wave effects.

A three-dimensional model is needed to combine self-consistently the model of the Alfvén wave propagation presented in Chapter 4 and the magnetosphere-ionosphere coupling model used in Chapter 3, which is difficult to develop due to the complexity of the coupled system. To improve the magnetosphere-ionosphere coupling model developed in this thesis and to explain more observations, a number of extensions of this work can be carried out based on the general framework of this ionosphere-magnetosphere coupling model. Adding the ionospheric reflection to the Alfvén wave propagation is an obvious extension of the model presented in Chapter 4. When the ionospheric reflection effects are included, one may study the Alfvén wave propagation between the magnetosphere and the ionosphere in a real content of the magnetosphere-ionosphere coupling model. The ionospheric closure of the FAC carried by the Alfvén wave is important for the dynamics of auroral activities. If the ionospheric conductivity is low, as in the nightside winter ionosphere, the magnetic fields of the incident and reflected waves tend to cancel and the electric field is enhanced. If the ionospheric conductivity is high, as in the dayside summer ionosphere, most of the incident wave energy can be reflected and the electric fields of the incident and reflected waves cancel

so that the ionospheric electric field is reduced and the FAC is enhanced [e.g., *Southwood and Hughes, 1983; Lee, 1986; Seyler, 1990; Lotko and Shen, 1991*].

Another extension is to include the variation of magnetic fields in the models presented in Chapters 2 and 3. The neglect of the variation of the magnetic field is based on the assumption that the variation of the magnetic field in the boundary layer region is very small, as shown in Figure 1.4. If the magnetic fields in the magnetosheath and in the magnetosphere are not parallel, the tense force tends to stabilize the KH instability at the magnetopause. On the other hand, if the magnetic fields at two sides are parallel or antiparallel, the KH instability can also develop at the magnetopause and leads to the deformation of the magnetopause. As an extension of the model presented in this thesis, the simulation domain should include both the magnetosheath and the magnetosphere so that the magnetopause is inside the simulation domain. The magnetic fields in the magnetosheath and in the magnetosphere are not parallel in the general case. A large anomalous diffusion may exist at the magnetopause to allow the high-density magnetosheath plasma to diffuse into the magnetosphere. It is expected that the presence of the magnetic field components in the simulation plane in Chapters 2 and 3 will slow down the development of the KH instability due to the tension force.

The main limitation of the model presented in this thesis is that it is incapable of modeling kinetic effects of particles because it is an MHD model. The particle behavior plays an important role in the formation of auroral bright spots. As a consequence, many phenomena associated with particle motions cannot be addressed, e.g., the electron acceleration process along the magnetic field lines due to a parallel electric field or the field-aligned potential drop in the upward FAC regions, wave-particle interaction effect, plasma heating due to waves, and finite Larmor radius effect. A particle simulation code is needed to address these problems. In addition, the simplified ionospheric model used in this thesis neglects the variations inside

the ionosphere and also the effects due to the neutral wind. A three-dimensional global MHD or particle simulation code is needed to address many problems related to the magnetosphere-ionosphere coupling process.

In summary, the present study of the plasma dynamics of the magnetopause-boundary layer region provides a theoretical explanation for the observed plasma vortices in the boundary layer region. The evolution of the plasma vortices along geomagnetic field lines leads to the generation of large-amplitude Alfvén waves, which carry field-aligned currents to the polar ionosphere. The observed auroral bright spots in the post-noon auroral oval may be explained by the formation of enhanced electron precipitation regions through the coupling of the plasma vortices to the polar ionosphere.



## APPENDIX

### Numerical Technique for Solving Magnetosphere-Ionosphere Coupling Equations

In the following, the numerical techniques used in Chapter 3 to solve the magnetosphere-ionosphere coupling equations (3.25)–(3.34) are presented.

First, equations (3.25)–(3.28) are a complete set if  $J_{\parallel i}$  is known. The numerical scheme for solving (3.25)–(3.28) with  $J_{\parallel i} = 0$  has been given in Chapter 2. In order to simulate the fine structures of the boundary layer, the effects of numerical errors should be minimized. To reduce the numerical errors, a high-order finite differencing scheme is developed, which can be described as: (1) a two-step method is used to time-center the time derivatives, which gives a second-order accuracy in time; (2) a third-order spatial scheme (equation (2.5)) is used for the convective terms  $\mathbf{v} \cdot \nabla N$  and  $\mathbf{v} \cdot \nabla \Omega$ , which introduces only a fourth-order numerical dissipation; (3) the usual second-order space-center differencing scheme is used for the diffusion term. It can be shown that this numerical scheme is stable even for a very small viscosity.

Next, we describe the numerical method to solve  $\phi_{\parallel}$ ,  $J_{\parallel i}$ , and other ionospheric quantities. The coupling equations (3.29)–(3.34) can be solved if the magnetospheric streamline function  $\psi$  is known. To simplify expressions in the derivation, we rewrite (3.32) as

$$\phi_{\parallel} = -\alpha'_0 J_{\parallel i} \quad (\text{A1})$$

where

$$\alpha'_0 = \begin{cases} \alpha_0 & \text{if } J_{\parallel i} < 0 \\ 0.1\alpha_0 & \text{if } J_{\parallel i} > 0 \end{cases} \quad (\text{A2})$$

By inserting (3.33) and (3.34) into (3.30) and using  $\nabla \cdot \mathbf{E}_m = -\Omega$  from (3.20), one obtains

that

$$J_{\parallel i} = \Sigma_0(\nabla\Sigma_p \cdot \mathbf{E}_m + R_{hp}\nabla\Sigma_p \cdot \hat{z} \times \mathbf{E}_m - \Sigma_p\Omega - \nabla\Sigma_p \cdot \nabla\phi_{\parallel} - R_{hp}\nabla\Sigma_p \cdot \hat{z} \times \nabla\phi_{\parallel} - \Sigma_p\nabla^2\phi_{\parallel}) \quad (\text{A3})$$

Inserting (A1) to the left hand side of (A3), we can express (A3) in the following form:

$$A\nabla^2\phi_{\parallel} + B\nabla_x\phi_{\parallel} + C\nabla_y\phi_{\parallel} - \phi_{\parallel} = S \quad (\text{A4})$$

where  $\nabla^2 = \frac{\partial^2}{\partial x^2} + \frac{\partial^2}{\partial y^2}$ ,  $\nabla_x = \frac{\partial}{\partial x}$ , and  $\nabla_y = \frac{\partial}{\partial y}$ . The coefficients and the source term in (A4) are:

$$A = \alpha'_0\Sigma_0\Sigma_p \quad B = \alpha'_0\Sigma_0g_1 \quad C = \alpha'_0\Sigma_0g_2$$

$$S = \alpha'_0\Sigma_0(-\Sigma_p\Omega + g_1E_{mx} + g_2E_{my}) \quad (\text{A5})$$

$$g_1 = \frac{\partial\Sigma_p}{\partial x} + R_{hp}\frac{\partial\Sigma_p}{\partial y} \quad g_2 = \frac{\partial\Sigma_p}{\partial y} - R_{hp}\frac{\partial\Sigma_p}{\partial x}$$

It can be seen from (3.31) and (A2) that  $\Sigma_p$  and  $\alpha'_0$  are also function of  $\phi_{\parallel}$ . Therefore, equation (A4) can be used to solve for  $\phi_{\parallel}$ . However, equation (A4) is difficult to solve due to the nonuniform coefficients in (A5). Also, it is found that if the Hall to Pedersen conductivity ratio ( $R_{hp}$ ) is too large, the iteration procedure used to solve (A4) tends to diverge. The numerical technique used to solve (A4) is described below.

An iteration method is used at each time step ( $n$ ) to solve for  $\phi_{\parallel}$  from (A4) since the coefficients in (A5) are also function of  $\phi_{\parallel}$ . The  $\phi_{\parallel}$  value at the previous step is used to calculate the coefficients in (A5) and to solve (A5) for  $\phi_{\parallel}$  at the current step, namely,  $\phi_{\parallel}^{l,n} \rightarrow \Sigma_p^{l,n}$ ,  $\alpha_0^{l,n} \rightarrow \phi_{\parallel}^{l+1,n}$ , where  $l$  is the iteration level. The iteration will end when the difference of  $\phi_{\parallel}$  values at different iteration levels is smaller than a preset small parameter  $\varepsilon$ , namely,  $|1 - \phi_{\parallel}^{l,n}/\phi_{\parallel}^{l+1,n}| \leq \varepsilon$ .

To handle the case with a large Hall to Pedersen conductivity ratio ( $R_{hp}$ ), which usually causes problems in the coefficients  $B$  and  $C$ , a portion of terms in  $B$  and  $C$  are moved from the left hand side to the right hand side of (A4). Those moved parts remain unchanged at different iteration levels. The technique is shown below. Define

$$\begin{aligned} g_{11} &= \frac{\partial \Sigma_p}{\partial x} + R'_{hp} \frac{\partial \Sigma_p}{\partial y} & g_{12} &= (R_{hp} - R'_{hp}) \frac{\partial \Sigma_p}{\partial y} \\ g_{21} &= \frac{\partial \Sigma_p}{\partial y} - R'_{hp} \frac{\partial \Sigma_p}{\partial x} & g_{22} &= -(R_{hp} - R'_{hp}) \frac{\partial \Sigma_p}{\partial x} \end{aligned} \quad (\text{A6})$$

where  $R'_{hp}$  is a parameter with  $0 \leq R'_{hp} \leq R_{hp}$ . The definitions of  $g_1$  and  $g_2$  in (A5) can be expressed as

$$g_1 = g_{11} + g_{12} \quad g_2 = g_{21} + g_{22} \quad (\text{A7})$$

After the terms with  $g_{12}$  and  $g_{22}$  have been moved to the right hand side, equation (A4) can be rewritten as

$$A \nabla^2 \phi_{\parallel} + B' \nabla_x \phi_{\parallel} + C' \nabla_y \phi_{\parallel} - \phi_{\parallel} = S' + H \quad (\text{A8})$$

where

$$\begin{aligned} B' &= \alpha'_0 \Sigma_0 g_{11} & C' &= \alpha'_0 \Sigma_0 g_{21} \\ S' &= \alpha'_0 \Sigma_0 (-\Sigma_p \Omega + g_{11} E_{mx} + g_{21} E_{my}) \end{aligned} \quad (\text{A9})$$

$$H = \alpha'_0 \Sigma_0 \{g_{12} (E_{mx} - \nabla_x \phi_{\parallel}) + g_{22} (E_{my} - \nabla_y \phi_{\parallel})\}$$

$H$  does not vary from an iteration level to another within a time step. It can also be shown that  $H$  is proportional to the Hall portion of the FAC density (the second term in equation (3.22)). If  $R'_{hp} = R_{hp}$ , no term is moved and (A8) is the same as (A4). On the other hand, all terms with the Hall conductivity are moved to the right hand side of (A4) if  $R'_{hp} = 0$ . We tested some values for  $R'_{hp}$  ( $0 \leq R'_{hp} \leq R_{hp}$ ) for the case with  $R_{hp} = 1$  and no significant

difference can be found in the simulation results. The cases with  $R_{hp} \geq 1.5$  usually diverge if  $R'_{hp} = R_{hp}$ , while they may converge if  $R'_{hp} < R_{hp}$ .

The coefficients  $A$ ,  $B'$ , and  $C'$  are functions of coordinates  $x$  and  $y$  for the general case. To find a fast solver for equation (A8), some further modifications are needed. If the coefficients  $A$ ,  $B'$ , and  $C'$  are independent of  $y$  and the boundary conditions along the  $y$ -direction can be treated periodically, then the fast Fourier transform (FFT) method can be used along the  $y$ -direction. To make the coefficients of terms  $\nabla^2 \phi_{\parallel}$ ,  $\nabla_x \phi_{\parallel}$ , and  $\nabla_y \phi_{\parallel}$  independent of  $y$ , the average of  $A$ ,  $B'$ , and  $C'$  over  $y$  is taken. The terms with coefficients dependent on  $y$  are moved to the right hand side of equation (A8) and treated as source terms. The boundary conditions along the  $y$ -direction are usually non-periodic, as used in our simulations. In order to use the FFT, periodic boundary conditions are needed. Appropriate expansion of the simulation domain along the  $y$ -direction may lead to the periodic conditions. If the original simulation domain is confined within  $0 \leq x \leq L_x$  and  $0 \leq y \leq L_y$ , then it can be shown that the vorticity is antisymmetric about the  $x$ -axis when the simulation domain is expanded to the region with  $-L_y \leq y \leq 0$ . From (3.26) and (A1), it may be shown that  $J_{\parallel}$ ; and  $\phi_{\parallel}$  have the same symmetry property as the vorticity. Then, it can be shown that for equation (A8)  $A$  and  $B'$  are symmetric and  $C'$  and  $S'$  (and  $H$ ) are antisymmetric about the  $x$ -axis. The periodic boundary conditions can be obtained with the above expansion. Therefore, the FFT method can be used along the  $y$ -direction with the above treatment. For the  $x$ -direction, the tridiagonal method is used. This method is proven to be very efficient for solving the coupling equations.

## REFERENCES

- Akasofu, S.-I., E. W. Hones, Jr., S. J. Bame, J. R. Asbridge, and A. T. Y. Lui, Magnetotail and boundary layer plasmas at a geocentric distance of  $\sim 18 R_E$ : VELA 5 and 6 observations, *J. Geophys. Res.*, **78**, 7257, 1973.
- Alfvén, H., *Cosmic Plasma*, D. Reidel, Hingham, Mass., 1981.
- Alfvén, H., and C.-G. Fälthammar, *Cosmical Electrodynamics*, Clarendon, Oxford, 1963.
- Anderson, R. R., C. C. Harvey, M. M. Hoppe, B. T. Tsurutani, T. E. Eastman, and J. Etcheto, Plasma waves near the magnetopause, *J. Geophys. Res.*, **87**, 2087, 1982.
- Axford, W. I., and C. O. Hines, A unifying theory of high-latitude geophysical phenomena and geomagnetic storms, *Can. J. Phys.*, **39**, 1433, 1961.
- Birn, J., M. Hesse, and K. Schindler, Filamentary structure of a three-dimensional plasmoid, *J. Geophys. Res.*, **94**, 241, 1989.
- Bryant, D. A., and S. Riggs, At the edge of the Earth's magnetosphere: A survey by AMPTE-UKS, *Philos. Trans. R. Soc. London, A, Ser. 328*, 43, 1989.
- Burlaga, L. F., MHD processes in the outer heliosphere, *Space Sci. Rev.*, **39**, 255, 1984.
- Burlaga, L. F., E. Sittler, F. Mariani, and R. Schwenn, Magnetic loop behind an interplanetary shock: Voyager, Helios, and IMP 8 observations, *J. Geophys. Res.*, **86**, 6673, 1981.
- Bythrow, P. F., R. A. Heelis, W. B. Hanson, R. A. Power, and R. A. Hoffman, Observational evidence for a boundary layer source of dayside region 1 field-aligned currents, *J. Geophys. Res.*, **86**, 5577, 1981.
- Bythrow, P. F., M. A. Doyle, T. A. Potemra, L. J. Zanetti, R. E. Huffman, C.-I. Meng, D. A. Hardy, F. J. Rich, and R. A. Heelis, Multiple auroral arcs and Birkeland currents: Evidence for plasma sheet boundary waves, *Geophys. Res. Lett.*, **13**, 805, 1986.
- Bythrow, P. F., T. A. Potemra, R. E. Erlandson, L. J. Zanetti, and D. M. Klumpar, Birkeland currents and charge particles in the high-latitude prenoon region: A new interpretation, *J. Geophys. Res.*, **93**, 9791, 1988.

- Chiu, Y. T., and J. M. Cornwall, Electrostatic model of a quiet auroral arc, *J. Geophys. Res.*, **85**, 543, 1980.
- Chiu, Y. T., A. L. Newman, and J. M. Cornwall, On the structure and mapping of auroral electrostatic potentials, *J. Geophys. Res.*, **86**, 10029, 1981.
- Cogger, L. L., J. S. Murphree, S. Ismail, and C. D. Anger, Characteristics of dayside 5577 Å and 3914 Å aurora, *Geophys. Res. Lett.*, **4**, 413, 1977.
- Eastman, T. E., The plasma boundary layer and magnetopause layer of the Earth's magnetosphere, Thesis, *Rep. LA-7842-T*, Los Alamos Sci. Lab., Los Alamos, N.M., June, 1979.
- Eastman, T. E., and E. W. Hones, Jr., Characteristics of the magnetospheric boundary layer and magnetopause layer as observed by Imp 6, *J. Geophys. Res.*, **84**, 2019, 1979.
- Eastman, T. E., E. W. Hones, Jr., S. J. Bame, and J. R. Asbridge, The magnetospheric boundary layer: Site of plasma, momentum and energy transfer from the magnetosheath into the magnetosphere, *Geophys. Res. Lett.*, **3**, 685, 1976.
- Elphic, R. C., C. T. Russell, J. A. Slavin, and L. H. Brace, Observations of the dayside ionosphere of Venus, *J. Geophys. Res.*, **85**, 7679, 1980.
- Elphic, R. C., C. A. Cattell, K. Takahashi, S. J. Bame, and C. T. Russell, ISEE-1 and 2 observations of magnetic flux ropes in the magnetotail: FTEs in the plasma sheet, *Geophys. Res. Lett.*, **13**, 648, 1986.
- Erlanson, R. E., L. J. Zanetti, T. A. Potemra, P. F. Bythrow, and R. Lundin, IMF  $B_y$  dependence of region 1 Birkeland currents near noon, *J. Geophys. Res.*, **93**, 9804, 1988.
- Evans, D. S., The characteristics of a persistent auroral arc at high latitude in the 1400 MLT sector, in *The Polar Cusp*, edited by J. Holtet and A. Egeland, pp. 99-109, D. Reidel, Boston, 1985.
- Farrugia, C. J., M. P. Freeman, S. W. H. Cowley, D. J. Southwood, M. Lockwood, and E. Etemadi, Pressure-driven magnetopause motions and attendant response on the ground, *Planet. Space Sci.*, **37**, 589, 1989.

- Freeman, M. P., and D. J. Southwood, The effect of magnetospheric erosion on mid- and high-latitude ionospheric flows, *Planet. Space Sci.*, 36, 509, 1988.
- Fridman, M., and J. Lemaire, Relationship between auroral electron fluxes and field-aligned electric potential difference, *J. Geophys. Res.*, 85, 664, 1980.
- Friis-Christensen, E., M. A. McHenry, C. R. Clauer, and S. Vennerstrom, Ionospheric traveling convection vortices observed near the polar cleft: A triggered response to sudden changes in the solar wind, *Geophys. Res. Lett.*, 15, 252, 1988.
- Fu, Z. F., L. C. Lee, and Y. Shi, A three-dimensional MHD simulation of the multiple X line reconnection process, in *The Physics of Magnetic Flux Ropes*, *Geophys. Monogr. Ser.*, vol. 58, edited by C. T. Russell, E. R. Priest, and L. C. Lee, pp. 515-519, AGU, Washington, D. C., 1990.
- Gary, S. P., and T. E. Eastman, The lower hybrid drift instability at the magnetopause, *J. Geophys. Res.*, 84, 7378, 1979.
- Gary, S. P., and A. G. Sgro, The lower hybrid drift instability at the magnetopause, *Geophys. Res. Lett.*, 17, 909, 1990.
- Glassmeier, K. H., M. Hoenisch, and J. Untiedt, Ground-based and satellite observations of traveling magnetospheric convection twin-vortices, *J. Geophys. Res.*, 94, 2520, 1989.
- Goertz, C. K., and R. W. Boswell, Magnetosphere-ionosphere coupling, *J. Geophys. Res.*, 84, 7239, 1979.
- Goertz, C. K., E. Nielson, A. Korth, K. H. Glassmeier, C. Haldoupis, P. Hoeg, and D. Hayward, Observations of a possible ground signature of flux transfer events, *J. Geophys. Res.*, 90, 4069, 1985.
- Gosling, J. T., M. F. Thomsen, D. W. Swift, and L. C. Lee, A note on the nature of the distant geomagnetotail magnetopause and boundary layer, *Geophys. Res. Lett.*, 12, 153, 1985.
- Gumett, D. A., R. R. Anderson, B. T. Tsurutani, E. J. Smith, G. Paschmann, G. Haerendel, S. J. Bame, and C. T. Russell, Plasma waves turbulence at the magnetopause: Observations from ISEE 1 and 2, *J. Geophys. Res.*, 84, 7043, 1979.

- Haerendel, G., G. Paschmann, N. Sckopke, H. Rosenbauer, and P. C. Hedgecock, The frontside boundary layer of the magnetosphere and the problem of reconnection, *J. Geophys. Res.*, **83**, 3195, 1978.
- Hesse, M., J. Birn, and K. Schindler, On the topology of flux transfer events, *J. Geophys. Res.*, **95**, 6549, 1990.
- Heikkila, W. J., Impulsive plasma transport through the magnetopause, *Geophys. Res. Lett.*, **9**, 159, 1982.
- Huba J. D., N. T. Gladd, and K. Papadopoulos, The lower-hybrid-drift instability as a source of anomalous resistivity for magnetic field reconnection, *Geophys. Res. Lett.*, **4**, 125, 1977.
- Iijima, T., and T. A. Potemra, Large-scale characteristics of field-aligned currents associated with substorms, *J. Geophys. Res.*, **83**, 599, 1978.
- Kan, J. R., and L. C. Lee, Theory of imperfect magnetosphere-ionosphere coupling, *Geophys. Res. Lett.*, **7**, 633, 1980.
- Kan, J. R., and Y. Kamide, Electrodynamics of the westward traveling surge, *J. Geophys. Res.*, **90**, 7615, 1985.
- Keskinen, M. J., H. G. Mitchell, J. A. Fedder, P. Satyanarayana, S. T. Zalesak, and J. D. Huba, Nonlinear evolution of the Kelvin-Helmholtz instability in the high-latitude ionosphere, *J. Geophys. Res.*, **93**, 137, 1988.
- Klein, L. W., and L. F. Burlaga, Interplanetary magnetic clouds at 1 AU, *J. Geophys. Res.*, **87**, 613, 1982.
- Knight, S., Parallel electric fields, *Planet. Space Sci.*, **21**, 741, 1973.
- LaBelle, J., and R. A. Treumann, Plasma waves at the dayside magnetopause, *Space Sci. Rev.*, **47**, 175, 1988.
- La Belle-Hamer, A. L., Z. F. Fu, and L. C. Lee, A mechanism for patchy reconnection at the dayside magnetopause, *Geophys. Res. Lett.*, **15**, 152, 1988.
- Lanzerotti, L. J., L. C. Lee, C. G. MacLennan, A. Wolfe, and L. V. Medford, Possible evidence of flux transfer events in the polar ionosphere, *Geophys. Res. Lett.*, **13**, 1089, 1986.



- Lanzerotti, L. J., R. D. Hunsucker, D. Rice, L. C. Lee, A. Wolfe, C. G. MacLennan and L. V. Medford, Ionospheric and ground-based response to field-aligned currents near the magnetospheric cusp regions, *J. Geophys. Res.*, *92*, 7739, 1987.
- Lanzerotti, L. J., A. Wolfe, N. Trivedi, C. G. MacLennan, and L. V. Medford, Magnetic impulsive events at high latitudes: Magnetopause and boundary layer plasma processes, *J. Geophys. Res.*, *95*, 97, 1990.
- Lee, L. C., Ion two-stream and modified two-stream instabilities in the magnetic neutral sheet, *Geophys. Res. Lett.*, *9*, 1159, 1982.
- Lee, L. C., Magnetic flux transfer events at the Earth's magnetopause, in *Proceedings of Chapman Conference on Solar Wind-Magnetosphere Coupling*, edited by Y. Kamide and J. Slavin, pp. 297-314, Terra Sci. Publ. Co., Tokyo, 1986.
- Lee, L. C., Time-dependent magnetic reconnection: Two- and three-dimensional MHD simulations, *Comput. Phys. Commun.*, *59*, 163, 1990.
- Lee, L. C., and Z. F. Fu, A theory of magnetic flux transfer at the Earth's magnetopause, *Geophys. Res. Lett.*, *12*, 105, 1985.
- Lee, L. C., and J. V. Olson, Kelvin-Helmholtz instability and the variation of geomagnetic pulsation activity, *Geophys. Res. Lett.*, *7*, 777, 1980.
- Lee, L. C., R. K. Albano, and J. R. Kan, Kelvin-Helmholtz instability in the magnetopause boundary layer region, *J. Geophys. Res.*, *86*, 54, 1981.
- Lee, L. C., Y. Shi, and L. J. Lanzerotti, A mechanism for the generation of cusp region hydromagnetic waves, *J. Geophys. Res.*, *93*, 7578, 1988.
- Lemaire, J., Impulsive penetration of filamentary plasma element into the magnetosphere of the Earth and Jupiter, *Planet. Space Sci.*, *25*, 887, 1977.
- Lemaire, J., and M. Roth, Penetration of solar wind plasma elements into the magnetosphere, *J. Atmos. Terr. Phys.*, *40*, 331, 1978.
- Lin, Y., and K.-K. Tschu, An analysis of Kelvin-Helmholtz instability in the low-latitude magnetopause-boundary layer region, *Planet. Space Sci.*, *36*, 687, 1988.

- Lockwood, M., P. E. Sandholt, and S. W. H. Cowley, Dayside auroral activity and magnetic flux transfer from the solar wind, *Geophys. Res. Lett.*, *16*, 33, 1989.
- Lockwood, M., S. W. H. Cowley, and P. E. Sandholt, Transient reconnection: Search for ionospheric signatures, *Eos Trans. AGU*, *71*, 709, 1990.
- Lotko, W., and M.-M. Shen, On large-scale rotational motions and energetics of auroral shear layers, *J. Geophys. Res.*, *96*, 9549, 1991.
- Lotko, W., B. U. Ö. Sonnerup, and R. L. Lysak, Nonsteady boundary layer flow including ionospheric drag and parallel electric fields, *J. Geophys. Res.*, *92*, 8635, 1987.
- Lu, G., P. H. Reiff, J. L. Burch, and J. D. Winningham, On the auroral current-voltage relationship, *J. Geophys. Res.*, *96*, 3523, 1991.
- Lui, A. T. Y., D. Venkatesan, G. Rostoker, J. S. Murphree, C. D. Anger, L. L. Cogger, and T. A. Potemra, Dayside auroral intensifications during a auroral substorm, *Geophys. Res. Lett.*, *14*, 415, 1987.
- Lui, A. T. Y., D. Venkatesan, and J. S. Murphree, Auroral bright spots on the dayside oval, *J. Geophys. Res.*, *94*, 5515, 1989.
- Lundin, R., and E. Dubinin, Solar wind energy transfer regions inside the dayside magnetopause, I, Evidence for magnetosheath plasma penetration, *Planet. Space Sci.*, *32*, 745, 1984.
- Lundin, R., and E. Dubinin, Solar wind energy transfer regions inside the dayside magnetopause: Accelerated heavy ions as traces for MHD-processes in the dayside boundary layer, *Planet. Space Sci.*, *33*, 891, 1985.
- Lyons, L. R., Generations of large-scale regions of auroral currents, electric potentials and precipitation by the divergence of the convection electric field, *J. Geophys. Res.*, *85*, 17, 1980.
- Lyons, L. R., Discrete aurora as the direct result of an inferred high-altitude generating potential distribution, *J. Geophys. Res.*, *86*, 1, 1981.
- Lysak, R. L., Auroral electrodynamics with current and voltage generators, *J. Geophys. Res.*, *90*, 4178, 1985.

- Lysak, R. L., Feedback instability of the ionospheric resonant cavity, *J. Geophys. Res.*, *96*, 1553, 1991.
- Lysak, R. L., and C. T. Dum, Dynamics of magnetosphere-ionosphere coupling including turbulent transport, *J. Geophys. Res.*, *88*, 365, 1983.
- Ma, Z. W., J. G. Hawkins, and L. C. Lee, A simulation study of impulsive penetration of solar wind irregularities into the magnetosphere at the dayside magnetopause, *J. Geophys. Res.*, *96*, in press, 1991.
- McHenry, M. A., C. R. Clauer, E. Friis-Christensen, and J. D. Kelly, Observations of ionospheric convection vortices: Signatures of momentum transfer, *Adv. Space Res.*, *8*, 315, 1988.
- McHenry, M. A., C. R. Clauer, E. Friis-Christensen, P. T. Newell, and J. D. Kelly, Ground observations of magnetospheric boundary layer phenomena, *J. Geophys. Res.*, *95*, 14995, 1990.
- Mitchell, D. G., F. Kutchoko, D. J. Williams, T. E. Eastman, L. A. Frank, and C. T. Russell, An extended study of the low-latitude boundary layer on the dawn and dusk flanks of the magnetosphere, *J. Geophys. Res.*, *92*, 7394, 1987.
- Miura, A., Anomalous transport by magnetohydrodynamic Kelvin-Helmholtz instabilities in the solar wind-magnetosphere interaction, *J. Geophys. Res.*, *89*, 801, 1984.
- Miura, A., and T. Sato, Numerical simulation of global formation of auroral arcs, *J. Geophys. Res.*, *85*, 73, 1980.
- Miura, A., and P. L. Pritchett, Nonlocal stability analysis of the MHD Kelvin-Helmholtz instability in a compressible plasma, *J. Geophys. Res.*, *87*, 7431, 1982.
- Murphree, J. S., L. L. Cogger, and C. D. Anger, Characteristics of the instantaneous auroral oval in the 1200–1800 MLT sector, *J. Geophys. Res.*, *86*, 7657, 1981.
- Ogilvie, K. W., and R. J. Fitzenreiter, The Kelvin-Helmholtz instability at the magnetopause and inner boundary layer surface, *J. Geophys. Res.*, *94*, 15,113, 1989.
- Olson, J. V., ULF signatures of polar cusp, *J. Geophys. Res.*, *91*, 10,055, 1986.

- Olson, J. V., Poleward propagation of pulsations near the cusp, *Planet. Space Sci.*, 37, 775, 1989.
- Olson, J. V., and G. Rostoker, Longitudinal phase variations of P<sub>c</sub> 4-5 micropulsations, *J. Geophys. Res.*, 83, 2481, 1978.
- Papamastorakis, I., G. Paschmann, W. Baumjohann, B. U. Ö. Sonnerup, and H. Lühr, Orientation, motion, and other properties of flux transfer event structures on September 4, 1984, *J. Geophys. Res.*, 94, 8852, 1989.
- Parker, E. N., *Cosmical Magnetic Fields*, Oxford University Press, New York, 1979.
- Paschmann, G., N. Sckopke, G. Haerendel, and J. Papamastorakis, ISEE plasma observations near the subsolar magnetopause, *Space Sci. Rev.*, 22, 717, 1978.
- Paschmann, G., G. Haerendel, I. Papamastorakis, N. Sckopke, S. J. Bame, J. T. Gosling, and C. T. Russell, Plasma and magnetic characteristics of magnetic flux transfer events, *J. Geophys. Res.*, 87, 2159, 1982.
- Phan, T. D., B. U. Ö. Sonnerup, and W. Lotko, Self-consistent model of the low-latitude boundary layer, *J. Geophys. Res.*, 94, 1281, 1989.
- Potemra, T. A., H. Vo, D. Venkatesan, L. L. Cogger, R. E. Erlandson, L. J. Zanetti, P. F. Bythrow, and B. J. Anderson, Periodic auroral forms and geomagnetic field oscillations in the 1400 MLT region, *J. Geophys. Res.*, 95, 5835, 1990.
- Priest, E. R., The equilibrium of magnetic flux ropes, in *The Physics of Magnetic Flux Ropes*, *Geophys. Monogr. Ser.*, vol. 58, edited by C. T. Russell, E. R. Priest, and L. C. Lee, pp. 1-22, AGU, Washington, D. C., 1990.
- Pu, Z. Y., and M. G. Kivelson, Kelvin-Helmholtz instability at the magnetopause: Energy flux into the magnetosphere, *J. Geophys. Res.*, 88, 853, 1983.
- Ratcliffe, J. A., *An Introduction to the Ionosphere and Magnetosphere*, p.90, Cambridge University Press, London, 1972.
- Rosenbauer, H., H. Grunwaldt, M. D. Montgomery, G. Paschmann, and N. Sckopke, HEOS 2 plasma observations in the distant polar magnetosphere: The plasma mantle, *J. Geophys. Res.*, 80, 2723, 1975.

- Rostoker, G., and T. Eastman, A boundary layer model for magnetospheric substorms, *J. Geophys. Res.*, *92*, 12187, 1987.
- Russell, C. T., Magnetic flux ropes in the ionosphere of Venus, in *The Physics of Magnetic Flux Ropes*, *Geophys. Monogr. Ser.*, vol. 58, edited by C. T. Russell, E. R. Priest, and L. C. Lee, pp. 413–423, AGU, Washington, D. C., 1990.
- Russell, C. T., and R. C. Elphic, ISEE observations of flux transfer events at the dayside magnetopause, *Geophys. Res. Lett.*, *6*, 33, 1979.
- Russell, C. T., R. C. Elphic, and J. A. Slavin, Initial Pioneer Venus magnetic field results: Dayside observations, *Science*, *203*, 745, 1979a.
- Russell, C. T., R. C. Elphic, and J. A. Slavin, Initial Pioneer Venus magnetic field results: Nightside observations, *Science*, *205*, 114, 1979b.
- Sandholt, P. E., C. S. Deehr, A. Egeland, B. Lybekk, R. Viereck, and G. J. Romick, Signatures in the dayside aurora of plasma transfer from the magnetosheath, *J. Geophys. Res.*, *91*, 10063, 1986.
- Sandholt, P. E., M. Lockwood, B. Lybekk, and A. D. Farmer, Auroral bright spot sequence near 1400 MLT: Coordinated optical and ion drift observations, *J. Geophys. Res.*, *95*, 21095, 1990.
- Sato, T., A theory of quiet auroral arcs, *J. Geophys. Res.*, *83*, 1042, 1978.
- Saunders, M. A., C. T. Russell, and N. Sckopke, Flux transfer events: Scale and interior structure, *Geophys. Res. Lett.*, *11*, 131, 1984.
- Schindler, K., On the role of irregularities in plasma entry into the magnetopause, *J. Geophys. Res.*, *84*, 7257, 1979.
- Scholer, M., Magnetic flux transfer at the magnetopause based on single X line bursty reconnection, *Geophys. Res. Lett.*, *15*, 291, 1988.
- Sckopke, N., G. Paschmann, H. Rosenbauer, and D. H. Fairfield, Influence of the interplanetary magnetic field on the occurrence and thickness of the plasma mantle, *J. Geophys. Res.*, *81*, 2687, 1976.

- Sckopke, N., G. Paschmann, G. Haerendel, B. U. Ö. Sonnerup, S. J. Bame, and E. W. Hones, Jr., Structure of the low-latitude boundary layer, *J. Geophys. Res.*, *86*, 2099, 1981.
- Seyler, C. E., Nonlinear 3-D evolution of bounded kinetic Alfvén waves due to shear flow and collisionless tearing instability, *Geophys. Res. Lett.*, *15*, 756, 1988.
- Seyler, C. E., A mathematical model of the structure and evolution of small-scale discrete auroral arcs, *J. Geophys. Res.*, *95*, 17199, 1990.
- Shi, Y., C. C. Wu, and L. C. Lee, A study of multiple X line reconnection at the dayside magnetopause, *Geophys. Res. Lett.*, *15*, 295, 1988.
- Shibata, K., and Y. Uchida, A magnetodynamic mechanism for the formation of astrophysical jets, I, Dynamical effects of the relaxation of nonlinear magnetic twists, *Publ. Astron. Soc. Jpn.*, *37*, 31, 1985.
- Sibeck, D. G., A model for the transient magnetospheric response to sudden solar wind dynamic pressure variations, *J. Geophys. Res.*, *95*, 3755, 1990.
- Sibeck, D. G., G. L. Siscoe, J. A. Slain, E. J. Smith, S. J. Bame, and F. L. Scarf, Magnetotail flux ropes, *Geophys. Res. Lett.*, *11*, 1090, 1984.
- Song, P., R. C. Elphic, C. T. Russell, J. T. Gosling, and C. A. Cattell, Structure and properties of the subsolar magnetopause for northward IMF: ISEE observations, *J. Geophys. Res.*, *95*, 6375, 1990.
- Song, Y., and R. L. Lysak, Evaluation of twist helicity of flux transfer events flux tubes, *J. Geophys. Res.*, *94*, 5273, 1989.
- Sonnerup, B. U. Ö., Theory of the low-latitude boundary layer, *J. Geophys. Res.*, *85*, 2017, 1980.
- Southwood, D. J., The hydromagnetic stability of the magnetospheric boundary, *Planet. Space Sci.*, *11*, 587, 1968.
- Southwood, D. J., The ionospheric signature of flux transfer events, *J. Geophys. Res.*, *92*, 3207, 1987.
- Southwood, D. J., and W. J. Hughes, Theory of hydromagnetic waves in the magnetosphere, *Space Sci. Rev.*, *35*, 301, 1983.

- Southwood, D. J., C. J. Farrugia, and M. A. Saunders, What are flux transfer events?, *Planet. Space Sci.*, 36, 503, 1988.
- Tsurutani, B. T., and R. M. Thorne, Diffusion processes in the magnetopause boundary layer, *Geophys. Res. Lett.*, 9, 1247, 1982.
- Tsurutani, B. T., E. J. Smith, R. M. Thorne, R. R. Anderson, D. A. Gurnett, G. K. Parks, C. S. Lin, and C. T. Russell, Wave-particle interactions at the magnetopause: Contributions to the dayside aurora, *Geophys. Res. Lett.*, 8, 183, 1981.
- Weimer, D. R., D. A. Gurnett, C. K. Goertz, J. D. Menietti, J. L. Burch, and M. Sugiura, The current-voltage relationship in auroral current sheets, *J. Geophys. Res.*, 92, 187, 1987.
- Wolfe, A., E. Kamen, L. J. Lanzerotti, C. G. MacLennan, J. F. Bamber, and D. Venkatesan, ULF geomagnetic power at cusp latitudes in response to upstream solar wind conditions, *J. Geophys. Res.*, 92, 168, 1987.
- Wright, A. N., The evolution of an isolated reconnected flux tubes, *Planet. Space Sci.*, 35, 813, 1987.
- Wright, A. N., and M. A. Berger, The effect of reconnection upon the linkage and interior structure of magnetic flux tubes, *J. Geophys. Res.*, 94, 1295, 1989.
- Wu, C. C., Kelvin-Helmholtz instability at the magnetospheric boundary, *J. Geophys. Res.*, 91, 3042, 1986.